Master's thesis

NTNU
Norwegian University of Science and Technology
Faculty of Information Technology and Electrical Engineering
Department of Engineering Cybernetics

Marcus Nicolai Løvdal

Design of Moving-mass and Dive-plane Control Systems for AUVs

Master's thesis in Cybernetics and Robotics
Supervisor: Thor I. Fossen
June 2021

NTNU
Norwegian University of
Science and Technology

Marcus Nicolai Løvdal

Design of Moving-mass and Dive-plane Control Systems for AUVs

Master's thesis in Cybernetics and Robotics
Supervisor: Thor I. Fossen
June 2021

Norwegian University of Science and Technology
Faculty of Information Technology and Electrical Engineering
Department of Engineering Cybernetics

NTNU
Norwegian University of
Science and Technology

NTNU
Norwegian University of
Science and Technology

Faculty of Information Technology
and Electrical Engineering
Department of Engineering Cybernetics

MASTER'S THESIS PROJECT DESCRIPTION

Name: Marcus Nicolai Løvdal
Department: Engineering Cybernetics
Thesis title: Design of Moving-mass and Dive-plane Control Systems for AUVs

Thesis Description:

The main purpose of the project is to design a moving-mass and dive-plane control system for an autonomous underwater vehicle (AUV). Focus should be placed on pitch and depth control.

The following topics and challenges should be considered in more detail:

1. Literature study on methods for moving-mass control of vehicles.
2. System description including scope and limitations. Appropriate research questions should be formulated to solve the problem.
3. Develop a simulator in Matlab for testing of moving-mass and dive-plane control systems applied to an AUV.
4. Develop control algorithms for simultaneous moving-mass and dive-plane depth control.
5. Investigate and compare the performance of moving-mass actuation with using only dive-planes for depth and pitch control.
6. Simulate the control system and conclude your findings.

Thesis performed at: Department of Engineering Cybernetics, NTNU
Supervisor: Professor Thor I. Fossen, Dept. of Eng. Cybernetics, NTNU

Acknowledgments

I would like to thank my supervisor, Thor I. Fossen, for his support for this thesis, by providing relevant material, knowledge, and experience both as a supervisor and as an expert within the field of guidance, navigation, and control of vehicles. Having the author of the material much of this thesis is based on as a supervisor has been a privilege.

Additionally, I would like to thank my friends and family for their support, both in-person and online. Not just through this semester, but through the entire pandemic. This would have been a lot harder without you.

Abstract

In this thesis, the literature on moving-mass actuation and control for vehicles in various applications is reviewed and discussed, considering a variety of moving-mass configurations. The advantages and disadvantages of implementing moving-mass actuation (MMA) in autonomous underwater vehicles (AUVs) are considered and compared to traditional dive-plane (DP) actuation, both in theory and in simulations. The equations of motion for the coupled MMA-AUV system are derived based on conservation of momentum and modified to include dive-planes, environmental, damping, and restoring forces for buoyant vehicles. Control laws for MMA and dive-planes are derived for pitch and depth control, verified in simulations and compared. The vehicle is simulated considering combinations of actuation methods and the results are compared. Case studies for implementing MMA as a failsafe function, as a drag reduction method, and as an auxiliary actuator are simulated and discussed.

Contents

List of Figures

Chapter 1

Introduction

Throughout history, many methods for vehicle attitude control have been proposed and implemented. In general, these methods control the attitude by applying control torques to the desired vehicle. Examples of conventional control torque actuators include control surfaces such as RCS thrusters and vectored engines for rockets, reaction wheels for satellites, ailerons and rudders for fixed-wing airplanes, and rudder and/or directional (azimuth) thrusters for ships and underwater vehicles. However, instead of applying the control torque actively, it can be applied indirectly by adjusting the relative position of the main thruster(s) of the vehicle act(s). In general, most vehicles are affected by a main thruster (e.g. main propeller(s) for ships, underwater vehicles, and aircraft) and gravity. By adjusting the relative distance between the points of application of these forces, a control torque can be introduced indirectly. In theory, a possible method of introducing this distance could be to introduce movable thrusters, however, a more feasible alternative is to adjust the center of gravity (CG) instead to generate an arm between the acting forces and CG. As will be discussed, several concepts for and methods of adjusting the CG exists in literature, however, in general, these methods encompass the concept of **Moving-Mass Actuation (MMA)**.

1.1 What is MMA?

The basic concept of MMA is to introduce an actuation based on introducing a movable, controllable mass within the vehicle. By moving this mass, the CG can be adjusted and an indirect control torque is thus generated, as the restoring forces acting on the variable CG position generating a variable, controllable torque. This method of attitude control can provide a torque that does not actively use propellant or electric power to maintain a fixed control torque, making it suitable for long-endurance missions. Additionally, since the components of MMA systems can be placed entirely within the controlled vehicle, they are much less affected by the vehicle environment, resulting in longer component endurance and lower specification requirements. Simultaneously, MMA affects the environment less than traditional actuators, considering the effects of induced drag and propellant plume and/or jet stream effects. Specific advantages and disadvantages are dependent on the area of deployment, being in space, supersonic, aerial, or underwater conditions.

1.2 MMA in Space

For space operations, payload requirements are typically affected by high mass launch prices and volumetric constraints. Therefore, using propulsion methods that are highly efficient in volume

and mass is of great importance in this field, especially in the growing field of tiny Cube Satellites (CubeSats).

1.2.1 CubeSat Propelled by Solid Rocket Motor

In [5], the use of a Solid Rocket Motor is discussed as a thruster. They argue that rocket-propelled vehicles using Solid Rocket Motors can have a misalignment between the motor thrust vector and the center of mass, which will generate an undesired torque on the vehicle as the thrust cannot be vectored. Additionally, they argue that using a Solid Rocket Motor can influence the attitude from jet-damping torques. Since the CubeSat is so small, they argue that conventional methods such as using jet vanes, attitude thrusters, or nozzle gimbaling/vectoring are not suitable for the miniature Solid Rocket Motors considered for their CubeSat. They also argue that using the more general method of spinning stability for attitude control can generate some undesirable instabilities. As an alternative, they examine the use of an MMA system to correct the misalignment of the thrust vector, by re-aligning the CG. They propose a configuration of 2 masses adjusting the CG to stabilize pitch and yaw motion. Through simulations, they conclude that the usage of MMA proves feasible, though their simulations did not include sensor errors, leaving it as future research.

1.2.2 Solar Sailing CubeSat

Another implementation of MMA in CubeSats has been suggested by [6], where it is discussed as an alternative method for attitude control of a CubeSat propelled by Solar sails. As the attitude of the satellite effectively determines the direction the resultant solar radiation force acts, it is of great importance for the guidance of Solar-sail-powered spacecraft. However, as argued by Huang and Zhou, the actuation problem can not use conventional active attitude methods due to issues related to the large inertia of solar sails and endurance requirements typically placed upon solar-sail-powered missions. Instead, they discuss the use of moving-mass actuation to generate an offset between the center of mass and center of pressure from the solar radiation, to generate the desired control torques without propellant or "active" actuators such as reaction wheels. Rather than implementing additional moving masses, they propose a configuration of rolling screws mounted between the CubeSat and a 1.2m x 1.2m plate connected to the 10 m x 10 m solar sail, and using the CubeSat as a single moving-mass with 2 degrees of freedom, allowing the generation of control torques in pitch and yaw. Through simulations, they conclude that moving-mass actuation (or mass-moving control, as the authors call it) is feasible for attitude control depending on the initial and desired state of the solar sail, due to the limited torque output such a system can provide. They also discuss an alternative use of moving-mass actuation as an auxiliary system to unload a flywheel of angular momentum, to increase the feasibility of using an active reaction wheel attitude control system.

1.3 MMA in Supersonic and/or Atmospheric Re-Entry Vehicles

Moving-mass actuation has also been discussed as a method for control of supersonic and/or atmospheric reentry vehicles. For these systems, the external force discussed for MMA is typically the aerodynamic lift occurring from static lift surfaces. The resulting lift force vector lies normal to the sway-surge body axes, allowing implementation of MMA in roll (sway) and pitch (surge) channels. In the literature reviewed for this thesis, these surfaces are generally smaller surfaces on missile reentry payloads that are used to either stabilize their attitude or as a means of guidance during the reentry phase to increase targeting accuracy. Conventional alternatives to MMA include

attitude thrusters and aerodynamic control surfaces such as rudders and ailerons, however, MMA has some advantages over both of these methods:

- **Control surfaces** are discussed[22, 23] to have issues related to great airspeed conditions, namely that high airspeeds ablates, generates heat on and stresses the surfaces thus introducing greater specification requirements on these, or even potentially making them infeasible. Additionally, using aerodynamic control surfaces induces additional drag and thus reduces the energy efficiency of the vehicle, while MMA can be confined within the airframe of the vehicle and thus allows optimal aerodynamic vehicle shaping. MMA is also independent of flap loads, meaning it potentially has lower actuator specification requirements than control surfaces.

- **Attitude thrusters** generally provide thrust independent of airflow, however, requires propellant to operate. Additionally, using thrusters affect the aerodynamic shape of the vehicle and can introduce fumes that potentially obscures electro-optical sensors[22]. Still, some configurations suggested in literature implements MMA in combination with thrusters, namely in roll channel. [28] states that "Nonetheless, the roll channel cannot be controlled effectively only by MMC [Moving-Mass Control] Technology", and argues that RCS thrusters should be used to control the roll channel of the vehicle.

1.4 MMA in UAVs

Due to the energy efficiency of MMA, its use has been discussed in specialized UAVs such as the High-altitude long-endurance (HALE) concept proposed by [1], the bi-rotor UAV concept presented by [2], and the heavy-lift, multi-rotor, IC-powered UAV from the MORUS project[3]. Each of these UAVs has its own specific challenges that are addressed.

1.4.1 High-Altitude Long-Endurance (HALE) UAV with flexible wing

In [1], the use of MMA in HALE vehicles is discussed as an alternative to control surfaces, mostly due to their energy efficiency and aerodynamic optimality. That is, they argue that the control authority of such surfaces is limited due to the high altitude, that the long endurance of the mission places especial importance on the aerodynamics of the UAV, and that the induced drag from the control surfaces therefore is undesired.

1.4.2 Vertical Takeoff and Landing (VTOL) bi-rotor UAV

[2] presents a novel configuration for control of a coaxial bi-rotor VTOL UAV. Rather than using conventional approaches to roll and pitch control, the authors examine the use of MMA to enable the full aerodynamic force to be used to lift the UAV and to simplify rotor design. Since the configuration only has two co-axial rotors spinning opposite ways with constant propeller attack angle, they cannot be used to control the pitch and/or roll of the UAV. Thus, [2] conceptualizes the use of MMA for these channels by implementing four moving masses along each side of the UAV.

1.4.3 Heavy-Lift Multi-Rotor Internal Combustion UAV

For the MORUS project[3], Haus et al argue that using internal combustion (IC) engines for UAVs is necessary for their project due to their requirement for high power over longer missions. However, they also argue that such engines are dynamically limited and thus unable to stabilize a quadrotor

in flight. Therefore, they present a control concept using MMA to perform this task, and show that using MMA is feasible in their system both in simulations and experiments.

1.5 MMA in AUVs

In underwater vehicles, similar issues related to control surfaces and thrusters related to attitude control can be found. While underwater vehicles are not subject to the same heating conditions as supersonic flying vehicles, control surface joints for AUVs are still subject to wear over time and, similarly as for flying vehicles, provide low control torque in low relative velocities, which is especially important for underwater vehicles. MMA can therefore be introduced as an alternative, or additional attitude control actuator, since it is independent of the relative velocity and is not exposed to the environment, unlike control surfaces. MMA also maintains the advantage of not inducing any drag, providing a more efficient control method for endurance missions. Due to these advantages, MMA has already been implemented as an auxiliary control system in systems such as the Folaga vehicles (as referenced by [18]), SLOCUM [16], MARIN's modular AUV[14], and VTMAUV (as payload)[11]. The use of MMA is also discussed in the literature to be used in fully-actuated AUVs, namely Hybrid Underwater Gliders (HUG), such as in [13]. In these practical implementations, the moving mass is often implemented by moving the AUV battery pack in surge direction to induce pitch in the vehicles.

Most of the AUVs found in this literature review are classified either as underwater gliders or hybrid underwater gliders. MMA is typically discussed in these vehicles due to the requirements on endurance, reliability, and robustness the missions these gliders are designed for. Using MMA in other, non-streamlined AUVs is typically not discussed since these typically are actuated by thrusters instead, though exploring implementing MMA as an auxiliary system in these vehicles could also be explored as an optimization opportunity.

1.6 MMA Configurations

Several configurations of MMA have been discussed for implementation, especially for supersonic and/or re-entry vehicles. The main configuration parameters are the number of masses, the degrees of freedom, the size of the moving mass ("small"/"large") relative to the vehicle mass, and the placement of movement rails. Since MMA is implemented inside the vehicle frame, and the rail on which the mass moves needs to be unobstructed, the configurations are limited by the physical constraints of the vehicle and imposes limitations to the other internal components.

1.6.1 Single DOF

The simplest configurations implement a single moving-mass with translation along the desired body axis, for example along the surge axis for pitch control (e.g. as in [7], [9] and [14]) or sway axis (e.g. as in [1] and [27]). For these configurations the relative mass is small [14, 5kg], [1, 1kg in 12kg wing], [9, 2kg in 10kg body], [7, 2kg in 20kg body]. As an alternative, to avoid the spatial constraints of MMA, the actuator can be placed as a module outside the body. [11] provides such an experiment where an MMA module actuating in surge/pitch was placed under the AUV, providing a greater actuating arm since it is not limited by the internal space of the vehicle.

Alternatively, the moving mass can be separated into two parallel actuators with equal mass, such that the centerline of the vehicle is freed. This relieves spatial constraints inside the vehicle, in addition to solving the problem of colliding actuators when multiple DOFs are implemented.

1.6.2 Multiple DOFs

In theory, implementing additional actuators along other body axes to introduce more DOF of the attitude control system is simple in concept. However, since these axes intersect, this limits the actuation range of the masses since they would otherwise collide. This can be avoided by moving the masses off-center and splitting the masses into parallel actuators, such as in [2]. Another alternative is to implement a single moving-mass placed on a rotating rail, such as in [19], [20], [21], and [24], to allow two DOFs using only one moving mass.

1.6.3 Moving-mass size

Since the resulting control torque is proportional to the size of the mass and the actuation length, both the size of the mass and the length of the arm affect the possible torque output of the system. On one hand, increasing the mass size increases the performance of the system, however, this generally also increases the total vehicle weight with is particularly undesirable for air- and spacecraft. On the other hand, increasing the maximum arm available increases the spatial demand of the system. Considering the limited space within re-entry vehicles, Li, Gao et al presents and discusses [19, 21, 24, 25] a configuration that uses a large mass ratio by effectively moving the entire payload on a rail, and provides experiments with mass ratios from 0 to 0.8 between moving- and total vehicle mass[25]. A similar approach for underwater gliders is discussed by [8], where the internal components are connected to a "common rail" that can be rotated, allowing approximately 90% of the vehicle mass to be used as a "moving-mass" in the roll channel of the vehicle. However, while increasing the mass ratio increases the control authority, the assumption that the moving mass can be treated as a point mass becomes increasingly invalid in terms of controller stability design, as argued by [21], requiring the use of complex nonlinear control methods.

1.7 Control of MMA

The control methods applied to MMA in the literature vary greatly depending on the requirements of disturbance compensation and general performance. [4] names examples of literature using classical control methods such as PID, Linear Quadratic Regulator (LQR), Sliding-mode, feedback-linearization, and back-stepping. Additionally, [4] discusses the use of intelligent control methods such as fuzzy logic and neural networks as a method of estimating and compensating uncertainties in MMA. Another control method found in literature is energy-based control, namely energy shaping [9, 10]. In the literature reviewed for this thesis, many of these control methods have been discussed and implemented. [8] demonstrates the use of MMA in AUVs experimentally using PID control. Similarly, [3] verifies the use of MMA controlled by PID on a UAV mounted to a gimbal testbed. [7] simulates and compares the performance of LQR, Model-predictive control (MPC), and Neural-Network Predictive Control (NNPC) on an AUV, demonstrating the advantage of intelligent control (e.g. NNPC here) when disturbances are present, though their simulated model is linearized. [12] implements backstepping and the Lyapunov redesign approach in their controller design, considering coupled dynamics in their controller design. [15] and [16] Implements LQR. Feedback linearization is used by [20] and [22]. Backstepping is used by [26, 27, 5]. Other Advanced nonlinear controllers are also discussed in literature, namely Sliding-mode control

[5, 17, 28, 29, 30], and Immersion & Invariance (I&I) [19, 21, 25] control as well as adaptive control schemes such as in [26]. In general, these methods are implemented in simulations, with mostly PID control being experimentally verified.

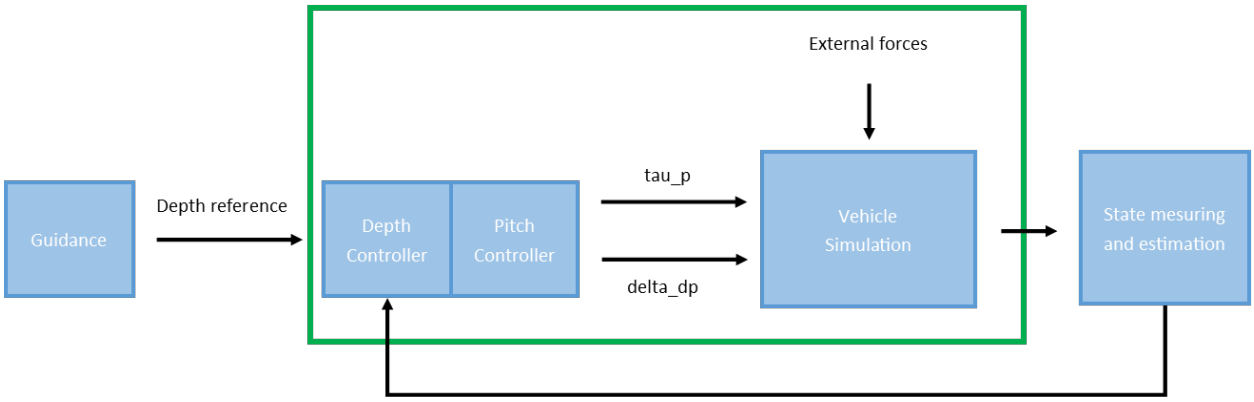

Figure 1.1: Limitation of problem definition in this thesis (green)

1.8 Disadvantages of MMA

While MMA has some advantages over other control methods, the concept is not without challenges. As discussed in section 1.6.3, the control torque applied is proportional to the mass size and actuation length, and increasing the mass gradually invalidates the point-mass assumption, as discussed in [21]. However, in addition to the spatial requirement, the actuation length cannot be extended indefinitely. This effectively imposes a saturation on the actuator and is deemed "The biggest shortcoming of the MMC" by [3]. When discussing the solar-sailing CubeSat (sec. 1.2.2), [6] argues that the feasibility of MMA for their system is dependent on the initial and desired state of the solar sail, as the limited maximum torque an MMA can provide could be too low to fulfill control requirements if the initial angular momentum is too high. Additionally, introducing MMA complicates the dynamical response of the system, as it generates additional products of inertia. Uncertainty of environmental forces also complicates control design, as argued by [22, 26, "the airframe (...) and must have near-neutral aerodynamic static stability characteristics"], as they are complex to model and thus often are left as unknown disturbances to be compensated for. Finally, the spatial requirement of MMA could make the control method infeasible, depending on implementation. Namely, in reentry vehicles the space available is limited, prompting the diverse use of configurations discussed in section 1.6.

1.9 Problem Definition

Despite the disadvantages of MMA discussed in section 1.8, the objective of this thesis is to design a depth control system for an AUV based on moving-mass actuation combined with dive-planes (DP). To avoid the usage of nonlinear theory, the mass is assumed to be small, such that it can be modeled as a point-mass In return, the actuator is modeled to actuate over the entire length of the vehicle. The performance of this system is to be modeled and simulated in Matlab for comparison and discussion. The thesis considers control system design assuming full-state feedback with negligible disturbances, with a depth level reference and applied actuation δ_{dp} in dive-planes and actuation

force τ_p on the internal mass of the vehicle. This thesis is therefore limited to control system design, illustrated by the green box in figure 1.1. The performance of the control system is to be examined in various contexts and cases, such as constant ocean currents, various surge velocities, fail-safe functionality, and a method of reducing the drag from conventional dive-plane actuation. The controllers are to be designed to minimize overshoot and to consider actuator saturation limits. Based on this, the following research questions are posed:

Research questions

- **Q1:** Can moving-mass actuators be used as sole actuators for depth control?
- **Q2:** How does the addition of MMA to a depth control system affect system performance?
- **Q3:** In which cases is moving-mass actuation beneficial over conventional dive-planes?
- **Q4:** How does the saturation limit of moving-mass actuation affect the control system?

1.10 Main Contributions

The main contributions presented in this thesis include:

- Derived an AUV model with moving-mass and dive-plane system for depth control
- Developed control systems for pitch and depth control, considering moving-mass-, dive-plane- and combined -actuation
- Examined and compared open-loop control laws in pitch
- Compared dive-plane actuation with combined actuation to demonstrate effectiveness of the system in different cases

1.11 Organization of Thesis

The remainder of this is organized as:

- Ch. 2: Deriving the equations of motion for the coupled system
- Ch. 3: Deriving controllers for surge subsystem, open-loop pitch control considering both MMA and dive-planes, and closed-loop depth controller
- Ch. 4: Simulating Control Laws derived in previous chapter for comparison and discussion
- Ch. 5: Simulating various cases for discussion and comparison of MMA, dive-planes and combined actuation.
- Ch. 6: Concluding the findings of this thesis

1.12 List of Acronyms

- MMC: Moving-Mass Control
- MMA: Moving-Mass Actuation
- DP: Dive-Plane(s)
- DOF: Degree(s) Of Freedom
- CG: Center (of) Gravity
- CB: Center (of) Buoyancy
- CO: (BODY) Coordinate Origin
- NED: North-East-Down
- UAV: Underwater Autonomous Vehicle
- LOS: Line-Of-Sight
- ILOS: Integral LOS

Chapter 2

Theory and Equations of Motion

The notation used in this thesis closely follow the notation from Fossen [33].

2.1 Coordinate Frames

There are three coordinate frames that are actively used for this thesis:

Name	Notation	Used for
North-East-Down (NED)	{n}	Vehicle position for control
Body	{b}	Vehicle dynamics
Flow	{f}	Vehicle hydrodynamics

(2.1)

- North-East-Down-frame (NED-frame) describes the vehicle position where the x-axis points towards north, y-axis towards east, and z-axis down into the earth. This effectively means that NED operates as a tangent field over the planetary surface, though for local navigation ($10km \times 10km$ [33, p.18]) the axes can be assumed to be constant.
- Body-frame is useful for describing the vehicle dynamics dependent on forces acting on the body, such as thrusters, control surfaces, and damping. The frame is fixed to and thus rotates with the vehicle.
- Flow-frame is used to express the hydrodynamic forces acting on the vehicle, such as lift and drag, since these typically act depending on the relative velocity of the vehicle.

The frames are related by the rotation matrices $\boldsymbol{R}_j^i$, which transforms 3-DOF vectors from frame $\{j\}$ to frame $\{i\}$ by performing rotations around the x, y and z-axis. The rotation matrices are provided[33, Ch.2] by:

$$\boldsymbol{R}_b^n = \begin{bmatrix} c_\psi c_\theta & -s_\psi c_\phi + c_\psi s_\theta s_\phi & s_\psi s_\phi + c_\psi c_\phi s_\theta \\ s_\psi c_\theta & c_\psi c_\phi + s_\phi s_\theta s_\psi & -c_\psi s_\phi + s_\theta s_\psi c_\phi \\ -s_\theta & c_\theta s_\phi & c_\theta c_\phi \end{bmatrix} \tag{2.2}$$

$$\boldsymbol{R}_n^b = (\boldsymbol{R}_b^n)^T \tag{2.3}$$

$$\boldsymbol{R}_f^b = \left(\boldsymbol{R}_n^f\right)^T = \begin{bmatrix} c_\beta c_\alpha & -s_\beta c_\alpha & -s_\alpha \\ s_\beta & c_\beta & 0 \\ c_\beta s_\alpha & -s_\beta s_\alpha & c_\alpha \end{bmatrix} \tag{2.4}$$

Where s_i and c_i denotes the sinus or cosines of the subscripted angle i.

2.2 Notation

The notation of SNAME[34] (as cited by Fossen [33]), is used as to denote the state variables:

$$\boldsymbol{v}_{nb}^{b} = \begin{bmatrix} v_{nb,x}^{b} \\ v_{nb,y}^{b} \\ v_{nb,z}^{b} \end{bmatrix} = \begin{bmatrix} u \\ v \\ w \end{bmatrix} = \boldsymbol{\nu}_1 \tag{2.5}$$

$$\boldsymbol{\omega}_{b}^{b} = \begin{bmatrix} \omega_{bx}^{b} \\ \omega_{by}^{b} \\ \omega_{bz}^{b} \end{bmatrix} = \begin{bmatrix} p \\ q \\ r \end{bmatrix} = \boldsymbol{\nu_2} \tag{2.6}$$

Additionally, the NED attitude of the vehicle is denoted using the Euler angles roll (ϕ), pitch (θ) and yaw (ψ), which provide the state general state vectors:

$$\boldsymbol{\nu} = \begin{bmatrix} \boldsymbol{\nu_1} \\ \boldsymbol{\nu_2} \end{bmatrix} = \begin{bmatrix} u \\ v \\ w \\ p \\ q \\ r \end{bmatrix} \tag{2.7}$$

$$\boldsymbol{\eta} = \begin{bmatrix} \boldsymbol{p^n} \\ \boldsymbol{\Theta_{nb}} \end{bmatrix} = \begin{bmatrix} x^n \\ y^n \\ z^n \\ \phi \\ \theta \\ \psi \end{bmatrix} \tag{2.8}$$

The 6-DOF equations of motion for a marine craft presented in Fossen[33, Ch.2] can be summarized as:

$$\dot{\boldsymbol{\eta}} = \mathbf{J}_{\Theta}(\boldsymbol{\eta})\boldsymbol{\nu} \tag{2.9}$$

$$\mathbf{M}\dot{\boldsymbol{\nu}} + \mathbf{C}(\boldsymbol{\nu})\boldsymbol{\nu} + \mathbf{D}(\boldsymbol{\nu})\boldsymbol{\nu} + \mathbf{g}(\boldsymbol{\eta}) + \mathbf{g}_0 = \boldsymbol{\tau} + \boldsymbol{\tau}_{wind} + \boldsymbol{\tau}_{wave} \tag{2.10}$$

Where:

$\boldsymbol{\eta}$	NED position and attitude vector
$\boldsymbol{\nu}$	BODY generalized velocity vector
$\mathbf{J}_{\Theta}$	Transformation matrix from BODY to NED
$\mathbf{M}$	Mass matrix
$\mathbf{C}$	Coriolis and centripetal matrix
$\mathbf{D}$	Damping matrix
$\mathbf{g}$	Restoring forces
$\boldsymbol{\tau}$	Generalized applied and environmental forces

(2.11)

2.3 Equations of Motion for Coupled System

The equations of motion of mechanical systems are often derived based on Newton's second law of motion:

$$\mathbf{F} = m\mathbf{a} \tag{2.12}$$

Where with net force $\mathbf{F}$, system mass m and acceleration a. However, this form of the law is a case of the generalized law:

$$\mathbf{F} = \frac{d(m\mathbf{a})}{dt} \tag{2.13}$$

Where the m is assumed to be constant. When implementing moving masses to the system, the mass becomes time-varying, and as such this assumption is no longer valid. Instead, the general law should be implemented instead:

$$\mathbf{F} = \frac{d\mathbf{p}}{dt} \tag{2.14}$$

Where $\mathbf{p}$ is the momentum of the system. The equations of motion are therefore derived based on the vehicle momentum. The equations used for this thesis are based on the model presented by Woolsey and Leonard, as cited by Fossen[33]. There, the momentum-based equations of motion are based on the kinetic energy of the system:

$$\boldsymbol{T} = \frac{1}{2}\begin{bmatrix}(\boldsymbol{v}_{bp}^b)^T & \boldsymbol{\nu}_1^T & \boldsymbol{\nu}_2^T\end{bmatrix}\boldsymbol{M}(\boldsymbol{r}_{bp}^b)\begin{bmatrix}\boldsymbol{v}_{bp}^b \\ \boldsymbol{\nu_1} \\ \boldsymbol{\nu_2}\end{bmatrix} \tag{2.15}$$

Where $\boldsymbol{v}_{bp}^b$ is the linear velocity of the point-mass in {b}. Note that since the moved mass is modeled as a point-mass, it does not have any angular velocity and the state-space is thereby 9-DOF. Furthermore, the mass matrix $\boldsymbol{M}(\boldsymbol{r}_{bp}^b)$ can be described, provided in Fossen[33], as:

$$\boldsymbol{M}(\boldsymbol{r}_{bp}^b) = \boldsymbol{M}_{RB}(\boldsymbol{r}_{bp}^b) + \boldsymbol{M}_A \tag{2.16}$$

$$= \begin{bmatrix} m_p\boldsymbol{I}_3 & m_p\boldsymbol{I}_3 & -m_pS(\boldsymbol{r}_{bp}^b) \\ m_p\boldsymbol{I}_3 & (m_v+m_p)\boldsymbol{I}_3 + \boldsymbol{A}_{11} & -m_pS(\boldsymbol{r}_{bp}^b) - m_vS(\boldsymbol{r}_{bg}^b) + \boldsymbol{A}_{12} \\ m_pS(\boldsymbol{r}_{bp}^b) & m_pS(\boldsymbol{r}_{bp}^b) + m_vS(\boldsymbol{r}_{bg}^b) + \boldsymbol{A}_{21} & \boldsymbol{I}_b^b - m_pS^2(\boldsymbol{r}_{bp}^b) + \boldsymbol{A}_{22} \end{bmatrix} \tag{2.17}$$

Where A_{ij} is the added mass resulting from the environment:

$$\boldsymbol{M}_A = \begin{bmatrix}\boldsymbol{0}_3 & \boldsymbol{0}_3 & \boldsymbol{0}_3 \\ \boldsymbol{0}_3 & \boldsymbol{A}_{11} & \boldsymbol{A}_{12} \\ \boldsymbol{0}_3 & \boldsymbol{A}_{21} & \boldsymbol{A}_{22}\end{bmatrix} \tag{2.18}$$

Considering diagonal added mass matrix:

$$\boldsymbol{M}_A = \text{diag}([0,0,0,X_{\dot{u}},Y_{\dot{v}},Z_{\dot{w}},K_{\dot{p}},M_{\dot{q}},N_{\dot{r}}] \tag{2.19}$$

$$\boldsymbol{A}_{11} = \text{diag}([X_{\dot{u}},Y_{\dot{v}},Z_{\dot{w}}]) \tag{2.20}$$

$$\boldsymbol{A}_{12} = \boldsymbol{A}_{21} = \boldsymbol{0}_3 \tag{2.21}$$

$$\boldsymbol{A}_{22} = \text{diag}([K_{\dot{p}},M_{\dot{q}},N_{\dot{r}}]) \tag{2.22}$$

The added mass coefficients $[X_{\dot{u}}, Y_{\dot{v}}, ..., N_{\dot{r}}]$ is determined assuming a slender body as described by Techet[31]. Considering a uniform body, the equations provided by her can be described as:

$$\begin{bmatrix} X_{\dot{u}} \\ Y_{\dot{v}} \\ Z_{\dot{w}} \\ K_{\dot{p}} \\ M_{\dot{q}} \\ N_{\dot{r}} \end{bmatrix} = \begin{bmatrix} 0 \\ \int_L 1.51\pi\rho_w d^2 dx \\ \int_L 1.51\pi\rho_w d^2 dx \\ \int_L 0.234\pi\rho_w d^4 dx \\ \int_L x^2 1.51\pi\rho_w d^2 dx \\ \int_L x^2 1.51\pi\rho_w d^2 dx \end{bmatrix} = \begin{bmatrix} 0 \\ 1.51\pi\rho_w d^2 l \\ 1.51\pi\rho_w d^2 l \\ 0.234\pi\rho_w d^4 l \\ 1.51\pi\rho_w d^2 \frac{1}{12} l^3 \\ 1.51\pi\rho_w d^2 \frac{1}{12} l^3 \end{bmatrix} \tag{2.23}$$

Where d is the half-width of the equivalent square cross-section of the vehicle. Namely, for a square cross-section vehicle with $b = h$, $= \frac{1}{2}b = \frac{1}{2}h$. Note that the moving-mass does not provide added mass, as it is shielded from the environment. The inertia matrix $\boldsymbol{I}_b^b$ is based on a uniform rectangular vehicle shape, such that, for a vehicle with mass m_v, length l, width b and height h, the matrix is:

$$\boldsymbol{I}_b^b = \begin{bmatrix} I_{xx} & 0 & 0 \\ 0 & I_{yy} & 0 \\ 0 & 0 & I_{zz} \end{bmatrix} \tag{2.24}$$

$$I_{xx} = \frac{1}{12} m_v (b^2 + l^2) \tag{2.25}$$

$$I_{yy} = \frac{1}{12} m_v (l^2 + h^2) \tag{2.26}$$

$$I_{zz} = \frac{1}{12} m_v (h^2 + b^2) \tag{2.27}$$

Furthermore, as shown in Fossen[33, s9.9], the linear ($\boldsymbol{\mathcal{P}}_p^b$, $\boldsymbol{\mathcal{P}}_v^b$) and angular momentums ($\boldsymbol{\mathcal{H}}_v^b$) are then obtainable as:

$$\boldsymbol{\mathcal{P}} := \begin{bmatrix} \boldsymbol{\mathcal{P}}_p^b \\ \boldsymbol{\mathcal{P}}_v^b \\ \boldsymbol{\mathcal{H}}_v^b \end{bmatrix} = \boldsymbol{M}(\boldsymbol{r}_{bp}^b) \begin{bmatrix} \boldsymbol{v}_{bp}^b \\ \boldsymbol{\nu_1} \\ \boldsymbol{\nu_2} \end{bmatrix} \tag{2.28}$$

$$:= \boldsymbol{M}(\boldsymbol{r}_{bp}^b)\boldsymbol{\nu} \tag{2.29}$$

Which describe the relation between the full 9-DOF momentum and velocity vectors $\boldsymbol{\mathcal{P}}$ and $\boldsymbol{\nu}$. Following Fossen[33, s9.9], a vehicle configuration with neutral buoyancy and a b coordinate origin (CO) coinciding with the Center of Buoyancy (CB) yields the set of equations:

$$\dot{\boldsymbol{\mathcal{P}}} = \begin{bmatrix} \dot{\boldsymbol{\mathcal{P}}}_p^b \\ \dot{\boldsymbol{\mathcal{P}}}_v^b \\ \dot{\boldsymbol{\mathcal{H}}}^b \end{bmatrix} \tag{2.30}$$

$$\dot{\boldsymbol{\mathcal{P}}}_p^b = -S(\boldsymbol{\nu_2})\boldsymbol{\mathcal{P}}_p^b + \boldsymbol{R}_n^b \boldsymbol{f}_{gp}^n + \boldsymbol{\tau}_p \tag{2.31}$$

$$\dot{\boldsymbol{\mathcal{P}}}_b^b = -S(\boldsymbol{\nu_2})\boldsymbol{\mathcal{P}}_v^b \tag{2.32}$$

$$\dot{\boldsymbol{\mathcal{H}}}^b = -S(\boldsymbol{\nu_1})\boldsymbol{\mathcal{P}}^b - S(\boldsymbol{\nu_2})\boldsymbol{\mathcal{H}}^b + S(\boldsymbol{r}_{bp}^b)\boldsymbol{R}_n^b \boldsymbol{f}_{gp}^n + S(\boldsymbol{r}_{bg}^b)\boldsymbol{R}_n^b \boldsymbol{f}_g^n \tag{2.33}$$

With:

$\boldsymbol{\tau}_p$	Internal control force applied to the moving mass (point-mass)
$\boldsymbol{R}_n^b$	Rotation matrix transforming 3-DOF vector from {n} to {b}
$\boldsymbol{f}_{gp}^n$	Gravity vector for point-mass in {n}
$\boldsymbol{f}_g^n$	Gravity vector for vehicle in {n}

The system can then be simulated based on its momentums, and be transformed to body velocities and NED positions by:

$$\boldsymbol{\nu} = \boldsymbol{M}^{-1}(\boldsymbol{r}_{bp}^b)\boldsymbol{P} \tag{2.34}$$

$$\dot{\boldsymbol{r}}_{bp}^b = \boldsymbol{v}_{bp}^b \tag{2.35}$$

$$\dot{\boldsymbol{\eta}} = \boldsymbol{T}_b^n \begin{bmatrix} \boldsymbol{\nu_1} \\ \boldsymbol{\nu_2} \end{bmatrix} \tag{2.36}$$

Note that since $\dot{\boldsymbol{\mathcal{P}}}$ is dependent on $\boldsymbol{\nu}$ and $\boldsymbol{\eta}$, this transformation needs to be performed in each iteration of the simulation.

2.4 Modified Vehicle Model

The model presented in Fossen[33, s9.9] is based on a vehicle without any actuators outside from the moving-mass system. When including additional thrusters and/or actuators, the damping of the system and environmental effects such as drag should also be included. Finally, including non-zero buoyancy could increase accuracy of the simulation, and should therefore be implemented. As such, the following implementations are added to the equations:

$\boldsymbol{\tau}_v$	Generalized applied control forces
$\boldsymbol{\tau}_{env}$	Generalized environmental forces
$\boldsymbol{D}$	Linear damping
$\boldsymbol{g}_{rest}$	Restoring forces

(2.37)

Implementing these yield the new full model:

$$\dot{\boldsymbol{\mathcal{P}}}_p^b = -S(\boldsymbol{\nu}_2)\boldsymbol{\mathcal{P}}_p^b + \boldsymbol{R}_n^b \boldsymbol{f}_{gp}^n + \boldsymbol{\tau}_p \tag{2.38}$$

$$\dot{\boldsymbol{\mathcal{P}}}_b^b = -S(\boldsymbol{\nu}_2)\boldsymbol{\mathcal{P}}_v^b + \boldsymbol{R}_n^b \left(\boldsymbol{f}_{gp}^n + \boldsymbol{f}_g^n + \boldsymbol{f}_b^n\right) + \boldsymbol{\tau}_{v,1} + \boldsymbol{\tau}_{env,1} - \boldsymbol{D}_1\boldsymbol{\nu}_{1,r} \tag{2.39}$$

$$\dot{\mathcal{H}}^b = -S(\boldsymbol{\nu}_1)\boldsymbol{\mathcal{P}}^b - S(\boldsymbol{\nu}_2)\mathcal{H}^b + S(\boldsymbol{r}_{bp}^b)\boldsymbol{R}_n^b \boldsymbol{f}_{gp}^n + S(\boldsymbol{r}_{bg}^b)\boldsymbol{R}_n^b \boldsymbol{f}_g^n + \boldsymbol{\tau}_{v,2} + \boldsymbol{\tau}_{env,2} - \boldsymbol{D}_2\boldsymbol{\nu}_{2,r} \tag{2.40}$$

To simplify notation, the equations can be set in 9-DOF matrix form, resulting in:

$$\dot{\boldsymbol{\mathcal{P}}} = C(\boldsymbol{\nu})\boldsymbol{\mathcal{P}} + \boldsymbol{g}(\boldsymbol{r}^b)\boldsymbol{f}^b(\boldsymbol{\Theta_{nb}}) - \boldsymbol{D}\boldsymbol{\nu}_r + \boldsymbol{\tau}_{env} + \boldsymbol{\tau}_v \tag{2.41}$$

With:

$$\textit{(Coriolis and Centripetal Matrix)}\ \boldsymbol{C}(\boldsymbol{\nu}) = \begin{bmatrix} -S(\boldsymbol{\nu}_2) & 0 & 0 \\ 0 & -S(\boldsymbol{\nu}_2) & 0 \\ 0 & -S(\boldsymbol{\nu}_1) & -S(\boldsymbol{\nu}_2) \end{bmatrix} \tag{2.42}$$

$$\textit{(Restoring Matrix)}\ \boldsymbol{g}(\boldsymbol{r}^b) = \begin{bmatrix} \boldsymbol{I}_3 & \boldsymbol{I}_3 & \boldsymbol{I}_3 \\ \boldsymbol{I}_3 & \boldsymbol{I}_3 & \boldsymbol{I}_3 \\ S(\boldsymbol{r}^b_{bp}) & S(\boldsymbol{r}^b_{bg}) & \boldsymbol{I}_3 \end{bmatrix} \tag{2.43}$$

$$\textit{(Restoring Vector)}\ \boldsymbol{f}^b(\boldsymbol{\Theta_{nb}}) = \begin{bmatrix} \boldsymbol{R}^b_n \boldsymbol{f}^n_{gp} \\ \boldsymbol{R}^b_n \boldsymbol{f}^n_g \\ \boldsymbol{R}^b_n \boldsymbol{f}^n_b \end{bmatrix} \tag{2.44}$$

$$\textit{(Damping Matrix)}\boldsymbol{D} = \text{diag}([0, 0, 0, X_u, Y_v, Z_w, K_p, M_q, N_r]) \tag{2.45}$$

$$\textit{(Environmental Forces)}\ \boldsymbol{\tau}_{env} = \begin{bmatrix} \boldsymbol{0}_{3x1} \\ \boldsymbol{F}^b_{env} \\ S(\boldsymbol{r}^b_{bl})\boldsymbol{F}^b_{env} \end{bmatrix} \tag{2.46}$$

$$\textit{(Control Forces)}\ \boldsymbol{\tau}_c = \begin{bmatrix} \boldsymbol{\tau}_p \\ \boldsymbol{\tau}_{v,1} \\ \boldsymbol{\tau}_{v,2} \end{bmatrix} \tag{2.47}$$

2.5 Environmental Forces

The model is designed to support a vehicle with a fixed wing with an area A_{Cl} that generates lift, and to consider the drag using a constant projected area A_{Cd}. The resulting environmental force $\boldsymbol{F}^b_{env}$ is assumed to be applied in Center of Lift (CL) denoted by the vector $\boldsymbol{r}^b_{bl}$. The force is found by:

$$\boldsymbol{F}^b_{env} = \boldsymbol{R}^b_f \boldsymbol{F}^f_{env} \tag{2.48}$$

The environmental force in {f} can, as shown in Fossen[33, s2.5], be provided by:

$$\boldsymbol{F}^f_{env} = \begin{bmatrix} -F^f_{drag} \\ 0 \\ -F^f_{lift} \end{bmatrix} = \begin{bmatrix} -\frac{1}{2}\rho_w U_r^2 A_{Cd} C_{Dl}(\alpha) \\ 0 \\ -\frac{1}{2}\rho_w U_r^2 A_{Cl} C_{Ll}(\alpha) \end{bmatrix} \tag{2.49}$$

With:

ρ_w	Density of water (Assumed constant) $\frac{kg}{m^3}$
U_r	Relative vehicle velocity $[\frac{m}{s}]$
A_{Cd}	Projected vehicle drag area $[m^2]$
A_{Cl}	Vehicle wing area $[m^2]$
$C_{Dl}(\alpha)$	Drag coefficient
$C_{Cl}(\alpha)$	Lift coefficient

(2.50)

2.5.1 Drag and Lift Coefficients

The drag coefficient is modeled as linear drag:

$$C_{Dl}(\alpha) = Cd|\alpha_r| \tag{2.51}$$

The lift coefficient is also modeled linearly, however, to prevent the wings from generating greater lift for angles of attack larger than stall angle $\alpha > \alpha_{stall}$, the coefficient calculation is modified such that if the angle of attack increases over the stall condition, the lift linearly decreases from that point. Namely, considering:

$$\begin{array}{c|c} \text{Stall angle} & \alpha_{stall} \\ \text{Maximum angle of attack} & \alpha_{max} \\ \text{Maximum Lift coefficient size} & Cl_{max} \end{array} \tag{2.52}$$

Yields the lift coefficient:

$$C_{Cl}(\alpha_r) = \begin{cases} \frac{Cl_{max}}{\alpha_{stall}}\alpha_r \;\mid\; \alpha_r < \alpha_{stall} \\ Cl_{max}\frac{\alpha_{max}-\alpha_r}{\alpha_{max}-\alpha_{stall}} \;\mid\; else \end{cases} \tag{2.53}$$

Using this ensures the following properties:

$$C_{Cl}(\alpha_{stall}) = Cl_{max} \tag{2.54}$$
$$C_{Cl}(\alpha_{max}) = 0 \tag{2.55}$$
$$\dot{C}_{Cl}(\alpha \in [0, \alpha_{stall} >) > 0 \tag{2.56}$$
$$\dot{C}_{Cl}(\alpha \in < \alpha_{stall}, \alpha_{max}]) < 0 \tag{2.57}$$

Which results in similar lift and drag coefficient as discussed by Tangler and Kocurek [32]. The figure showing their discussed lift and drag calculations and verifications is provided in the appendix of this thesis as Figure A.4.

2.6 Linear Damping

The damping of the vehicle can be specified based on pole-placement. Neglecting the Coriolis and Centripetal effects and examining the system for $\sum \tau = 0$:

$$\dot{\boldsymbol{\mathcal{P}}} = \boldsymbol{g}(\boldsymbol{r}^b)\boldsymbol{f}^b(\boldsymbol{\Theta_{nb}}) - \boldsymbol{D\nu} \tag{2.58}$$
$$= \boldsymbol{G}(\boldsymbol{\eta}) - \boldsymbol{D\nu} \tag{2.59}$$

$$\boldsymbol{M}(\boldsymbol{r}^b_{bp})\dot{\boldsymbol{\nu}} + \boldsymbol{D\nu} - \boldsymbol{G}(\boldsymbol{\eta}) = \vec{\boldsymbol{0}} \tag{2.60}$$
$$\dot{\boldsymbol{\nu}} + \boldsymbol{M}^{-1}(\boldsymbol{r}^b_{bp})\boldsymbol{D\nu} - \boldsymbol{M}^{-1}(\boldsymbol{r}^b_{bp})\boldsymbol{G}(\boldsymbol{\eta}) = \vec{\boldsymbol{0}} \tag{2.61}$$

Linearizing the equation around $\boldsymbol{\eta}_0 = \vec{\boldsymbol{0}}$ and comparing to the characteristic equation yields:

$$\dot{\boldsymbol{\nu}} + \boldsymbol{M}^{-1}(\boldsymbol{r}^b_{bp})\boldsymbol{D\nu} - \boldsymbol{M}^{-1}(\boldsymbol{r}^b_{bp})(\boldsymbol{G}^*\boldsymbol{\eta} + \boldsymbol{G_0}) = \vec{\boldsymbol{0}} \tag{2.62}$$
$$\dot{\boldsymbol{\nu}} + 2\boldsymbol{\mathcal{Z}\Omega\nu} + \boldsymbol{\Omega}^2\boldsymbol{\eta} = \vec{\boldsymbol{0}} \tag{2.63}$$
$$\rightarrow -\boldsymbol{M}^{-1}(\boldsymbol{r}^b_{bp})(\boldsymbol{G}^*\boldsymbol{\eta} + \boldsymbol{G_0}) = \boldsymbol{\Omega}^2 \tag{2.64}$$
$$\boldsymbol{M}(\boldsymbol{r}^b_{bp})\,(2\boldsymbol{\mathcal{Z}\Omega}) = \boldsymbol{D} \tag{2.65}$$

Which could, on paper, provide a bandwidth matrix $\boldsymbol{\Omega}$ which then could be combined with a design parameter damping matrix $\boldsymbol{\mathcal{Z}}$ to find the damping matrix of the system:

$$\boldsymbol{\Omega} = \sqrt{-\boldsymbol{M}^{-1}(\boldsymbol{r}^b_{bp})\boldsymbol{G}^*} \tag{2.66}$$
$$\boldsymbol{\mathcal{Z}}\ \textit{Design parameter matrix} \tag{2.67}$$
$$\boldsymbol{D} = \boldsymbol{M}(\boldsymbol{r}^b_{bp})\,(2\boldsymbol{\mathcal{Z}\Omega}) \tag{2.68}$$

Assuming the term G_0 is handled by a control torque in τ. The linearized gravity matrix $\boldsymbol{G}^*\boldsymbol{\eta}$ can be found by using the small angle approximation for the rotation matrix [33, eq2.32]:

$$\boldsymbol{G}(\boldsymbol{\eta}) = \boldsymbol{g}(\boldsymbol{r}^b)\boldsymbol{f}^b(\boldsymbol{\Theta_{nb}}) \tag{2.69}$$

$$= \begin{bmatrix} \boldsymbol{R}_n^b \boldsymbol{f}_{g,p}^n \\ \boldsymbol{R}_n^b \left(\boldsymbol{f}_{g,p}^n + \boldsymbol{f}_g^n + \boldsymbol{f}_b^n \right) \\ S(\boldsymbol{r}_{bp}^b)\boldsymbol{R}_n^b \boldsymbol{f}_{g,p}^n + S(\boldsymbol{r}_{bg}^b)\boldsymbol{R}_n^b \boldsymbol{f}_g^n \end{bmatrix} \tag{2.70}$$

Inserting the linearized rotation matrix:

$$\boldsymbol{R}_b^n \approx \begin{bmatrix} 1 & -\psi & \theta \\ \psi & 1 & -\phi \\ -\theta & \phi & 1 \end{bmatrix} \rightarrow \boldsymbol{R}_n^b = (\boldsymbol{R}_b^n)^T = \begin{bmatrix} 1 & \psi & -\theta \\ -\psi & 1 & \phi \\ \theta & -\phi & 1 \end{bmatrix} \tag{2.71}$$

Yields the linearized restoring forces:

$$\boldsymbol{G}(\boldsymbol{\eta}) \approx \begin{bmatrix} \begin{bmatrix} -\theta \\ \phi \\ 1 \end{bmatrix} m_p g \\ \begin{bmatrix} -\theta \\ \phi \\ 1 \end{bmatrix} g(m_v + m_p - V_v \rho_w) \\ \begin{bmatrix} 0 & 0 & 0 \\ 0 & 0 & -r_{bp,x}^b \\ 0 & r_{bp,x}^b & 0 \end{bmatrix} \begin{bmatrix} -\theta \\ \phi \\ 1 \end{bmatrix} m_p g + \begin{bmatrix} 0 & -r_{bg,z}^b & 0 \\ r_{bg,z}^b & 0 & 0 \\ 0 & 0 & 0 \end{bmatrix} \begin{bmatrix} -\theta \\ \phi \\ 1 \end{bmatrix} m_v g \end{bmatrix} \tag{2.72}$$

$$= \begin{bmatrix} 0 & 0 & 0 & 0 & 0 & 0 & 0 & -m_p g & 0 \\ 0 & 0 & 0 & 0 & 0 & 0 & m_p g & 0 & 0 \\ 0 & 0 & 0 & 0 & 0 & 0 & 0 & 0 & 0 \\ 0 & 0 & 0 & 0 & 0 & 0 & 0 & -g(m_p + m_v - V_v \rho_w) & 0 \\ 0 & 0 & 0 & 0 & 0 & 0 & g(m_p + m_v - V_v \rho_w) & 0 & 0 \\ 0 & 0 & 0 & 0 & 0 & 0 & 0 & 0 & 0 \\ 0 & 0 & 0 & 0 & 0 & 0 & -r_{bg,z}^b m_v g & 0 & 0 \\ 0 & 0 & 0 & 0 & 0 & 0 & 0 & -r_{bg,z}^b m_v g & 0 \\ 0 & 0 & 0 & 0 & 0 & 0 & r_{bp,x}^b & 0 & 0 \end{bmatrix} \begin{bmatrix} \boldsymbol{r}_{bp}^b \\ \boldsymbol{\eta} \end{bmatrix} \tag{2.73}$$

$$+ \begin{bmatrix} 0 \\ 0 \\ m_p g \\ 0 \\ 0 \\ g(m_p + m_v - V_v \rho_w) \\ 0 \\ -r_{bp,x}^b m_p g \\ 0 \end{bmatrix} \tag{2.74}$$

$$= \boldsymbol{G}^* \boldsymbol{\eta} + \boldsymbol{G_0} \tag{2.75}$$

However, since the restoring forces only provide a spring coefficient in θ and ϕ, determining a filled bandwidth matrix $\boldsymbol{\Omega}$ as in equation 2.66 is not possible, since this configuration leaves the matrix $-\boldsymbol{M}^{-1}\boldsymbol{G}^*$ singular.

2.6.1 Diagonal, Decoupled Damping

Instead of determining the damping using the full, coupled system, each damping can be examined considering separate, decoupled DOF. UAVs are commonly designed with CG under the CB such that the equilibrium $\theta = \phi = 0$ is stable. Such designs results in a spring coefficient resulting from the restoring forces, and can therefore be modeled similarly the the filled matrix approach (eq. (2.66)-(2.68)):

$$\omega_i = \sqrt{-\frac{M_{ii}}{G^*_{ii}}} \tag{2.76}$$

$$\zeta_i = \textit{Design parameter} \tag{2.77}$$

$$D_{ii} = M_{ii} 2\zeta_i \omega_i \tag{2.78}$$

$$i \in \{\theta, \phi\} \tag{2.79}$$

However, since the restoring forces only act as a spring in roll and pitch, the remaining DOF must be determined by other methods. These dynamics are more closely describable by:

$$\dot{\boldsymbol{\mathcal{P}}} = -\boldsymbol{D}\boldsymbol{\nu} \tag{2.80}$$

$$\boldsymbol{M}(\boldsymbol{r}^b_{bp})\dot{\boldsymbol{\nu}} + \boldsymbol{D}\boldsymbol{\nu} = 0 \tag{2.81}$$

$$\boldsymbol{D}^{-1}\boldsymbol{M}(\boldsymbol{r}^b_{bp})\dot{\boldsymbol{\nu}} + \boldsymbol{\nu} = 0 \tag{2.82}$$

This can be compared to the Nomoto model as presented in Fossen[33, eq15.105]:

$$T\dot{\boldsymbol{\nu}} + \boldsymbol{\nu} = 0 \tag{2.83}$$

$$\rightarrow \boldsymbol{D}^{-1}\boldsymbol{M}(\boldsymbol{r}^b_{bp}) = T \tag{2.84}$$

$$\boldsymbol{D} = \boldsymbol{M}(\boldsymbol{r}^b_{bp})\boldsymbol{T}^{-1} \tag{2.85}$$

Where T is a diagonal matrix of specifiable time constants for each DOF. Then, the complete damping matrix can be determined as:

$$D_{ii} = \begin{cases} M_{ii}(2\zeta_i\omega_i),\ \omega_i = \sqrt{-\boldsymbol{M}_{ii}^{-1}G^*_{ii}} & i \in \{\theta, \phi\} \\ \frac{M_{ii}}{T_i} & i \in \{x, y, z, \psi\} \\ 0 & i \in \{x_{pm}, y_{pm}, z_{pm}\} \end{cases} \tag{2.86}$$

$$\boldsymbol{D} = \text{diag}(D_{11}, D_{22}, ..., D_{99}) \tag{2.87}$$

Where M_{ii} is the inertia, including added mass, of the decoupled DOF i:

$$\begin{array}{llll} \textit{(Linear)} & M_x = (m_v + X_{\dot{u}}) & M_y = (m_v + Y_{\dot{v}}) & M_z = (m_v + Z_{\dot{w}}) \\ \textit{(angular)} & M_\phi = (I_{xx} + K_{\dot{p}}) & M_\theta = (I_{yy} + M_{\dot{q}}) & M_\psi = (I_{zz} + M_{\dot{r}}) \end{array}$$

The spring coefficient in pitch and roll resulting from the restoring forces, $\boldsymbol{G}^*$, can be determined by examining the restoring forces in the pitch channel in CO, as shown in figure 2.1. There, we see that for a CG with an offset $\boldsymbol{r}^b_{bg,z}$ in z^b and a pitch θ, a force (shown in red) will with this offset generate a pitch torque equal to:

$$\boldsymbol{G}(\boldsymbol{\eta})_\theta = r^b_{bg,z} m_v g \sin(-\theta) \tag{2.88}$$

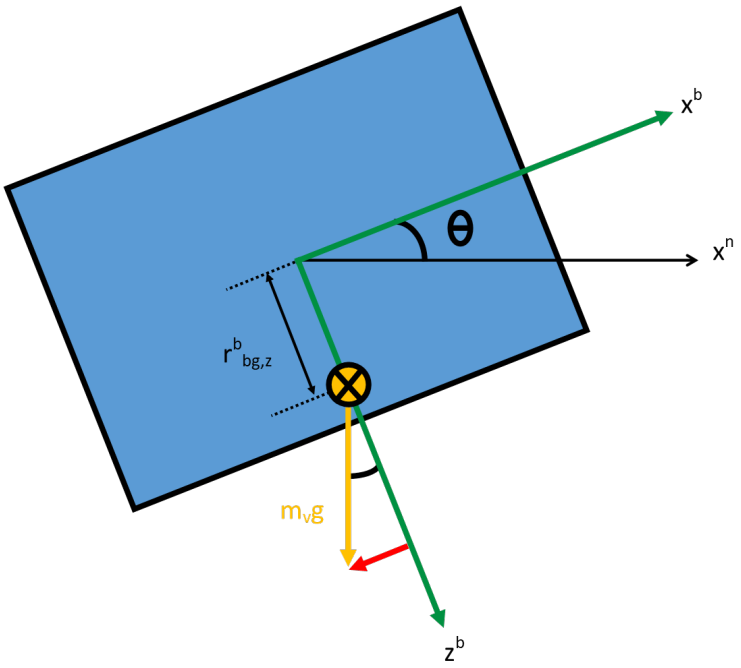

Figure 2.1: Restoring spring force in pitch from CG offset

Using small-angle approximation, the equation can be linearized around $\theta_0 = 0$:

$$G(\eta)_\theta \approx G^*_\theta \theta = r^b_{bg,z} m_v g(-\theta) \tag{2.89}$$

$$G^*_\theta = -r^b_{bg,z} m_v g \tag{2.90}$$

Similarly in roll channel:

$$\boldsymbol{G}(\boldsymbol{\eta})_\phi = r^b_{gp,z} m_v g \sin(-\phi) \tag{2.91}$$

$$G^*_\phi = -r^b_{gp,z} m_v g \tag{2.92}$$

Note that this is only applied to vehicles with a CG offset in z^b.

2.6.2 Combined Damping Model

To better consider how the moving mass actuation affect the damping of the system, a combined damping model is implemented in this thesis. The approach first determines a base damping:

$$D^*_i = \begin{cases} 2\zeta_i \omega_i, \ \omega_i = \sqrt{-\boldsymbol{M}_i^{-1} \boldsymbol{G}^*} & i \in \{\theta, \phi\} \\ \frac{1}{T_i} & i \in \{x, y, z, \psi\} \\ 0 & i \in \{x_{pm}, y_{pm}, z_{pm}\} \end{cases} \tag{2.93}$$

$$\boldsymbol{D}^* = \text{diag}(D^*_1, D^*_2, ..., D^*_3) \tag{2.94}$$

The inertia matrix M is then applied in each iteration to determine the time-varying damping matrix D:

$$\boldsymbol{D} = \boldsymbol{M}(\boldsymbol{r}^b_{bp}(t)) \boldsymbol{D}^* \tag{2.95}$$

2.7 Control Forces

In order to control the system, the simulation includes several actuator forces:

$$\begin{array}{c|c} \text{Moving-mass-actuator (MMA)} & \boldsymbol{\tau}_p \\ \text{Main Thruster} & \boldsymbol{F}^b_{thrust} \\ \text{Dive-planes} & \boldsymbol{F}_{dp} \end{array} \tag{2.96}$$

These forces are transformed to generalized forces by:

$$\boldsymbol{\tau}_p = \begin{bmatrix} \boldsymbol{F}^b_p \\ \vec{\mathbf{0}}_3 \\ \vec{\mathbf{0}}_3 \end{bmatrix} \tag{2.97}$$

$$\boldsymbol{\tau}_v = \begin{bmatrix} \vec{\mathbf{0}}_3 \\ \boldsymbol{F}^b_{thrust} \\ S(\boldsymbol{r}^b_{bt})\boldsymbol{F}^b_{thrust} \end{bmatrix} \tag{2.98}$$

$$\boldsymbol{\tau}_{dp} = \begin{bmatrix} \vec{\mathbf{0}}_3 \\ \boldsymbol{F}_{dp} \\ S(\boldsymbol{r}^b_{bdp})\boldsymbol{F}_{dp} \end{bmatrix} \tag{2.99}$$

Where $\boldsymbol{r}^b_{bi}$ denotes the distance from CO to C_i in {b}, namely:

$$\begin{array}{c|l} \boldsymbol{r}^b_{bt} & \text{Thruster acting point} \\ \boldsymbol{r}^b_{bdp} & \text{Diveplane acting point} \end{array} \tag{2.100}$$

The force generated by the dive-plane $\boldsymbol{F}_{dp}$ is defined similarly as the environmental forces (eq. 2.49):

$$\boldsymbol{F}^f_{dp} = \begin{bmatrix} -F_{dp,drag} \\ 0 \\ F_{dp,lift} \end{bmatrix} \tag{2.101}$$

$$= \begin{bmatrix} -\frac{1}{2}\rho_w U_r^2 A_{dp} C_{dp} \delta_{dp}^2 \\ 0 \\ \frac{1}{2}\rho_w U_r^2 A_{dp} C_{dp} \delta_{dp} \end{bmatrix} \tag{2.102}$$

As provided in Fossen[33, s9.7]. Note that the sign of $F_{dp,lift}$ is dependent on the vehicle design, namely which direction of δ_{dp} is defined positive.

Chapter 3

Design of AUV controllers

The AUV modeled in this thesis requires controllers for the MMA, dive-planes and the surge velocity subsystem.

3.1 Surge Velocity Subsystem

The thrust $\boldsymbol{F}^b_{thrust}$ can be used to control the surge velocity u by its x-component, namely:

$$\boldsymbol{F}^b_{thrust,x} = F_u \tag{3.1}$$

A controller for the decoupled system can then be implemented. In this thesis, a PI controller is implemented as:

$$K_{p,u} = m_v \omega_u^2 \tag{3.2}$$

$$K_{i,u} = \frac{1}{10} K_{p,u} \tag{3.3}$$

Enabling the surge velocity to be controlled by regulating the force F_u:

$$F_u = K_{p,u} e_u + K_{i,u} u_{int} \tag{3.4}$$

$$\dot{u}_{int} = e_u \tag{3.5}$$

3.2 Moving-Mass Controller

First, the effect of the restoring forces acting on the point-mass is considered:

3.2.1 Restoring Forces on Point-Mass

Since the point-mass is completely enveloped within the vehicle, the only restoring forces that act on the point-mass is gravity. The restoring forces acting on the point-mass in body frame are thereby described in 3-DOF as:

$$\boldsymbol{\tau}^b_{rest,pm} = \boldsymbol{R}^b_n \boldsymbol{f}^n_{gp} \tag{3.6}$$

This contribution to the total force applied to the point-mass needs to be removed by the controller, and as such, the holding the point-mass in place within the vehicle against the restoring forces, the force applied to the point-mass is set to:

$$\boldsymbol{\tau}_p = -\boldsymbol{\tau}^b_{rest,pm} = -\boldsymbol{R}^b_n \boldsymbol{f}^n_{gp} \tag{3.7}$$

This assumes that the mass m_p and the relevant attitude angles are known.

3.2.2 Steady-State Control Law

Now, consider the decoupled steady-state ($\ddot{\theta} = \dot{\theta} = 0$) pitch dynamics with only MMA and restoring forces:

$$M_\theta \ddot{\theta} = 0 = \boldsymbol{\tau}_{mm} + \boldsymbol{\tau}_g \tag{3.8}$$

$$= m_p g(-r^b_{bp,x}\cos(\theta)) - m_v g r^b_{bg,z}\sin(\theta) \tag{3.9}$$

$$\rightarrow m_p g r^b_{bp,x}\cos(\theta) = m_v g r^b_{bg,z}\sin(\theta) \tag{3.10}$$

$$-r^b_{bp,x}\frac{m_p}{m_v}\frac{1}{r^b_{bg,z}} = \tan(\theta) \tag{3.11}$$

$$r^b_{bp,x}(\theta) = -\frac{m_v}{m_p} r^b_{bg,z}\tan(\theta) \tag{3.12}$$

$$r^b_{bp,x}(\theta) = -\frac{1}{\sigma_p} r^b_{bg,z}\tan(\theta) \tag{3.13}$$

With mass ratio $\sigma_p = \frac{m_p}{m_v}$. This provides us with a relation for the steady-state pitch angle and MMA actuation required to hold that angle. Additionally, it can be used to describe the maximum pitch θ_{max} obtainable for a maximum $r^b_{bp,x,max}$ MMA actuation:

$$r^b_{bp,x,max} = -\frac{1}{\sigma_p} r^b_{bg,z}\tan(\theta_{max}) \Leftrightarrow \theta_{max} = \tan^{-1}\left(-\sigma_p \frac{r^b_{bp,x,max}}{r^b_{bg,z}}\right) \tag{3.14}$$

This provides an explicit, open-loop control law for $r^b_{bp,x,d}$:

$$r^b_{bp,x,d} = -\frac{1}{\sigma_p} r^b_{bg,z}\tan(\theta_d) \tag{3.15}$$

Assuming that the controller is able to follow the reference signal θ_d. However, for $\theta_d > \theta_{max}$, the reference signal will exceed the maximum actuation $r^b_{bp,x,d} > r^b_{bp,x,max}$. Therefore, the pitch reference signal should be saturated to prevent this:

$$\bar{\theta}_d = \text{sat}(\theta_d, -\theta_{max}, \theta_{max}) \tag{3.16}$$

$$r^b_{bp,x,d} = -\frac{1}{\sigma_p} r^b_{bg,z}\tan(\bar{\theta}_d) \tag{3.17}$$

The controller determining τ_p is then implemented as a common PD controller:

$$\tau_p = K_{p,mm}(r^b_{bp,x,d} - r^b_{bp,x}) + K_{d,mm} v^b_{bp,x} \tag{3.18}$$

The derivative gain is implemented to ensure that the point-mass does not overshoot. That is, with critical damping $\zeta_{mm,x} > 1$, it prevents the mass from colliding the the end of the actuation length. The PD gain is determined using the PID pole-placing algorithm presented in Fossen[33, s15.3]: Note that the moved mass is modeled without damping and/or spring force ($k = d = 0$). The control law for the point-mass is then applied as:

$$\boldsymbol{\tau}_{mm} = -\boldsymbol{\tau}^b_{rest,pm} + \begin{bmatrix} K_{p,mm} e_{pm,x} + K_{d,mm} v^b_{b,pm} \\ 0 \\ 0 \end{bmatrix} \tag{3.19}$$

P(I)D pole-placement for MMA	
For specified bandwidth:	$\omega_b > 0$
And specified damping ratio:	$\zeta > 0$
Compute natural frequency:	$\omega_n = \frac{1}{\sqrt{1-2\zeta^2+\sqrt{4\zeta^4-4\zeta^2+2}}}\omega_b$
Compute P gain:	$K_p = m_v\omega_n^2$
Compute D gain:	$K_d = 2\zeta\omega_n m_v$

Note that countering the restoring forces can require a control torque in y^b_{pm} and z^b_{pm}. For this MMA system, the moved mass is actuated in x^b_{pm} and the other forces are assumed to be provided by the vehicle as the point-mass is locked in y^b_{pm} and z^b_{pm}.

3.3 Dive-Plane Controller

A similar approach can be used to determine an explicit, open-loop control law for the dive-plane actuation δ_{dp}. Considering the steady-state pitch dynamics ($\ddot{\theta} = \dot{\theta} = 0$) without dive-plane drag:

$$\sum \tau = \tau_{rest} + \tau_{mm} + \tau_{dp} = 0 \tag{3.20}$$

$$\rightarrow -m_v g \sin(\theta) r^b_{bg,z} - m_p g \cos(\theta) r^b_{bp,x} + \frac{1}{2}\rho_w U_r^2 A_{dp} C_{dp} \delta_{dp} r^b_{bdp,x} = 0 \tag{3.21}$$

Assuming small α_r and neglecting the drag induced from the dive-planes, as an approximation for the controller. The law also assumes that the pitch dynamics are decoupled from the remaining DOF, including couplings from coriolis and centripetal forces. To simplify notation, the equation is changed to amplitude-phase form:

$$A_\theta(r^b_{bp,x}) := g\sqrt{(m_v r^b_{bg,z})^2 + (m_p r^b_{gp,x})^2} \tag{3.22}$$

$$\phi_\theta(r^b_{bp,x}) := \text{atan2}(-m_v r^b_{bg,z}, -m_p r^b_{bp,x}) + \frac{\pi}{2} \tag{3.23}$$

$$\rightarrow A_\theta \sin(\theta - \phi_\theta) + \frac{1}{2}\rho_w U_r^2 A_{dp} C_{dp} \delta_{dp} r^b_{bdp,x} = 0 \tag{3.24}$$

This equation has similar properties as equation 3.14 in the sense that it relates the pitch angle θ to actuation parameters, however in this case the equation includes both δ_{dp} and $r^b_{bp,x}$. Assuming the moving-mass actuation $r^b_{bp,x}$ acts independent of the dive-planes (which is true when using the control law suggested in section 3.2), the equation can be used to relate the dive-plane actuation δ_{dp} with the pitch angle θ:

$$\frac{1}{2}\rho_w U_r^2 A_{dp} C_{dp} \delta_{dp} r^b_{bdp,x} \ = \tau_{dp} = -A_\theta \sin(\theta - \phi_\theta) \tag{3.25}$$

$$\delta_{dp} = -\frac{2}{\rho_w U_r^2 A_{dp} C_{dp} r^b_{bdp,x}} A_\theta \sin(\theta - \phi_\theta) \ \Leftrightarrow \ \theta = \text{asin}\left(-\frac{1}{A_\theta}\frac{1}{2}\rho_w U_r^2 A_{dp} C_{dp} \delta_{dp} r^b_{bdp,x}\right) + \phi_\theta \tag{3.26}$$

This equation can be used as a control law for the dive-planes:

$$\delta_{dp,d} = -\frac{2}{\rho_w U_r^2 A_{dp} C_{dp} r^b_{bdp,x}} A_\theta \sin(\theta_d - \phi_\theta) \tag{3.27}$$

Note that this control law is dependent on the relative velocity U_r^2.

Sidenote: MMA control law including dive-plane contributions

The equation 3.21 can also be used to create a control law for $r^b_{bp,d}$:

$$-m_v g \sin(\theta) r^b_{bg,z} - m_p g \cos(\theta) r^b_{bp,x} + \frac{1}{2}\rho_w U_r^2 A_{dp} C_{dp} \delta_{dp} r^b_{bdp,x} = 0 \tag{3.28}$$

$$r^b_{bp,x,d} = -\frac{1}{\sigma_p}\tan(\theta_d) r^b_{bg,z} + \frac{1}{m_p g \cos(\theta_d)}\frac{1}{2}\rho_w U_r^2 A_{dp} C_{dp} \delta_{dp} r^b_{bdp,x} \tag{3.29}$$

However, due to the actuation limit $r^b_{bp,x,max}$, implementing this control law would result in a maximum MMA outside the defined maximum, and the previous control law should be used instead.

Depth Control

Considering depth control, we desire to regulate $\boldsymbol{\eta}$, namely the z^n position of the craft, to generate a pitch reference θ_d.

3.4 Maximum Pitch

The simplest approach to depth control is to implement a saturated PD-controller such that the generated pitch is limited to $\theta \in (-\frac{\pi}{2}, \frac{\pi}{2})$. However, considering that as the pitch increases to $\theta \to \pm\frac{\pi}{2}$, the effective torque in pitch generated by the moving mass decreases to $\tau_{mm} \to 0$.
As such, the maximum pitch should be specified to a smaller value to ensure that θ_d doesn't negate the effectiveness of the MMA. Using this controlling technique will result in the vehicle using the maximum pitch available (limited to the predefined saturation limit θ_{max}) as the pitching reference θ_d while the vehicle is far away from its desired depth target z^n_d.

However, θ_{max} should consider not only that the effectiveness of MMA decreases drastically for $\theta \to \pm\frac{\pi}{2}$, but also that the maximum pitch in steady-state descent that the actuators can provide due to their saturation limits. With this approach, the maximum pitch would have to be predefined, or an offset in pitch during diving/rising- maneuvers would have to be accepted. An offset would create reference signals that are more aggressive than necessary and creates integrator windup if an integrator were to be implemented in the controller. However, the relation between the pitch angle θ and the actuators can be described by eq. 3.14 (for MMA only) and 3.26 (for MMA and DP actuation).

3.4.1 Maximum pitch for MMA only

The maximum pitching angle of a vehicle with only MMA and no dive-planes is provided by equation 3.14, reciting:

$$\theta_{max} = \tan^{-1}\left(-\sigma_p \frac{r^b_{bp,x,max}}{r^b_{bg,z}}\right) \tag{3.30}$$

In this equation we note that the maximum pitch is essentially limited by the ratio $\frac{m_p r^b_{bp,x}}{m_v r^b_{bg,z}}$. As such, the maximum actuation of MMA can be improved either by increasing the point-mass to vehicle-mass ratio σ_p, by implementing a greater actuation limit for $r^b_{bp,x}$ or by designing a vehicle

with smaller $r^b_{bg,z}$. Increasing σ_p effectively means increasing the mass m_p which either increases power requirement or decreases MMA response in addition to adding more mass to the vehicle. Increasing $r^b_{bp,x,max}$ does not add more mass to the vehicle, but reaching maximum actuation takes longer or requires more power and requires more space within the vehicle. Decreasing $r^b_{bg,z}$ in design is optimal considering MMA, however, since this distance stabilizes the pitch- and roll- channel, decreasing it will also decrease overall system stability. This approach also constrains the overall design of the vehicle.

3.4.2 Maximum pitch for MMA and dive-planes

The pitch angle can be determined as a function of both the MMA and dive-plane actuation, as shown in eq. 3.26. Following the equation, the maximum pitch can be determined as:

$$F_{dp,max}(U_r^2) = \frac{1}{2}\rho_w U_r^2 A_{dp} C_{dp} \delta_{dp,max} \cos(\alpha_r) \tag{3.31}$$

$$A_{\theta,max} = g\sqrt{(m_v r^b_{bg,z})^2 + (m_p r^b_{bp,max})^2} \tag{3.32}$$

$$\phi_{\theta,max} = atan2(-m_v r^b_{bg,z}, -m_p r^b_{bp,max}) + \frac{\pi}{2} \tag{3.33}$$

$$\theta_{max} = \text{asin}\left(-\frac{1}{A_{\theta,max}} F_{dp,max} r^b_{b,dpx}\right) + \phi_{\theta,max} \tag{3.34}$$

Note that since the force $F_{dp,max}$ from the dive-planes are dependent on the relative velocity, the maximum pitch angle is also dependent on the maximum relative velocity in pitch steady-state conditions. There are several methods that can be used to solve this issue:

- Determine $U_{r,max}$ by experimentation and/or simulation
- Determine $U_{r,max}$ explicitly based on vehicle parameters
- Implement variable θ_{max} that use feedback of velocity measurements

The equilibrium equation 3.26 can be rewritten to describe the relative velocity:

$$U_r = \sqrt{\frac{2}{A_{dp} C_{dp} \rho_w} \frac{1}{\delta_{dp,max}} A_{\theta_{max}} \sin(\theta_{max} - \phi_{\theta_{max}})} \tag{3.35}$$

However this function is dependent on the maximum pitch angle θ_{max} meaning attempting to define both $U_{r,max}$ and θ_{max} results in one equation with two unknowns. Other equations that can be examined includes velocity equilibrium in v^b_{nb}, however these equations prove too cumbersome to calculate U_r explicitly. As such, the maximum pitch available is calculated each iteration in the simualtion, following equation 3.26.

3.5 Maximum Rising and Descending Rate

So far, the maximum rise and descent rate has been assumed to occur at the maximum absolute pitch angles. The forces acting on the body in NED are:

- $\tau_g = g(m_v + m_p - V_v \rho_w)$
- $\tau_{thrust} = F^b_{thrust} \sin(-\theta)$
- $\tau_{lift} = -F^b_{lift} \cos(\theta) = -\frac{1}{2}\rho_w U_r^2 (A_{cl}\alpha_r - A_{dp} C_{dp} \delta_{dp}) \cos(\theta)$

- $\tau_{drag} = F^b_{drag} \sin(\theta) = \frac{1}{2}\rho_w U_r^2 (A_{cd} C_d \alpha_r + A_{dp} C_{dp} \delta_{dp}^2) \sin(\theta)$

Then, the decoupled dynamics for z^n can be described by:

$$M_z \ddot{z}^n + D_z \dot{z}^n = \tau_z \tag{3.36}$$
$$\tau_z = \tau_g - F_{lift} \cos(\theta) - (F_{thrust} - F_{drag}) \sin(\theta) \tag{3.37}$$
$$\tag{3.38}$$

Where equation 3.37 relates the pitching angle θ with the associated force τ_z in z^n. This expression may then be solved for θ based on several methods:

Linear (1st order) approximation

Equation 3.37 can be approximated considering small angles such that $\cos(\theta) \approx 1$ and $\sin(\theta) \approx \theta$:

$$\tau_{z,d} = \tau_g - F_{lift} \cos(\theta_d) - (F_{thrust} - F_{drag}) \sin(\theta_d) \tag{3.39}$$
$$\approx \tau_g - F_{lift} - (F_{thrust} - F_{drag}) \theta_d \tag{3.40}$$
$$\theta_d \approx \frac{\tau_g - F_{lift} - \tau_{z,d}}{F_{thrust} - F_{drag}} \tag{3.41}$$

Note that this approach requires $F_{thrust} - F_{drag}$ to be nonzero.

Quadratic (2nd order) approximation

Instead of using $\cos(\theta) \approx 1$, the cosine function can be approximated by to second order approximation:

$$\cos(\theta) = 1 - 2\sin^2(\frac{1}{2}\theta) \tag{3.42}$$
$$\approx 1 - 2(\frac{1}{2}\theta)^2 \tag{3.43}$$
$$= 1 - \frac{1}{2}\theta^2 \tag{3.44}$$

Using this approximation in equation 3.37 yields:

$$\tau_{z,d} \approx \tau_g - F_{lift}(1 - \frac{1}{2}\theta_d^2) - (F_{thrust} - F_{drag})\theta_d \tag{3.45}$$
$$\rightarrow \frac{1}{2} F_{lift} \theta_d^2 \ - (F_{thrust} - F_{drag})\theta_d + \tau_g - F_{lift} - \tau_{z,d} = 0 \tag{3.46}$$

This expression can be solved using the quadratic formula:

$$\theta_d = \frac{1}{F_{lift}} \left[(F_{thrust} - F_{drag}) \pm \sqrt{(F_{thrust} - F_{drag})^2 - 2F_{lift}(\tau_g - F_{lift} - \tau_{z,d})} \right] \tag{3.47}$$

Firstly, this equation yields two solutions for θ_d. Additionally, the equation only provides a result in $\mathcal{R}$ when:

$$(F_{thrust} - F_{drag})^2 - 2F_{lift}(\tau_g - F_{lift} - \tau_{z,d}) \geq 0 \tag{3.48}$$

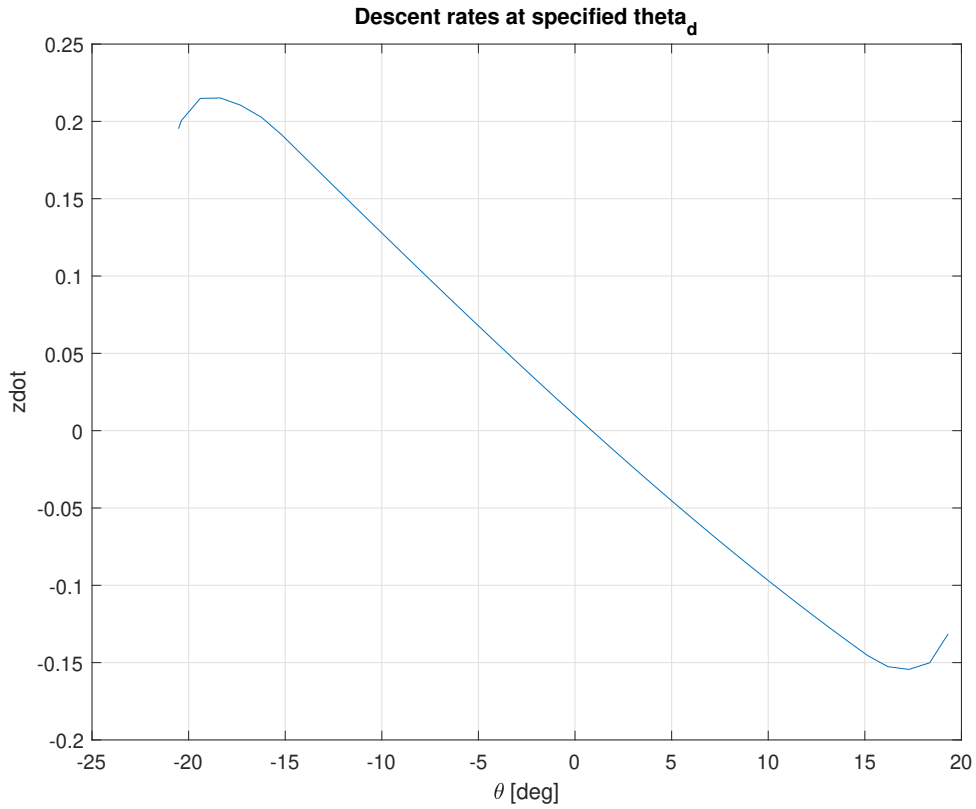

Figure 3.1: Demonstration of descent rate $\dot{z^n}$ over different pitch angles

Amplitude-phase form

Another alternative is to bring the equation to phase-amplitude form:

$$\tau_{z,d} = -F_{lift}\cos(\theta_d) - (F_{thrust} - F_{drag})\sin(\theta_d) + \tau_g \tag{3.49}$$

$$= A_z \sin(\theta_d - \phi_z) + \tau_g \tag{3.50}$$

$$A_z = \sqrt{(F_{thrust} - F_{drag})^2 + F_{lift}^2} \tag{3.51}$$

$$\phi_z = \tan^{-1}\left(\frac{-(F_{thrust} - F_{drag})}{-F_{lift}}\right) \tag{3.52}$$

However, as with the pitch equilibrium, this function is also dependent on the relative velocity U_r^2. So instead of determining the desired maximum pitch rate explicitly, it is found by simulation. That is, the descent rate can be simulated by performing a diving maneuver with steps in pitch angle to determine the steady-state descent rate $\dot{z}^n$. As a demonstration to see if the maximum descent rate occurs at the maximum pitch, such a simulation is performed, with the result presented in figure 3.1. There, we see that the descent rate and pitch angle mostly seem linearly dependent on each other. However, at the greatest pitch angles, the descending/ascending rate drops slightly, suggesting that the maximum pitch angle $\theta_{d,max}$ should be reduced slightly during maneuvers.

3.6 Depth Reference

To avoid large steps in e_z and to ensure that the inner $r^b_{bp,x}$ loop can be assumed constant relative to the outer loop θ_d, a reference model on z_d is implemented. A reference model of order two is implemented to ensure a smooth position and velocity reference. The bandwidth of the reference model is selected such that it is separated from the inner loop bandwidth by a factor of 10. The reference model is taken from Fossen[33, ch12] as:

$$A_{r_z} = \begin{bmatrix} 0 & 1 & 0 \\ 0 & 0 & 1 \\ -\omega_{r_z}^3 & -(2\zeta_{r_z}+1)\omega_{r_z}^2 & -(2\zeta_{r_z}+1)\omega_{r_z} \end{bmatrix} \tag{3.53}$$

$$B_{r_z} = \begin{bmatrix} 0 \\ 0 \\ \omega_{r_z}^3 \end{bmatrix} \tag{3.54}$$

$$\dot{r}_z = \begin{bmatrix} z_{lp} \\ \dot{z}_{lp} \\ \ddot{z}_{lp} \end{bmatrix} = A_{r_z} r_z + B_{r_z} z_{mes} \tag{3.55}$$

Velocity saturation

As the desired pitch angle approaches its maximum value, the descent rate will reach an equilibrium and will be unable to follow the reference model. To consider this, a velocity saturation is implemented in the reference model, as discussed by Fossen [33, eq12.14].

Chapter 4

Simulating Control Laws with Proposed Example Model

To demonstrate the controllers, actuators (and system in general), the configuration provided by Table 4 is proposed and used in simulations.

4.1 Demonstrating Pitch Control and Actuation

The pitch θ is actuated by the MMA system and the dive-planes. Using the parameters from chapter 4, the steady-state control law for MMA (section 3.2.2), and the explicit dive-plane control law presented in equation 3.27, the system is simulated for the following diving and rising maneuver:

$$z^n_{ref,raw} = \begin{cases} 0[m] & t \in [0, 50)[s] \\ 10[m] & t \in [50, 250)[s] \\ 0[m] & t \in [250, 600][s] \end{cases} \tag{4.1}$$

With the pitch reference θ_d generated by the proportional, non-linearly saturated controller and using the maximum pitch $\theta_{d,max}$ from MMA and dive-planes described by equation 3.26:

$$\theta_{max} = \text{asin}\left(-\frac{1}{A_{\theta,max}} F_{dp,max} r^b_{b,dpx}\right) + \phi_{\theta,max} \tag{4.2}$$

$$\theta_d = \theta_{max} \frac{2}{\pi}(-\text{atan}(K_{p,z} e_z)) \tag{4.3}$$

Performing the simulation yields the result shown in Figure 4.1. In spite of the dive-planes not maxing out and saturating, the explicit control law for δ_{dp} sufficiently manages to perform the desired maneuver.

Variable	Value	Unit	Description
	Environmental Constants		
g	9.81	$[\frac{m}{s^2}]$	Gravity constant
ρ_w	997	$[\frac{kg}{m^3}]$	Density of Water
	Vehicle Parameters		
b	0.2	$[m]$	Vehicle width
l	2.02	$[m]$	Vehicle length
h	0.2	$[m]$	Vehicle height
V_v	$b \cdot l \cdot h$	$[m^3]$	Volume displaced by vehicle
m_v	80	$[kg]$	Vehicle mass (without MMA)
m_p	1	$[kg]$	MMA mass size
σ_p	$\frac{m_p}{m_v}$	-	Moving-mass ratio
I_{xx}	$\frac{1}{12}m_v(b^2+l^2)$	$[kgm^2]$	Inertia in Roll
I_{yy}	$\frac{1}{12}m_v(l^2+h^2)$	$[kgm^2]$	Inertia in Pitch
I_{zz}	$\frac{1}{12}m_v(h^2+b^2)$	$[kgm^2]$	Inertia in Yaw
$\boldsymbol{I}_b^b$	$\begin{bmatrix} I_{xx} & 0 & 0 \\ 0 & I_{yy} & 0 \\ 0 & 0 & I_{zz} \end{bmatrix}$	$[kgm^2]$	Rotation Inertia Matrix
	(Linear) Added mass		
$X_{\dot{u}}$	0	$[kg]$	Added mass in u
$Y_{\dot{v}}$	95.54	$[kg]$	Added mass in v
$Z_{\dot{w}}$	95.54	$[kg]$	Added mass in w
$K_{\dot{p}}$	2.369	$[kgm^2]$	Added mass in p
$M_{\dot{q}}$	32.49	$[kgm^2]$	Added mass in q
$N_{\dot{r}}$	32.49	$[kgm^2]$	Added mass in r
$\boldsymbol{M}_A$	diag($[0, 0, 0, X_{\dot{u}}, Y_{\dot{v}}, Z_{\dot{w}}, K_{\dot{p}}, M_{\dot{q}}, N_{\dot{r}}]$	$[kg, kgm^2]$	Added mass matrix

Table 4.1: Proposed vehicle configuration for simulation (1)

		Position (r) vectors	
$\boldsymbol{r}_{bg}^{b}$	$[0, 0, 0.05]^T$	$[m]$	Vector from CO to CG (Center of Gravity)
$\boldsymbol{r}_{bb}^{b}$	$[0, 0, 0]^T$	$[m]$	Vector from CO to CB (Center of Buoyancy)
$\boldsymbol{r}_{bl}^{b}$	$[0, 0, 0]^T$	$[m]$	Vector from CO to CL (Center of Lift)
$\boldsymbol{r}_{bpx,max}^{b}$	$\frac{1}{2}l$	$[m]$	Maximum point-mass actuation in x^b
$\boldsymbol{r}_{bdp}^{b}$	$[-\frac{1}{2}l, 0, 0]^T$	$[m]$	Vector from CO to dive-planes
		Linear damping	
T_{X_u}	5	$[s]$	damping Time Coefficient in X_u
T_{Y_v}	5	$[s]$	damping Time Coefficient in Y_v
T_{Z_w}	5	$[s]$	damping Time Coefficient in Z_w
T_{N_r}	5	$[s]$	damping Time Coefficient in N_r
ζ_{K_p}	0.3	-	damping Coefficient in K_p
ζ_{M_q}	0.6	-	damping Coefficient in M_q
		Lift and Drag Coefficients	
A_{Cd}	0.05	$[m^2]$	Projected drag surface area
A_{Cl}	0.5	$[m^2]$	Lift surface Area
α_{stall}	25	$[deg]$	Angle of attack at which stalling behavior starts
α_{max}	90	$[deg]$	Maximum angle of attack
Cd_{const}	2	-	Linear drag model constant
A_{dp}	0.1	$[m^2]$	Dive-plane area
Cdp_{condt}	0.4	-	Linear dive-plane lift model constant
$\delta_{dp,lim}$	$[-45, 45]^T$	$[deg]$	Actuation limits of dive-planes
$\boldsymbol{F}_{thrust}^{b}$	$[15, 0, 0]^T$	$[N]$	Main thruster forces

Table 4.2: Proposed vehicle configuration for simulation (2)

Simulation variables			
Δt	0.01	$[s]$	Simulation time-step size
t_{end}	600	$[s]$	Simulation time stop
z^n_{ref}	$\begin{cases} 0 & t < 50 \\ -10 & t \in [50, 300) \\ 0 & t \in [300, t_{end}] \end{cases}$	-	z^n reference
Initial Conditions			
$\boldsymbol{\eta}_{init}$	$\vec{\mathbf{0}}^b$	$[m, deg]$	Initial NED position
$\boldsymbol{r}^b_{bp,init}$	$\vec{\mathbf{0}}^b$	$[m]$	initial point-mass body position
$\boldsymbol{\nu}_{init}$	$\vec{\mathbf{0}}^b$	$[\frac{m}{s}, \frac{1}{s}]$	Initial BODY velocities
Reference model			
$\dot{z^n}_{lim}$	$[-0.5, 0.5]$	$\frac{m}{s}$	Reference model velocity saturation
$\omega_{n,zref}$	0.1	-	Reference model natural frequency
ζ_{zref}	1	-	Reference model damping coefficient
z^n controller			
$K_{p,z}$	1	-	z proportional gain
$K_{d,z}$	0	-	z derivative gain
z_κ	0	-	z κ relating $K_{i,z} = \kappa K_{p,z}$
DP PD controller			
$\omega_{b,\theta}$	2	-	θ controller bandwidth
ζ_θ	0.1	-	θ controller damping coefficient
Moving-mass controller			
$\omega_{b,pm}$	0.5	-	Moving-mass controller bandwidth
ζ_{pm}	2	-	Moving-mass controller damping coefficient
Surge velocity controller			
ω_u	0.3	-	Surge velocity controller bandwidth
u_{ref}	1	$\frac{m}{s}$	Surge reference velocity

Table 4.3: Proposed vehicle configuration for simulation (3)

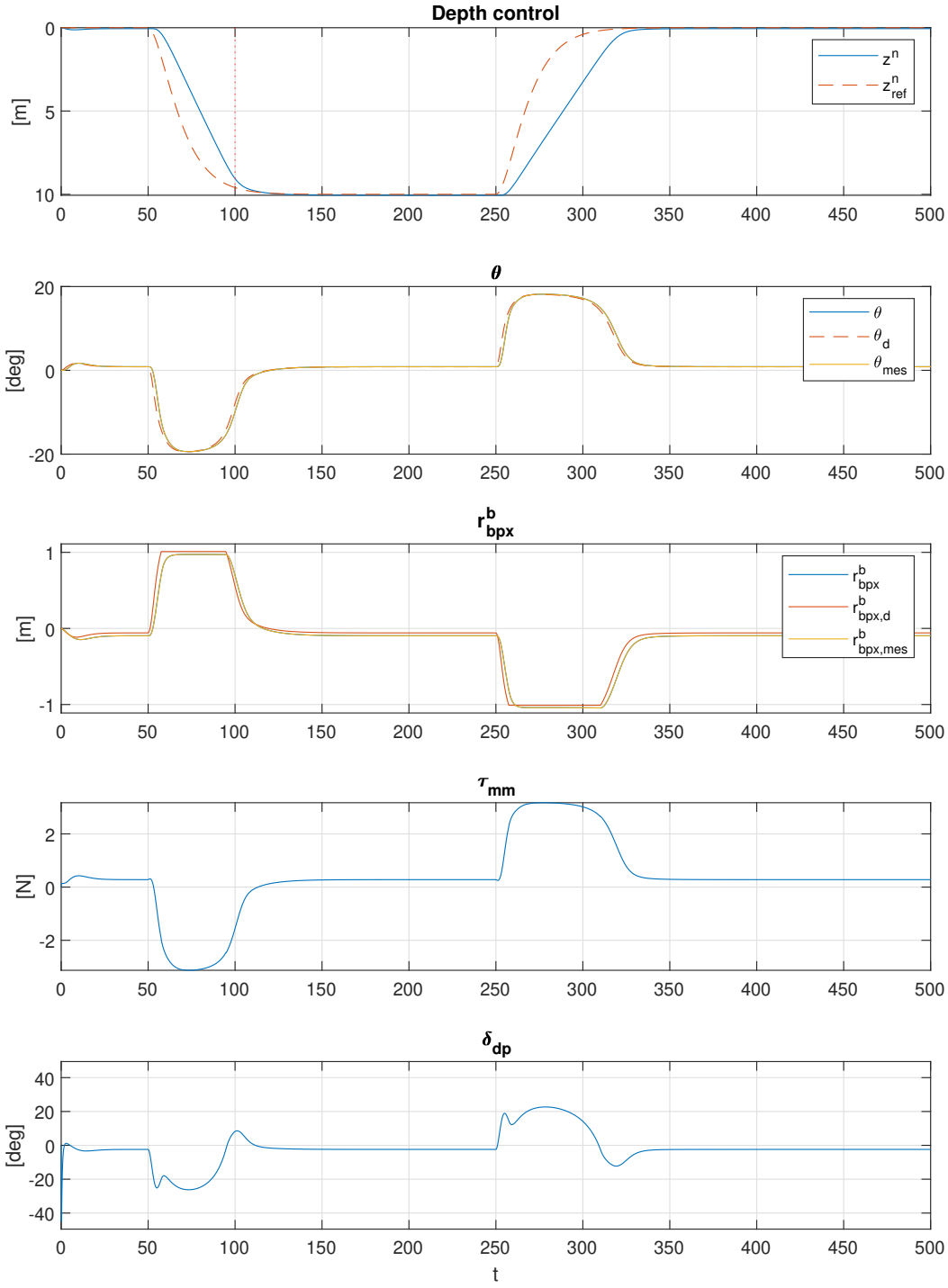

Figure 4.1: Simulated result from saturated P controller, as discussed in section 4.1

4.2 Examining Different Depth Control Laws

Using the configuration presented in Table 4, the control laws determining θ_d can be examined:

4.2.1 Basic Proportional Control law

The basic proportional control law is provided by:

$$\theta_d = -K_{p,z} e_z \tag{4.4}$$

Which then is saturated such that $\theta_d \in (-\frac{1}{2}\pi, \frac{1}{2}\pi)$. Simulating the system using this control law results in the motion shown in figure 4.2. The result shows that the system generally manages to follow the pitch reference until the maximum pitch is reached, but provides oscillations in z. These can be mitigated by tuning the $K_{p,z}$ gain, for example to $K_{p,z} = 0.1$, which results in the tuned result shown in figure 4.3.

Derivative gain in z

Implementing derivative gain such that:

$$\theta_d = -K_{p,z} e_z - K_{d,z} \dot{z} \tag{4.5}$$

Would reduce oscillations in the depth response, measuring the NED velocity $\dot{z}$ is impractical in real-life application. As such, it is not implemented in this thesis. When later discussing feedback control for dive-planes in pitch, derivative gain is implemented as the body angular velocities can easily be obtained by IMUs.

4.2.2 Linear and Quadratic Approximation

For the linear and quadratic approximations described in section 3.5, the control law can be implemented with:

$$\tau_{z,d} = -K_{p,z} e_z \tag{4.6}$$

Simulating this approach yields the result presented in figure 4.4. As shown in the graph, the dive-plane actuation δ_{dp} is lacking as the θ_d never reaches the maximum equilibrium angle possible. Since θ_d is proportional to the error $K_{p,z} e_z$, the gain $K_{p,z}$ can be increased to improve this. Simulating with $K_{p,z} = 3$ yields the result presented in figure 4.5. With the increased proportional gain, the vehicle reaches the saturation limit of both the MMA and the dive-planes during decent, but not during decent. This occurs since the vehicle is not neutrally buoyant, as such its maximum descent rate is larger than the maximum accent rate. And since the reference z model is limited with equal velocity in both positive and negative direction, the error e_z is smaller during descent than accent resulting in smaller actuation as well. The difference between using linear and quadratic approximation is minor, as demonstrated by figure 4.6. There, we see that the difference mainly shows for large e_z, where θ_d falls outside the actuator saturation.

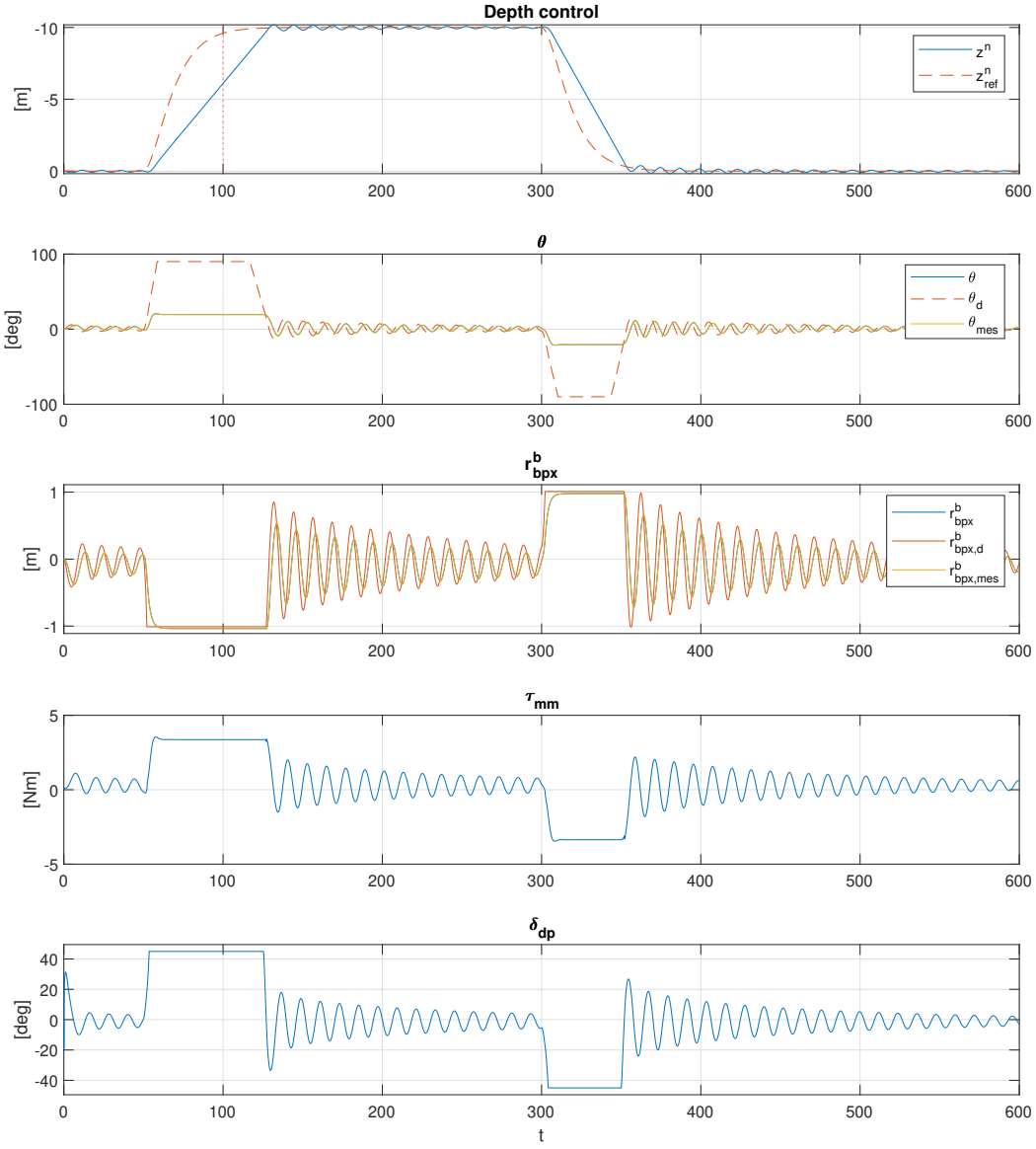

Figure 4.2: Resulting motion using basic P controller

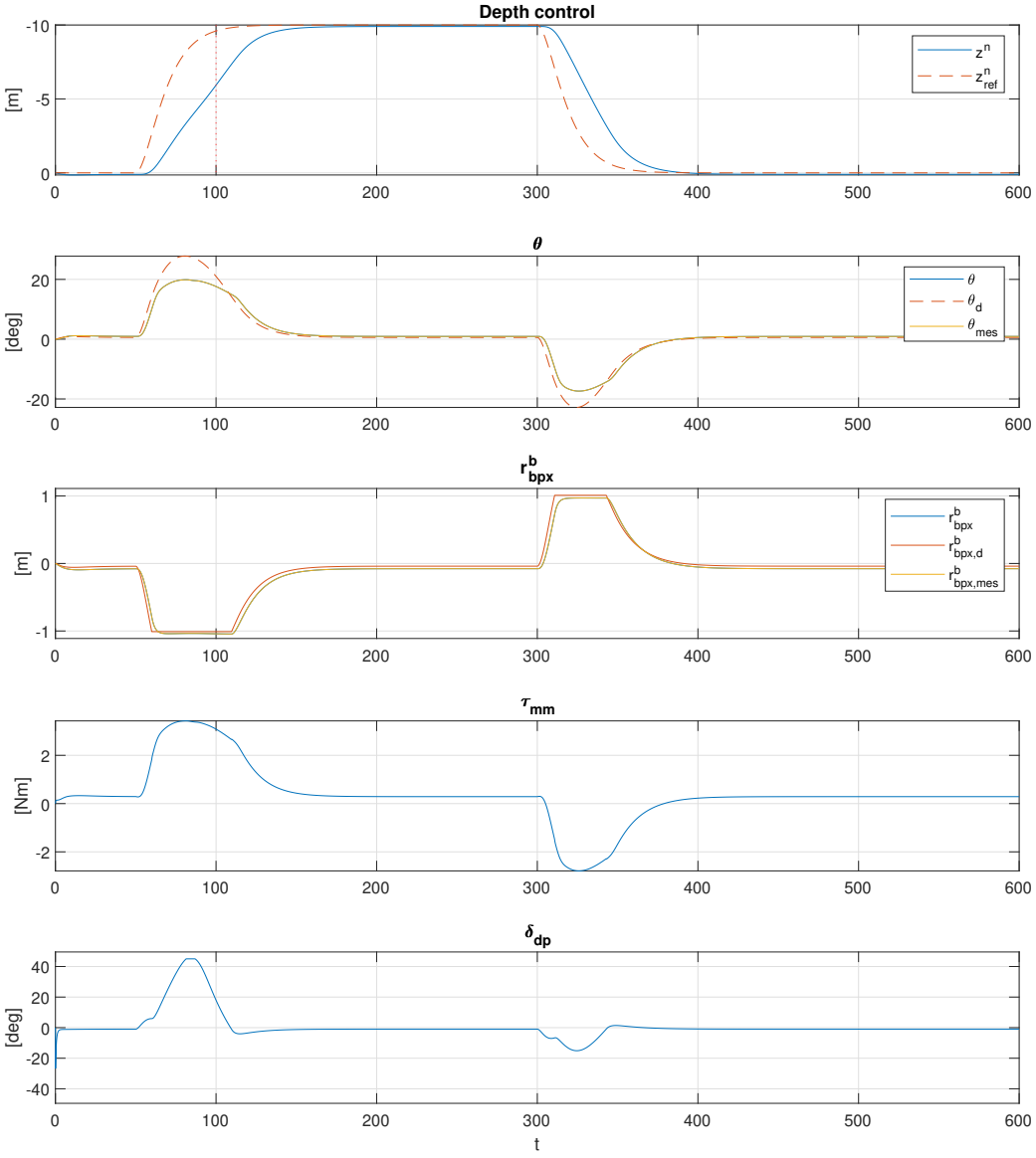

Figure 4.3: Resulting motion using tuned basic P controller

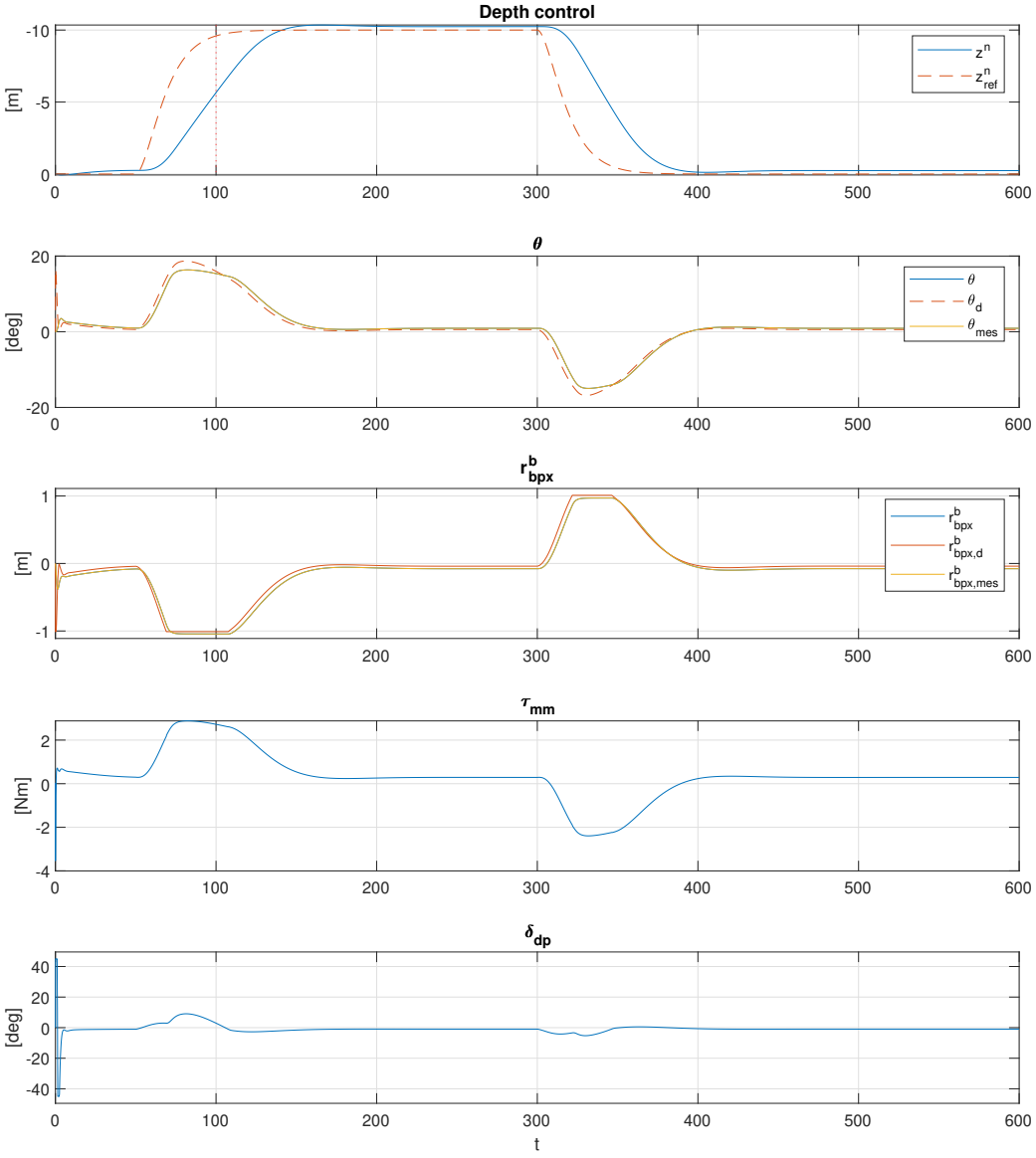

Figure 4.4: Linear approximation for θ_d control law

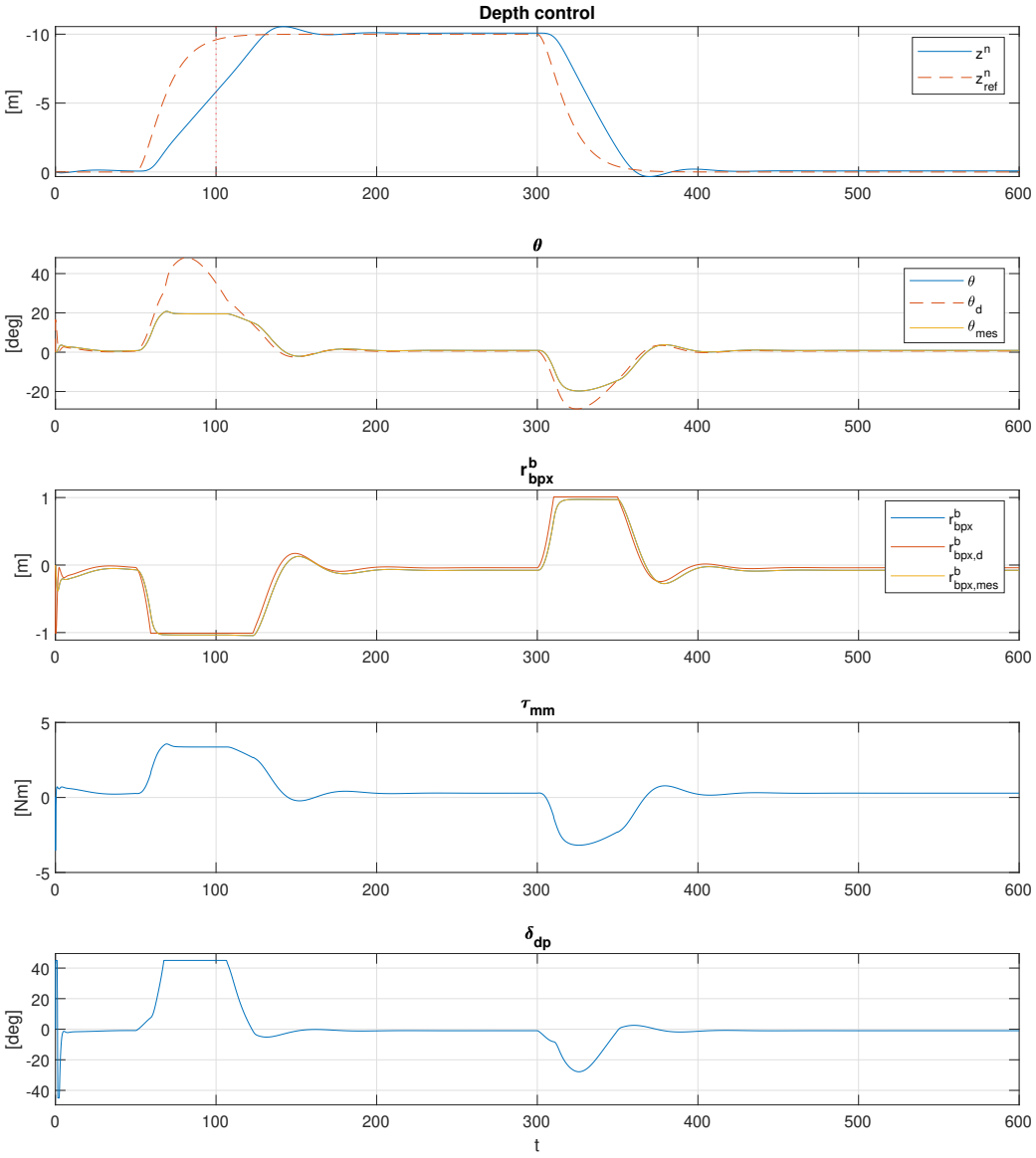

Figure 4.5: Linear approximation with $K_{p,z} = 3$

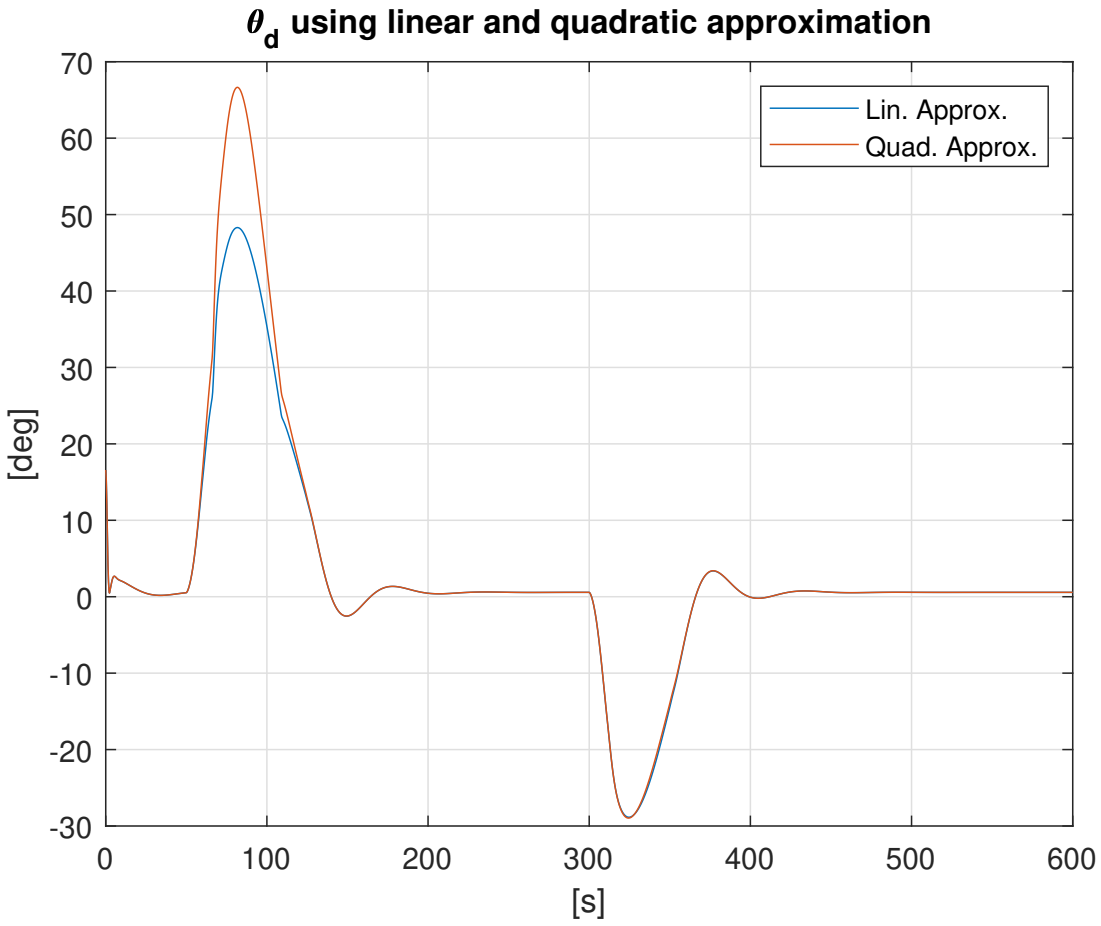

Figure 4.6: Linear versus Quadratic approximation of θ_d control law

4.2.3 Non-Linearly Saturated Proportional Controller

Considering that the basic control law (eq. 4.4) must be saturated to $\theta_d \in (-\frac{1}{2}\pi, \frac{1}{2}\pi)$, nonlinear saturation can be used to ensure a smooth reference using:

$$\theta_d = \text{atan}(-K_{p,z} e_z) = -\text{atan}(K_{p,z} e_z) \tag{4.7}$$

Which would ensure that θ_d is held within the saturation limits. Simulating the system with this control law with $K_{p,z} = 0.2$ yields the result shown in figure 4.7. As shown there, the saturation has little effect on the result, which can be explained by the lack of actual saturation, considering that the resulting θ_d is well below the saturation limit. However, examining the equation in the context of the vehicle dynamics provides an interesting property of this control law: It is similar to the Line-Of-Sight guidance presented in Fossen[33].

4.2.4 Line-Of-Sight (LOS) Control Law

Examining the vehicle z^n dynamics in Amplitude-Phase form (eq.3.36 and 3.50):

$$M_z \ddot{z}^n + D_z \dot{z}^n = \tau_z = A_z \sin(\theta_d - \phi_z) + \tau_g \tag{4.8}$$

$$\tag{4.9}$$

We observe that τ_z in Amplitude-Phase form is on a similar form as the side-track error dynamics for the Proportional LOS guidance law presented in Fossen[33, s12.4], as used there for path-following using course or heading autopilots. Namely:

$$\dot{y}_e^p = U \sin(\chi - \pi_p) \tag{4.10}$$

$$\chi_d = \pi_p - \tan^{-1}(K_p y_e^p) \tag{4.11}$$

As such, a similar control law as the LOS guidance law can be proposed:

$$\tau_z = A_z \sin(\theta - \phi_z) + \tau_g \tag{4.12}$$

$$\theta_d = \tan^{-1}(-K_{p,z} e_z) + \phi_z \tag{4.13}$$

$$\tau_z = A_z \sin(\tan^{-1}(-K_{p,z} e_z)) + \tau_g \tag{4.14}$$

$$= -A_z K_{p,z} \frac{1}{\sqrt{1 + (K_{p,z} e_z)^2}} e_z + \tau_g \tag{4.15}$$

The new dynamics are then provided by:

$$M_z \ddot{z}^n + D_z \dot{z}^n = -A_z K_{p,z} \frac{1}{\sqrt{1 + (K_{p,z} e_z)^2}} e_z + \tau_g \tag{4.16}$$

$$M_z \ddot{z}^n + D_z \dot{z}^n + A_z K_{p,z} \frac{1}{\sqrt{1 + (K_{p,z} e_z)^2}} e_z = \tau_g \tag{4.17}$$

Here we see that the control force τ_z resulting from the control law acts as a spring force with an equilibrium at $z = z_d$. For small e_z, the control force can be approximated as:

$$M_z \ddot{z}^n + D_z \dot{z}^n + A_z K_{p,z} e_z = \tau_g \tag{4.18}$$

Simulating with the control law from equation 4.13 provides the result shown in figure 4.8. As the result shows, the LOS guidance law creates an offset in z. This can be explained by the constant acceleration resulting from the restoring forces τ_g, as this is not handled by the proportional controller. To handle τ_g, integral action can be introduced to the controller.

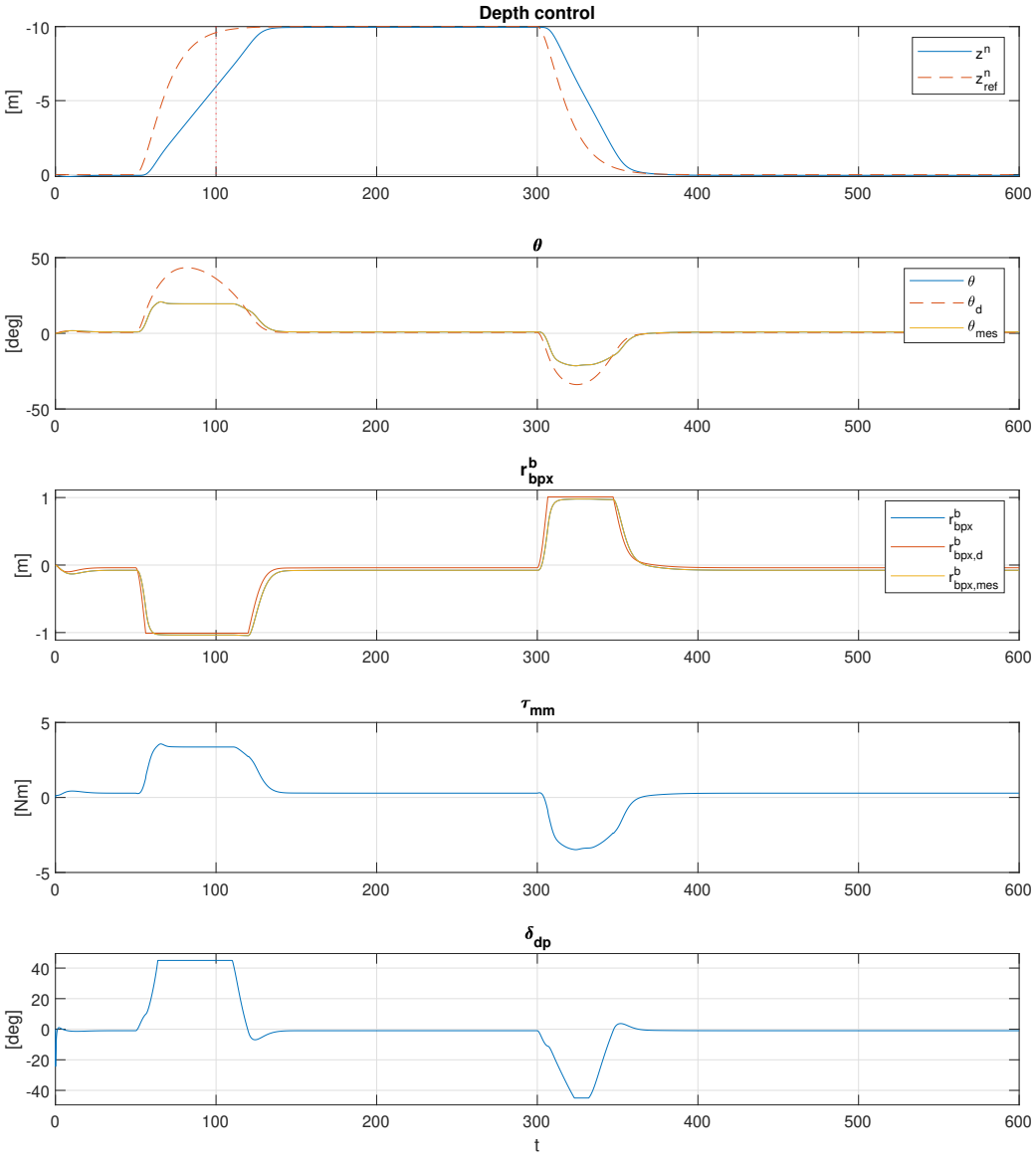

Figure 4.7: Simulated result using $K_{p,z} = 0.2$ and nonlinear saturation

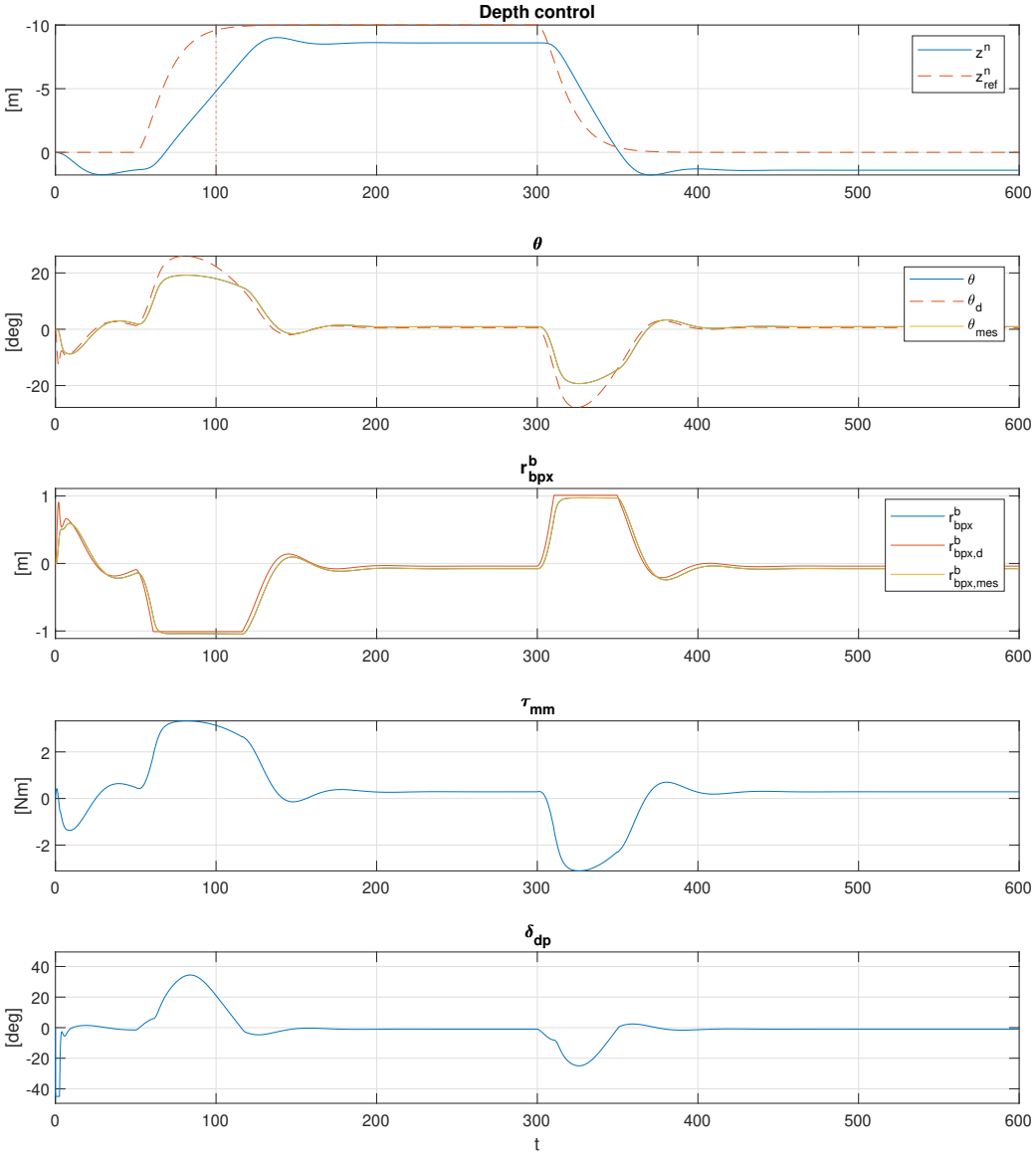

Figure 4.8: LOS guidance law for θ_d

4.2.5 Integral LOS Control Law

In Fossen[33, Ch12], two formulas for implementing integral action with guaranteed stability is presented. Namely, stability for the LOS guidance laws for path following using course or heading autopilots.

Both of these integrators are implemented to remove an unknown disturbance, though in different contexts in Fossen[33]. Considering the z dynamics of the depth control system (eq. 4.8), both of these integrators effectively act to remove disturbances in pitch θ and/or ϕ_z. Assuming the depth control system is able to counteract the restoring forces, the dynamics of can be described as:

$$M_z\ddot{z} + D_z\dot{z} = A_z \sin(\theta_d - \phi_z - \bar{\tau_g}(t)) \tag{4.19}$$

$$\theta_d = -\tan^{-1}(K_{p,z}e_z + K_{i,z}z_{int}) + \phi_z \tag{4.20}$$

Then, the integrator z_{int} can compensate for the restoring forces. Implementing the integrator as[33, s12.5]:

$$\kappa = 0.002 \tag{4.21}$$

$$K_{i,z} = \kappa K_{p,z} \tag{4.22}$$

$$\Delta = \frac{1}{K_{p,z}} \tag{4.23}$$

$$\dot{z}_{int} = \frac{\Delta}{\Delta^2 + (e_z + \kappa z_{int})^2} e_z \tag{4.24}$$

Simulating with this control law yields the result shown in figure 4.9. Comparing this result with the LOS guidance without integral effect (fig 4.8), the offset in z^n has successfully been removed by the integral term. However, during rising and diving- maneuvers, integrator windup occurs as the actuator saturation limits prevent the vehicle from following the reference trajectory as intended. And the greater the maneuver change, the greater this will affect the controller performance. This could be countered by slowing down the reference trajectory, namely decreasing the velocity saturation to better suit the actual maximum descent rate. However, this requires more tuning of the saturation limit, and on a practical implementation the saturation would likely have to be set lower than the maximum expected saturation to be certain windup is avoided.

Alternatively, the purpose of the integrator can be questioned: If we instead of aiming to reduce the general error e_z, consider just removing the stationary error that occurs when the vehicle is stabilizing on the desired z_d^n. This can be considered to occur when the reference model provides a velocity reference of $z_{ref}^n \approx 0$. As such, the following integrator limiter is proposed:

$$\dot{z}_{int} = \begin{cases} 0 & \dot{z}_{ref}^n > \dot{z}_{ref,tol}^n \\ \frac{\Delta}{\Delta^2 + (e_z + \kappa z_{int})^2} e_z & else \end{cases} \tag{4.25}$$

Simulating the system with this limiter using $\dot{z}_{ref,tol}^n = 1 \cdot 10^{-7}$ yields the results provided in figure 4.10. As we see, the overshoot in z is now much smaller, while the integrator still removes the stationary deviation due to τ_g.

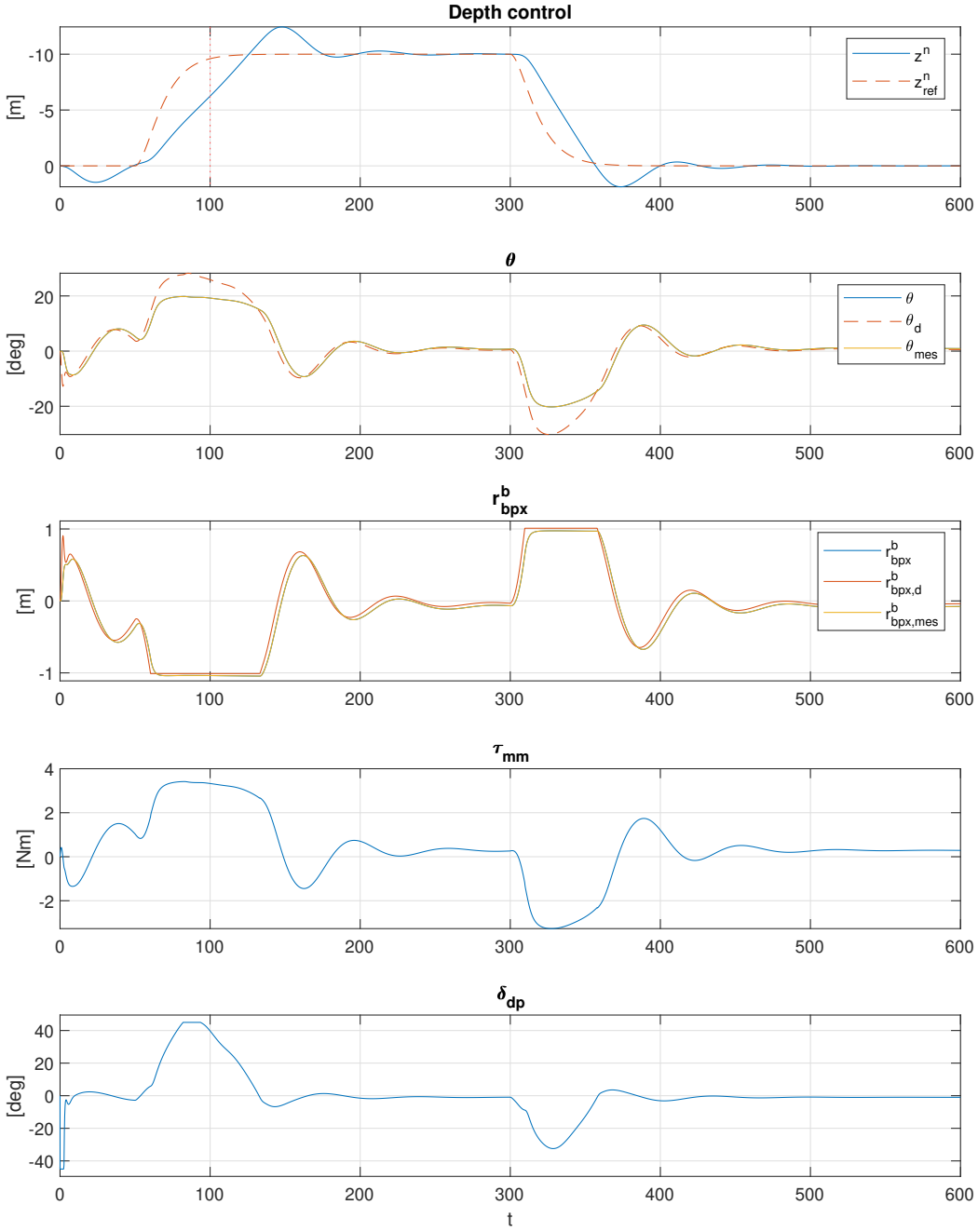

Figure 4.9: ILOS guidance law for θ_d

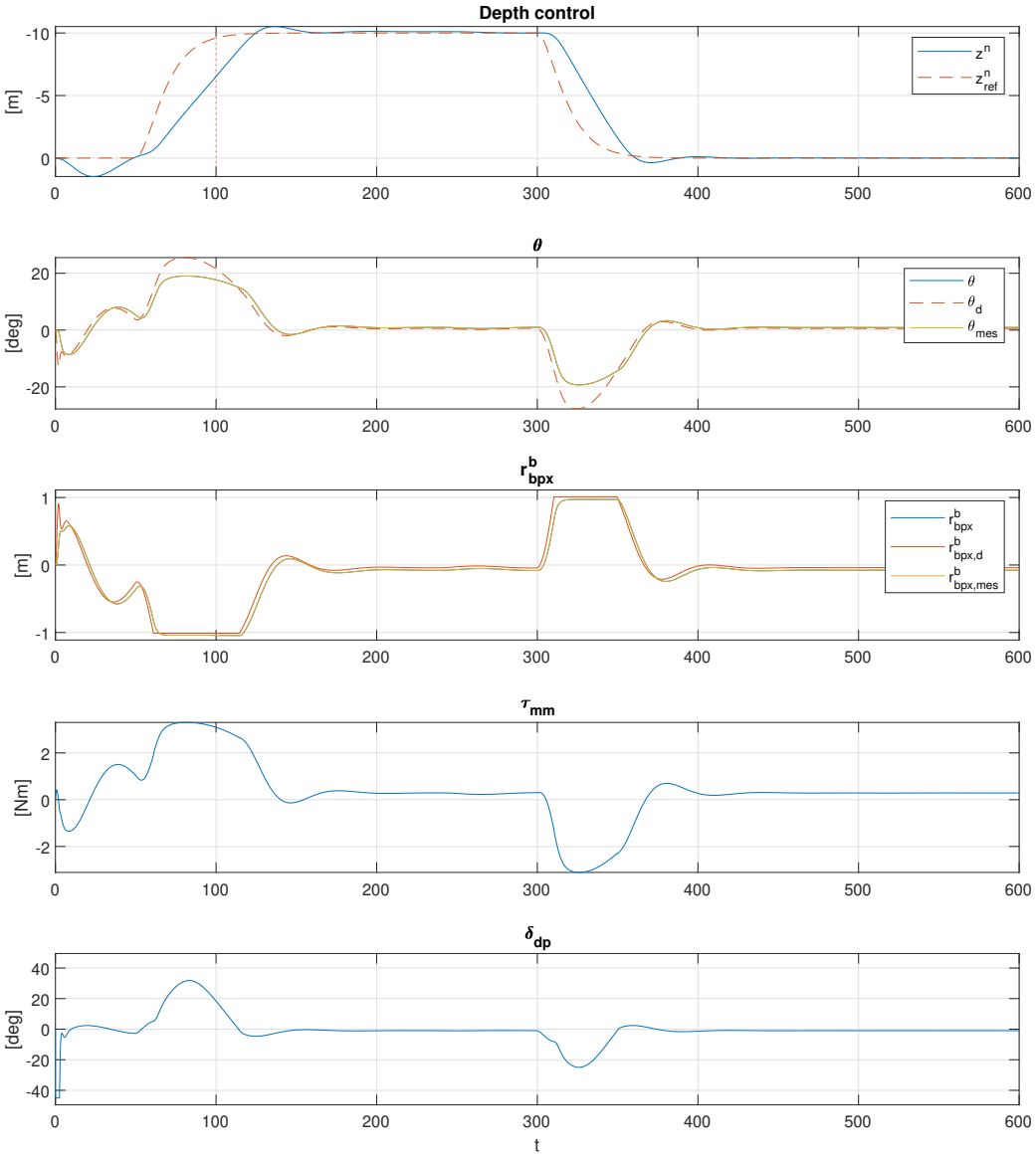

Figure 4.10: ILOS guidance law for θ_d, with integration limit based on $\dot{z}^n_{ref}$

4.2.6 Integrator Preloading

Examining the result of the ILOS implementation, it can be seen that early in the simulation, the deviation increases until the integrator has gotten time to build up. The time this takes can be reduced by increasing κ and thus in turn $K_{i,z}$, however, this will lead to more oscillations in the system. And considering that a damping term $K_{d,z}$ is impractical to introduce (measuring NED velocity), this is harder to reduce by other means. However, instead of starting the system with $z_{int} = 0$, the integrator can be pre-loaded with some desired value $z_{int,0}$, based on τ_g. Examining the vehicle z-dynamics resulting from the ILOS control law:

$$\theta_d = \phi_z - \tan^{-1}(K_{p,z}e_z + K_{i,z}z_{int}) \tag{4.26}$$

$$M_z\ddot{z}^n + D_z\dot{z}^n = A_z \sin(\theta_d - \phi_z) + \tau_g \tag{4.27}$$

$$= -A_z \sin(\tan^{-1}(K_{p,z}(e_z + \kappa z_{int}))) + \tau_g \tag{4.28}$$

$$= -A_z \frac{K_{p,z}(e_z + \kappa z_{int})}{\sqrt{1 + K_{p,z}^2(e_z + \kappa z_{int})^2}} + \tau_g \tag{4.29}$$

$$\approx -A_z K_{p,z} e_z - A_z K_{p,z} \kappa z_{int} + \tau_g \tag{4.30}$$

Now, consider the term $-A_z K_{p,z} \kappa z_{int}$ to fully counter the restoring force τ_g:

$$-A_z K_{p,z} \kappa z_{int} \approx \tau_g \tag{4.31}$$

$$\rightarrow z_{int,0} := -\frac{\tau_g}{A_z K_{p,z} \kappa} \tag{4.32}$$

Thus, the integrator can be pre-loaded with this value. Simulating the system with a pre-loaded z_{int} using:

$$\tau_g = g(m_v + m_p - V_v \rho_w) \tag{4.33}$$

$$A_z \approx F_{thrust} \tag{4.34}$$

Yields the result presented in figure 4.12, which shows that the dip in depth during the beginning of the simulation now is greatly reduced. Plotting z_{int} for both methods also reveals the difference, as shown in figure 4.11. As the graph shows, the initial condition for z_{int} was not perfect, but still a great improvement from zero-start conditions.

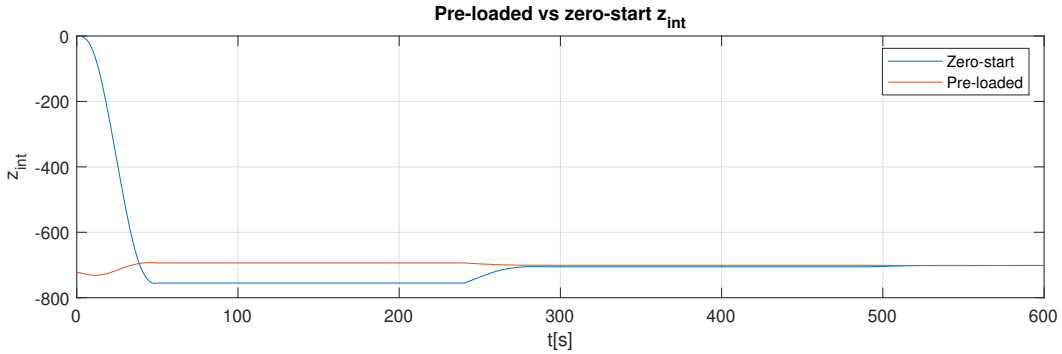

Figure 4.11: z_{int} over time using and not using pre-loading

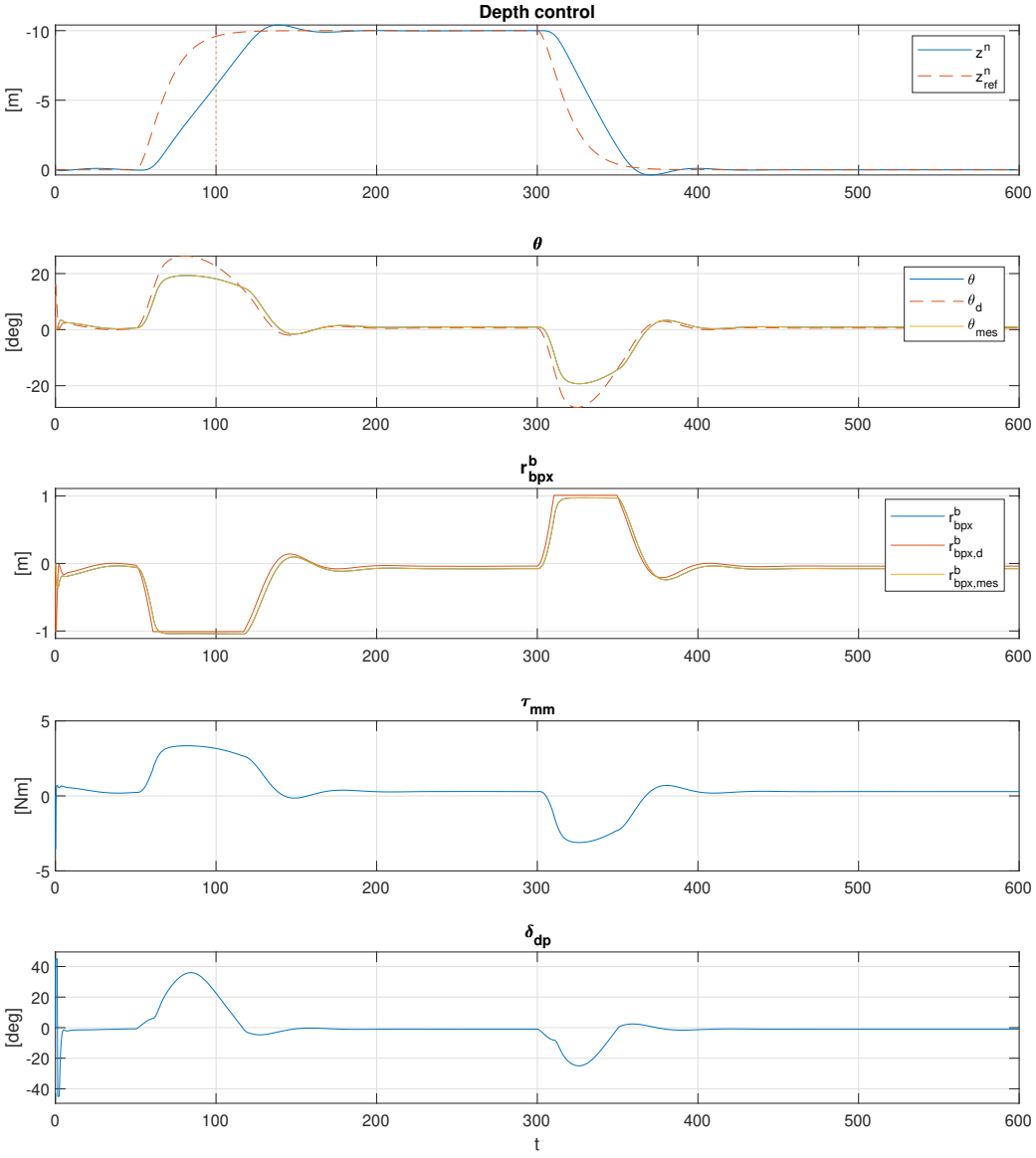

Figure 4.12: ILOS guidance law for θ_d using pre-loaded integrator

4.2.7 Integrator Based On Course Autopilot LOS Guidance Law

So far the control law is based on Heading autopilot LOS guidance (eq. 4.24). However, Fossen[33, s12.4] also contains an integrator based on Course autopilot LOS guidance:

$$\dot{y}^p_{int} = U \sin(\chi - \pi_p) \tag{4.35}$$

$$= \frac{U y^p_e}{\sqrt{\Delta^2 + (y^p_e + \kappa y^p_{int})^2}} \tag{4.36}$$

Which results in the cross-track error dynamics:

$$\dot{y}^p_e = -U \frac{y^p_e + \kappa y^p_{int}}{\sqrt{\Delta^2 + (y^p_e + \kappa y^p_{int})^2}} \tag{4.37}$$

Comparing these dynamics with the integrator dynamics presented in equation 4.27 and 4.29, a similar integrator can be determined for the depth control system:

$$\dot{z}_{int} = \frac{A_z}{\sqrt{\Delta^2 + (e_z + \kappa z_{int})^2}} e_z \tag{4.38}$$

Comparing this integrator with the Heading-based integrator (eq. 4.24), we note some differences. Firstly, the numerator has changed from Δ to A_z. If the actual value for A_z is used, then the dynamics of this integrator becomes time-varying, as A_z varies with time. This could be mitigated by using a constant A^*_z, similarly as when determining the integrator preload in section 4.2.6 if desired. Additionally, a more significant change is that the denominator is now a square root function. As such, the integrating rate $\dot{z}_{int}$ will, for $\Delta \approx A_z$, be larger using this approach, and the integrator is thereby more aggressive. As such, the look-ahead distance Δ would have to be increased if the performance of these integrators is desired to have similar dynamics. However, simulating the system reveal that κ needs to be reduced further due to windup. Simulating the system with $\Delta = 10$ and $\kappa = 1 \cdot 10^{-4}$ yields the result shown in figure 4.13.

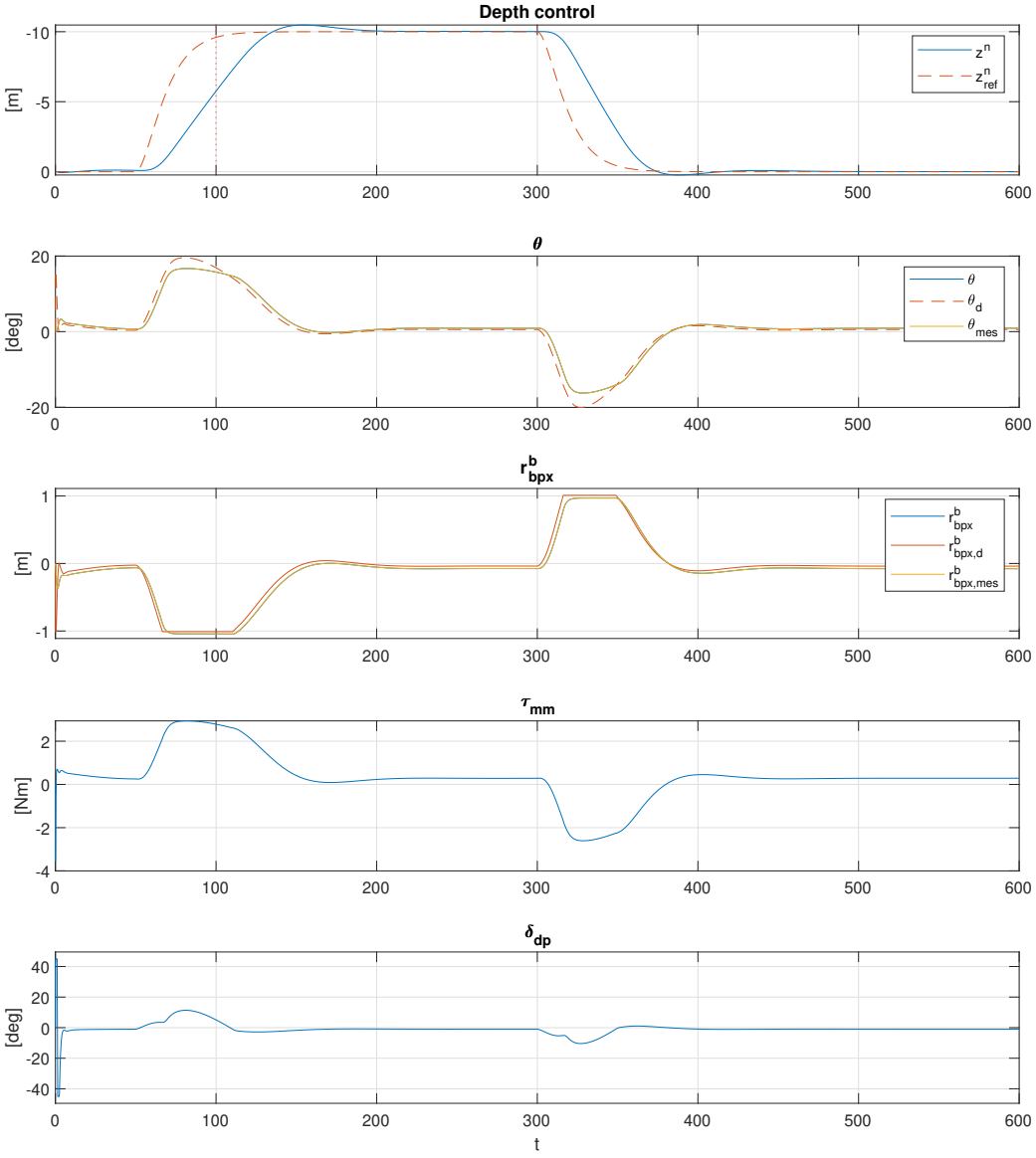

Figure 4.13: Integrator based on Course autopilot LOS guidance

Saturating for θ_{max}

Considering the actuator limitations, the pitch control law θ_d should be saturated such that it does not exceed the limit specified by equation 3.34. The function $\tan^{-1}(x)$ can be used as a nonlinear saturation limiting the input to $(-\frac{1}{2}\pi, \frac{1}{2}\pi)$, however, this function will affect small values of its input x and limit the input long before the saturation limit is reached. Therefore, an alternative saturation function is suggested:

$$\bar{x} = \frac{x}{\left(1 + (\frac{1}{x_{lim}}x)^{2o}\right)^{\frac{1}{2o}}} \tag{4.39}$$

Where x is the unsaturated input, $\bar{x}$ is the saturated output, o is the order of the function and x_{lim} is the desired saturation limit. The order $o > 0, o \in \mathbb{Z}$ indicates how fast the saturation occurs; the higher the order, the longer the input has a linear output. In return, a higher order of o means later, but more aggressive saturation of the input. Increasing the order $o \to \infty$ yields a similar performance as using an if-statement:

$$\bar{x} = \lim_{o\to\infty} \frac{x}{\left(1 + (\frac{1}{x_{lim}}x)^{2o}\right)^{\frac{1}{2o}}} \iff \bar{x} = \begin{cases} -x_{lim} & x < x_{lim} \\ x_{lim} & x > x_{lim} \\ x & else \end{cases} \tag{4.40}$$

The effect of the saturation function using different orders o is compared to using $\frac{2}{\pi}\text{atan}(\frac{\pi}{2}x)$ in figure 4.14.

The function can also be defined based on lower x_{min} and upper x_{max} saturation limits:

$$x_{avg} = \frac{1}{2}(x_{max} + x_{min}) \tag{4.41}$$

$$x_{halfspan} = \frac{1}{2}(x_{max} - x_{min}) \tag{4.42}$$

$$\bar{x} = \frac{x - x_{avg}}{\left(1 + \left(\frac{x - x_{avg}}{x_{halfspan}}\right)^{2o}\right)^{\frac{1}{2o}}} + x_{avg} \tag{4.43}$$

Comparison with z-dynamics

Interestingly, using this function with an order of $o = 1$ provides the same dynamics for x as the z-dynamics when using the LOS guidance law (eq. 4.15):

$$\sin(\tan^{-1}(-K_{p,z}e_z)) = -\frac{K_{p,z}e_z}{\sqrt{1 + (K_{p,z}e_z)^2}} = \frac{x}{\left(1 + (\frac{1}{x_{lim}}x)^2\right)^{\frac{1}{2}}} \tag{4.44}$$

With $x = K_{p,z}e_z$ and $x_{lim} = 1$, suggesting that using the LOS control law has a saturated generalized control force limited by:

$$\frac{K_{p,z}e_z}{\sqrt{1 + (K_{p,z}e_z)^2}} \in (-1, 1) \tag{4.45}$$

$$\to -A_z\frac{K_{p,z}e_z}{\sqrt{1 + (K_{p,z}e_z)^2}} \in (-A_z, A_z) \tag{4.46}$$

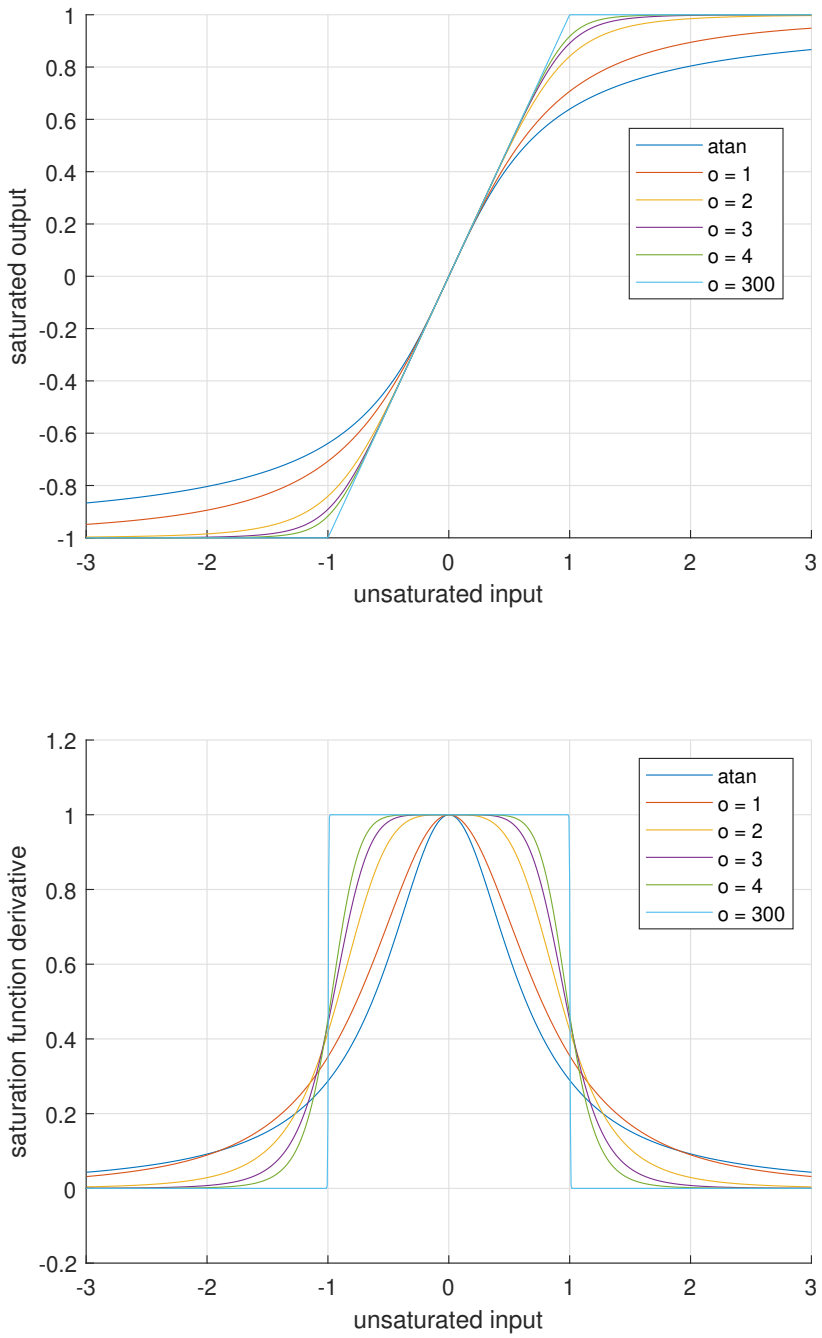

Figure 4.14: Effect of different orders in the saturation function presented in equation 4.39, with $\frac{2}{\pi}\text{atan}(\frac{\pi}{2}x)$ for comparison. Show resulting saturation (top) and function derivative (bottom)

This allows us to discuss the validity of the approximation from equation 4.30, as this only holds for small e_z. Namely, we can see that the value for $K_{p,z}e_z$ has, for $o = 1$, been reduced by roughly 30% for $K_{p,z}e_z$. Examining the function derivative, we can see that the ratio between the unsaturated input and saturated output is only 1 occur approximately at $x_{unsat} = 0$, while increasing the order of the function also increases the width of this linear relation, though as the cost of sharper saturation closer to $K_{p,z}e_z = 1$. If we consider implementing an input of $x_{unsat} \in (-1, 1)$, the following condition can be determined:

$$K_{p,z}e_z \in (-1, 1) \tag{4.47}$$

$$\rightarrow e_z \in (-\frac{1}{K_{p,z}}, \frac{1}{K_{p,z}}) \tag{4.48}$$

$$= (-\Delta, \Delta) \tag{4.49}$$

or, if we instead consider limiting the saturation to some constant c:

$$x_{unsat} = K_{p,z}e_z \in (-c, c) \tag{4.50}$$

$$\rightarrow e_z \in (-c\Delta, c\Delta) \tag{4.51}$$

We note that the look-ahead distance Δ affects the region of which the assumption is valid:

$$e_z \in (-c\Delta, c\Delta) \propto (-\Delta, \Delta) \tag{4.52}$$

This rule can be extended to include the integral effect:

$$K_{p,z}(e_z + \kappa z_{int}) \in (-c, c) \tag{4.53}$$

$$e_z + \kappa z_{int} \in (-c\Delta, c\Delta) \tag{4.54}$$

$$\kappa z_{int} \in (-c\Delta - e_z, c\Delta - e_z) \tag{4.55}$$

$$z_{int} \in \left(-\frac{1}{\kappa}(e_z + c\Delta), -\frac{1}{\kappa}(e_z - c\Delta)\right) \tag{4.56}$$

Which provides an alternative condition for the integrator limiter presented earlier (eq. 4.25), which reflects the actual dynamics of the vehicle rather than being purely based on the reference model.

Additionally, to prevent the integrator term from being "stuck", the term z_{int} can be set to decay by reducing it by some factor of itself each iteration towards the pre-loaded value $z_{int,0}$. The decaying function can be determined by:

$$z_{int}(i+1) = (1 - \delta_{int}dt)(z_{int}(i) - z_{int,0}) + z_{int,0} \tag{4.57}$$

Where $\delta_{int}dt \in (0, 1)$ decides the decay rate at which z_{int} converges to $z_{int,0}$. Note that since this update is discrete, the integrator can be destabilized in simulation for large dt. This can be transformed from discrete to continuous time:

$$z_{int}(i+1) = (1 - \delta_{int}dt)(z_{int}(i) - z_{int,0}) + z_{int,0} \tag{4.58}$$

$$z_{int}(i+1) - z_{int}(i)(1 - \delta_{int}dt) = z_{int,0}\delta_{int}dt \tag{4.59}$$

$$z_{int}(i+1) - z_{int}(i) = (z_{int,0} - z_{int}(i))\delta_{int}dt \tag{4.60}$$

$$\dot{z}_{int} \approx \frac{z_{int}(i+1) - z_{int}(i)}{dt} = (z_{int,0} - z_{int})\delta_{int} \tag{4.61}$$

$$\tag{4.62}$$

Which holds for small dt. Notably, if the time-step dt is limited to $dt \leq 1$, then the decay rate δ_{int} can be safely set within $\delta_{int} \in (0, 1)$. Combined, the integrator limiter dynamics can be described as:

$$\dot{z}_{int} \begin{cases} \frac{\Delta e_z}{\Delta^2 + (e_z + \kappa z_{int}(i))^2} & z_{int} \in [-\frac{1}{\kappa}(e_z + c\Delta), -\frac{1}{\kappa}(e_z - c\Delta)] \\ (z_{int,0} - z_{int})\delta & else \end{cases} \tag{4.63}$$

Simulating the system with this integrator limiter provides the result shown in figure 4.15. An even stricter integrator limiter can be implemented by saturating the integrator z_{int} such that it is always within its limits (eq. 4.56). However, such a saturation will severely affect the system performance whenever significant e_z occur. Since the integrator limiter is implemented to reduce integrator windup due to saturation, using the limiter described by equation 4.63 is preferred in this thesis.

4.2.8 Non-Linearly Saturated Proportional-Integral Controller

Using the control law based on LOS guidance has a couple of drawbacks. Firstly, the LOS guidance control laws proposed in this thesis are dependent on the forces acting on the vehicle affecting the Amplitude-Phase variables A_z and ϕ_z. Namely, the variables are dependent on the forces F_{thrust}, F_{drag}, and F_{lift}. While F_{thrust} normally is specified by the thruster specifications, F_{drag} and F_{lift} are dependent on a range of time-varying variables, such as projected areas and coefficients. As such, implementing a simpler control scheme can reduce dependencies on vehicle modeling. Secondly, while the ILOS control law (eq.3.52) is limited to $\theta_d \in (-\frac{1}{2}\pi, \frac{1}{2}\pi)$, the actual maximum pitch providable by the actuators (as provided by eq. 3.26) is generally lower than this. Thus, the desired pitch θ_d should be saturated to reflect this actuator limitation. If the phase compensation is removed, the non-linearly saturated P controller (eq 4.7) can be modified to include integral action and saturation limit:

$$\theta_d = -\theta_{max} \frac{2}{\pi} \tan^{-1}(K_{p,z} e_z + K_{i,z} z_{int}) \tag{4.64}$$

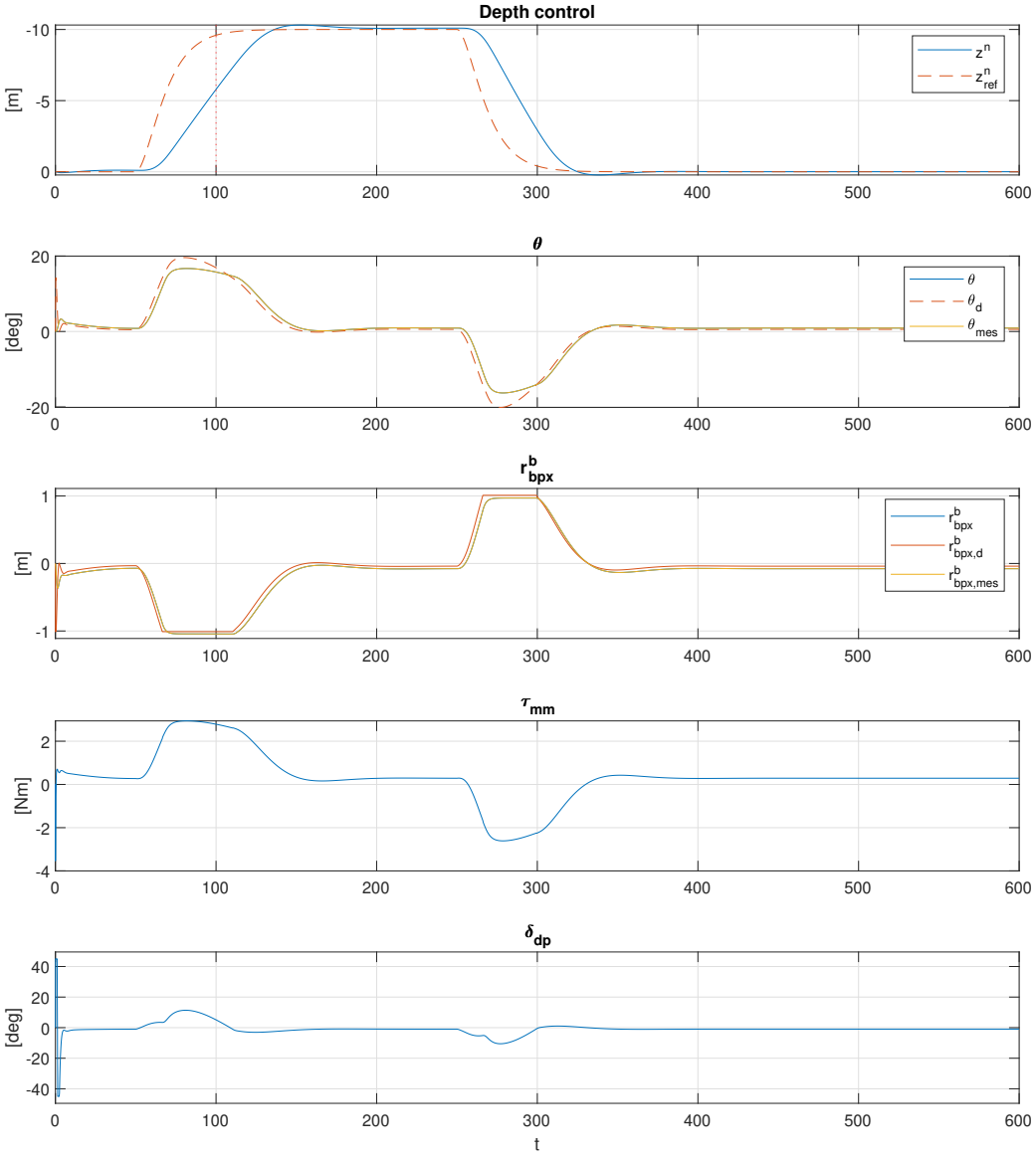

Figure 4.15: Simulated result using the integrator limiter presented in equation 4.63

Chapter 5

Simulating the System for Different Actuator Combinations and Settings

Now that potential control laws has been discussed, the performance of the MMA and dive-planes can be compared in different settings.

5.1 Validating Actuation Methods

Firstly, the system is simulated considering the cases:

- Using only dive-plane (DP) actuation
- Using only MMA
- Using the combined actuation of both actuators

And the result, as shown in Figure 5.1, reveal that for the configuration presented in Table 4, all three cases manages to follow the depth reference, and the MMA case even descends and ascend quicker than the DP only case. However, it should be noted that this configuration is only one of several configurations, and only shows that the suggested configurations are feasible for depth control without discussing the feasibility of the configurations themselves. For example, the MMA is set to be actuatable for the entire length of the vehicle, while spatial constraints might not allow this, as discussed in the literature review. Additionally, the simulation shows result with a surge velocity of $u = 1\frac{m}{s}$ without current present.

5.2 Surge velocity

Since the dive-planes are proportional to the squared relative velocity U_r^2, their effectiveness is negligible at small U_r, providing MMA an advantage over the use of dive-planes, as discussed in chapter 1. As such, the effectiveness of the configuration is examined for different surge velocities to examine how it affects performance. However, increasing the surge velocity increasingly induces oscillation in the pitch channel until the channel destabilizes the system. For example, simulating a holding maneuver for $z_{ref}^n = 0$ with $u_{ref} = 10$ shows (Fig. 5.2) that the motion destabilizes starting with an exponentially growing $\omega_y^b (= \omega_\theta)$ until $t \approx 75[s]$, at which the oscillations in the pitch channel fully destabilize the system. This could a result of the control laws, however, simulating at large velocities is out of scope for this thesis. As such, the performance is examined using $u_{ref} \in [0, 8]$, The result of simulating the system for different u_{ref} within these values is shown in Figure 5.3 and 5.4. As we can see, both methods are unstable for larger u_{ref}. As the surge velocity u increases,

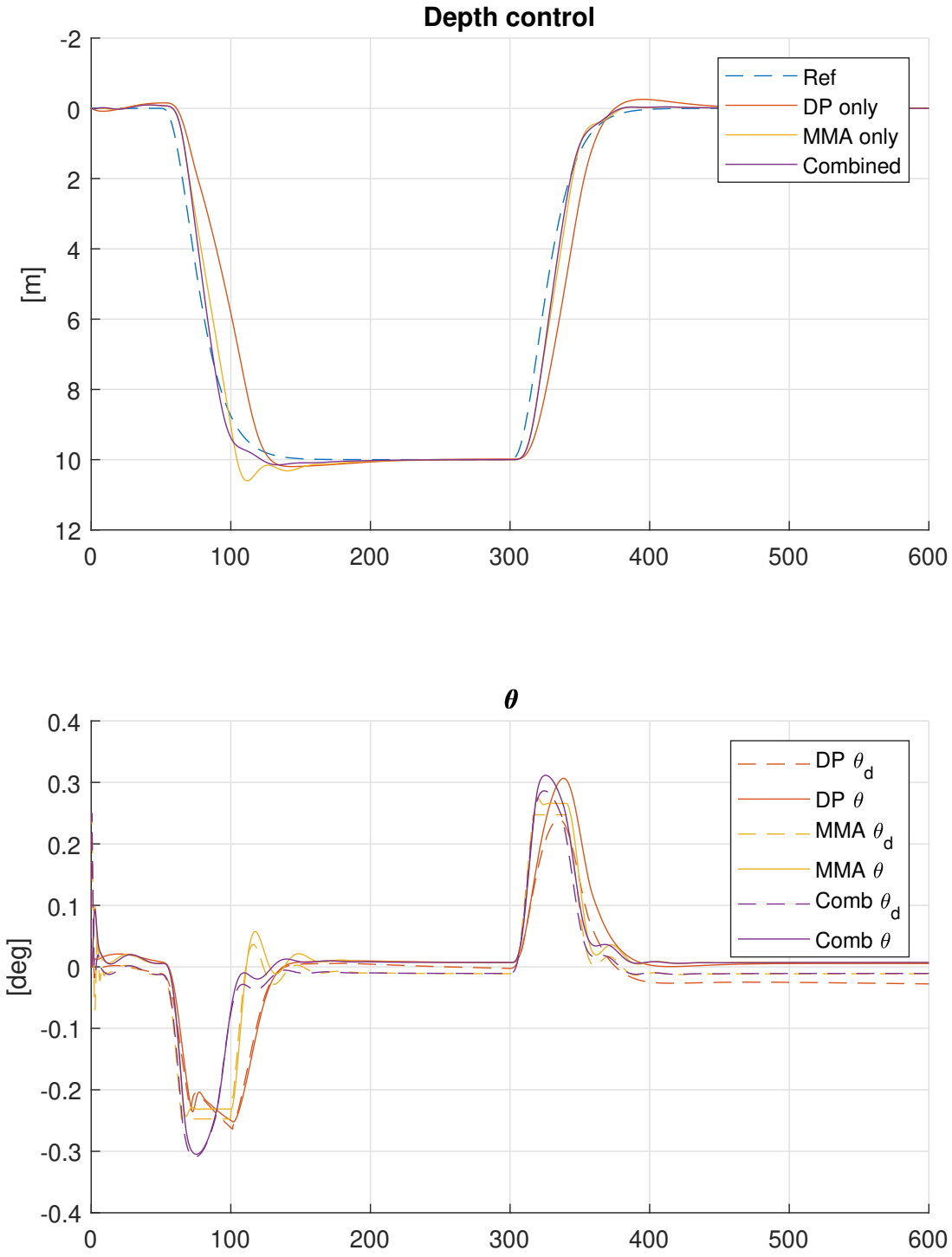

Figure 5.1: Simulated result using only dive-planes (red), only MMA (yellow) and combined actuation (magneta).

the Coriolis and centripetal term for the attitude dynamics $S(\boldsymbol{\nu_1})\boldsymbol{\mathcal{P}}$ grows as well. These tend to be handled by the damping, however, since the vehicle is modeled using linear damping, this may not be the case for larger body velocities.

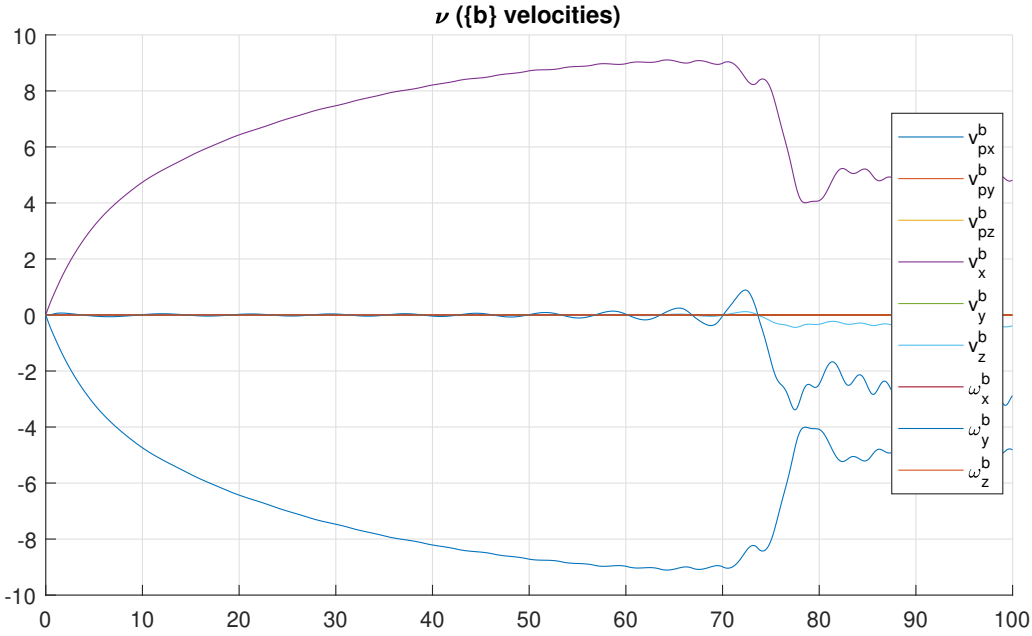

Figure 5.2: Body velocities example for $u_{ref} = 10$ using dive-planes only

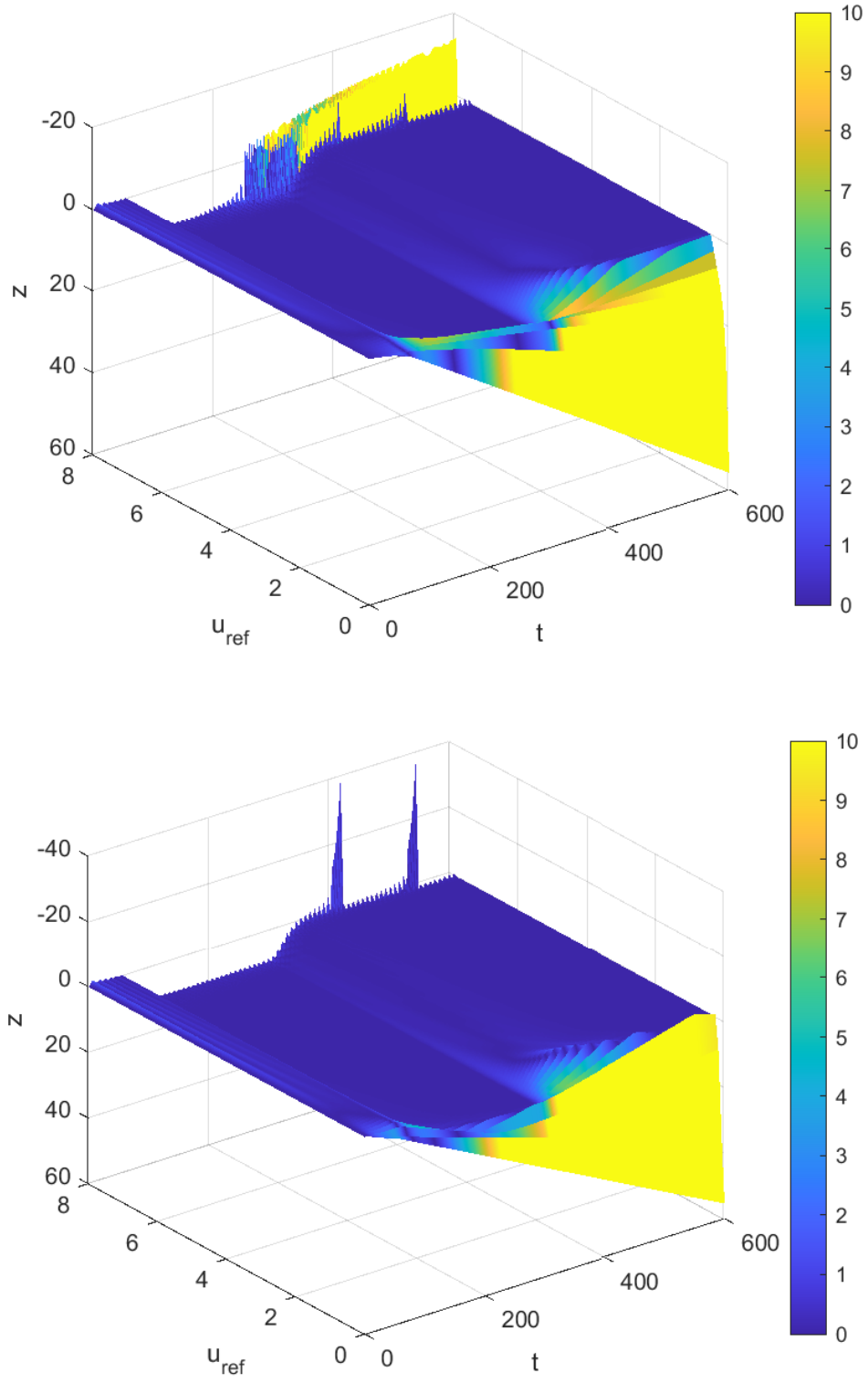

Figure 5.3: Simulated depth control using dive-planes only (top) and combined actuation (bottom) over different surge reference velocities, color by absolute depth error $|e_z|$ saturated to $|e_z| < 10$ for increased contrast

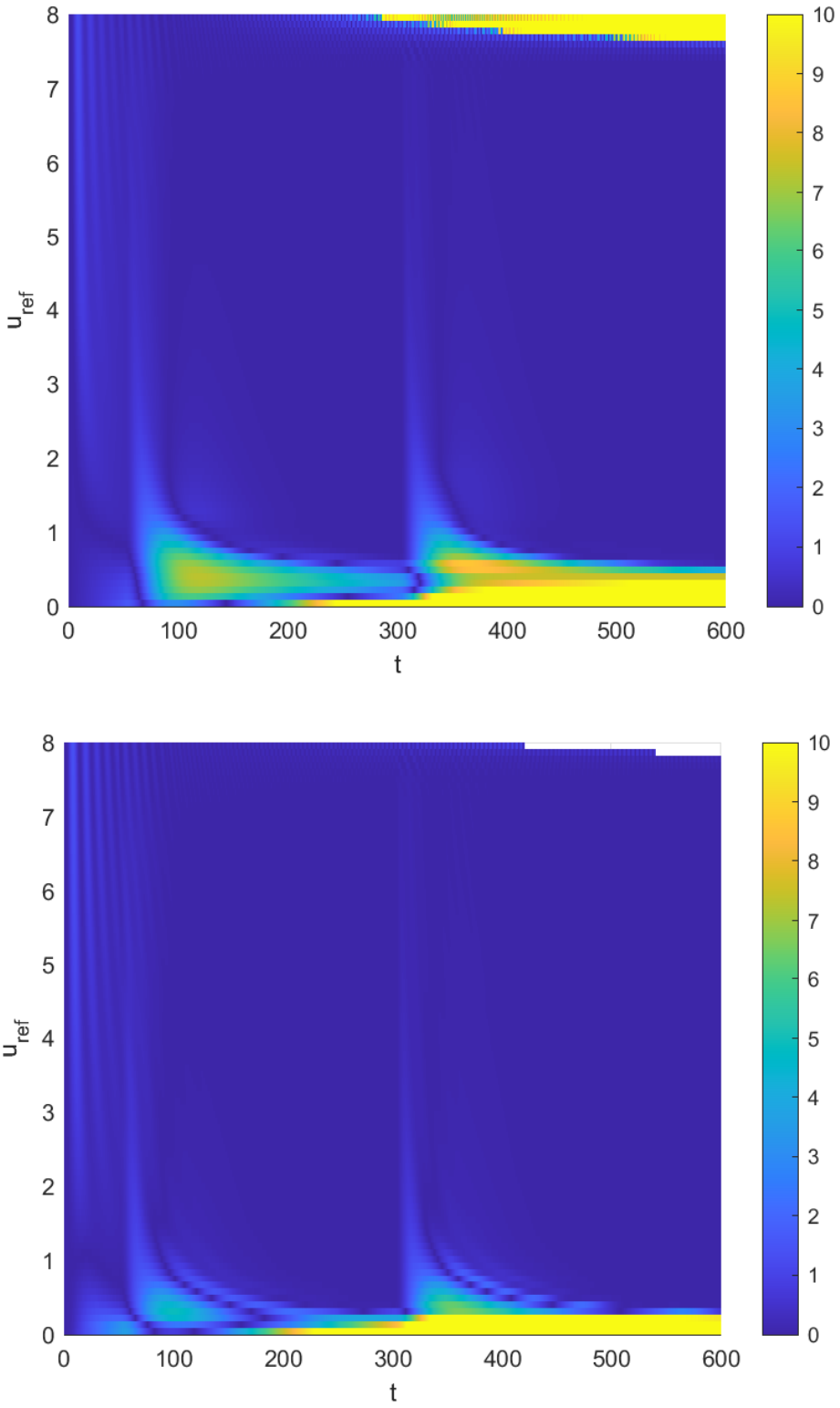

Figure 5.4: Simulated depth control using dive-planes only (top) and combined actuation (bottom) over different surge reference velocities, color by absolute depth error $|e_z|$ saturated to $|e_z| < 0$. Some values at larger u_{ref} is removed as the simulation was unstable and ended early

5.2.1 Attitude Control

The combined actuation does not manage to provide depth control at zero surge velocity $u = 0\frac{m}{s}$. However, the model used in this thesis is not neutrally buoyant. As such, the main thruster must counteract the buoyancy of the vehicle, as partly discussed in section 4.2.5. However, when holding zero surge velocity, the main thruster does not manage to perform this. If instead a neutrally buoyant vehicle is simulated, the depth control system is able to perform diving and rising maneuvers provided it manages to control the vehicle pitch θ. As such, the effect of adding MMA to the system can be further explored by considering the inner pitch controller for different surge velocities. Performing simulations for both dive-plane-only actuation and combined actuation following a sine wave pitch reference yield the result provided in Figures 5.5-5.8. Examining these figures, we see that the combined actuation performs significantly better than the dive-plane-only case at small u_{ref}, even managing to provide significant pitching at zero surge velocity. However, due to saturation of the MMA, the pitch providable by the control system is limited. This limitation comes from the restoring forces due to the offset in CG from CO, namely $r^b_{bg,z}$, which provides a spring force for nonzero pitch angles. The maximum pitch angle providable by the MMA is, as provided by equation 3.14:

$$\theta_{max} = \tan^{-1}\left(-\sigma_p \frac{r^b_{bp,x,max}}{r^b_{bg,z}}\right) \tag{5.1}$$

Notably, the maximum pitch is dependent on the mass ratio σ_p, which coincides with the relations found in the literature (section 1.6.3). Additionally, we note that the error (as colored) is, in general, smaller for the combined actuation case than the dive-plane-only case, especially at smaller u_{ref}.

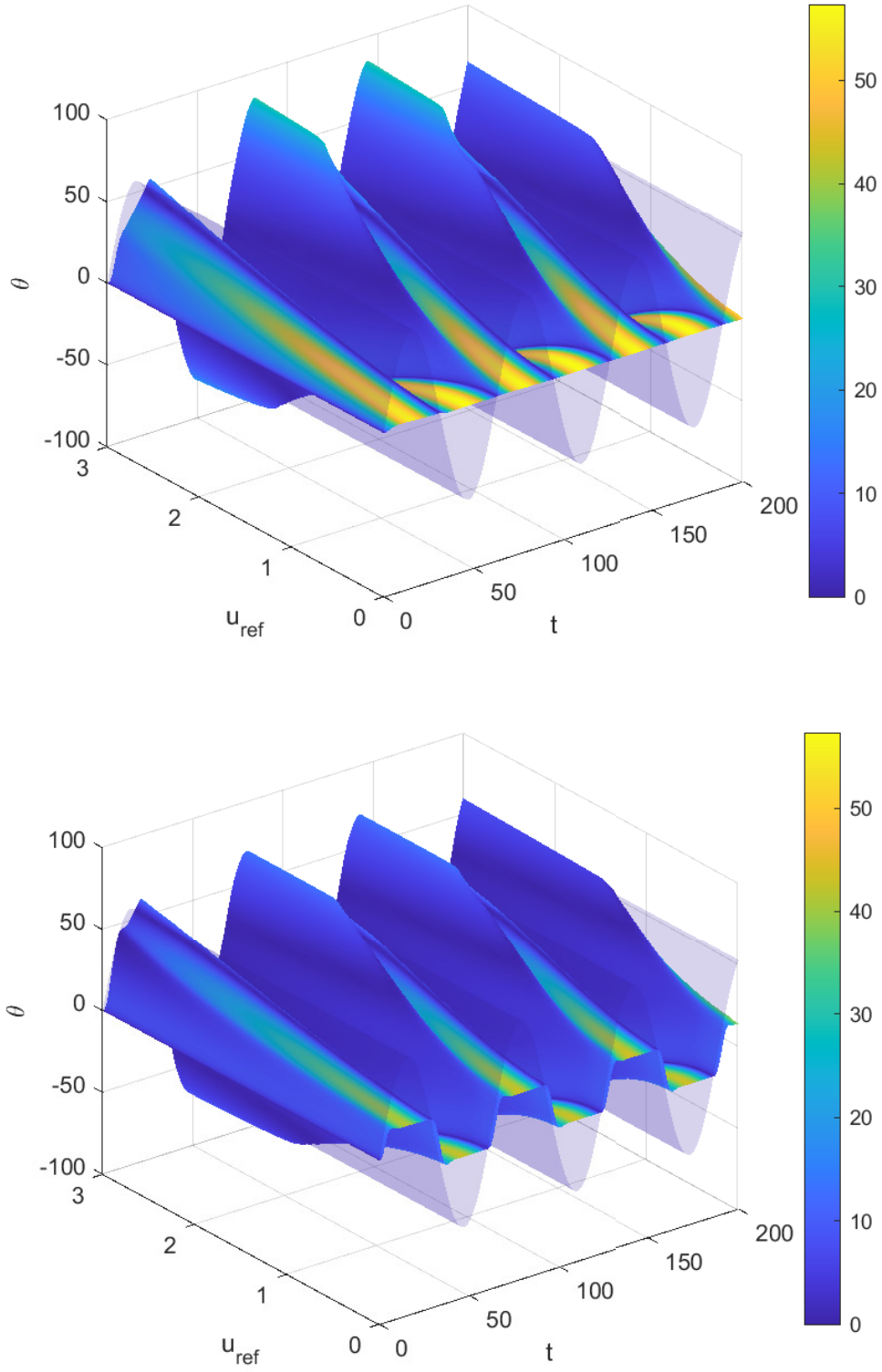

Figure 5.5: Simulated Pitch response following sine reference, colored by absolute pitch error $|e_\theta|$. Pitch reference (transparent) and response (solid, colored by error), using dive-plane actuation only (top) and combined actuation (bottom)

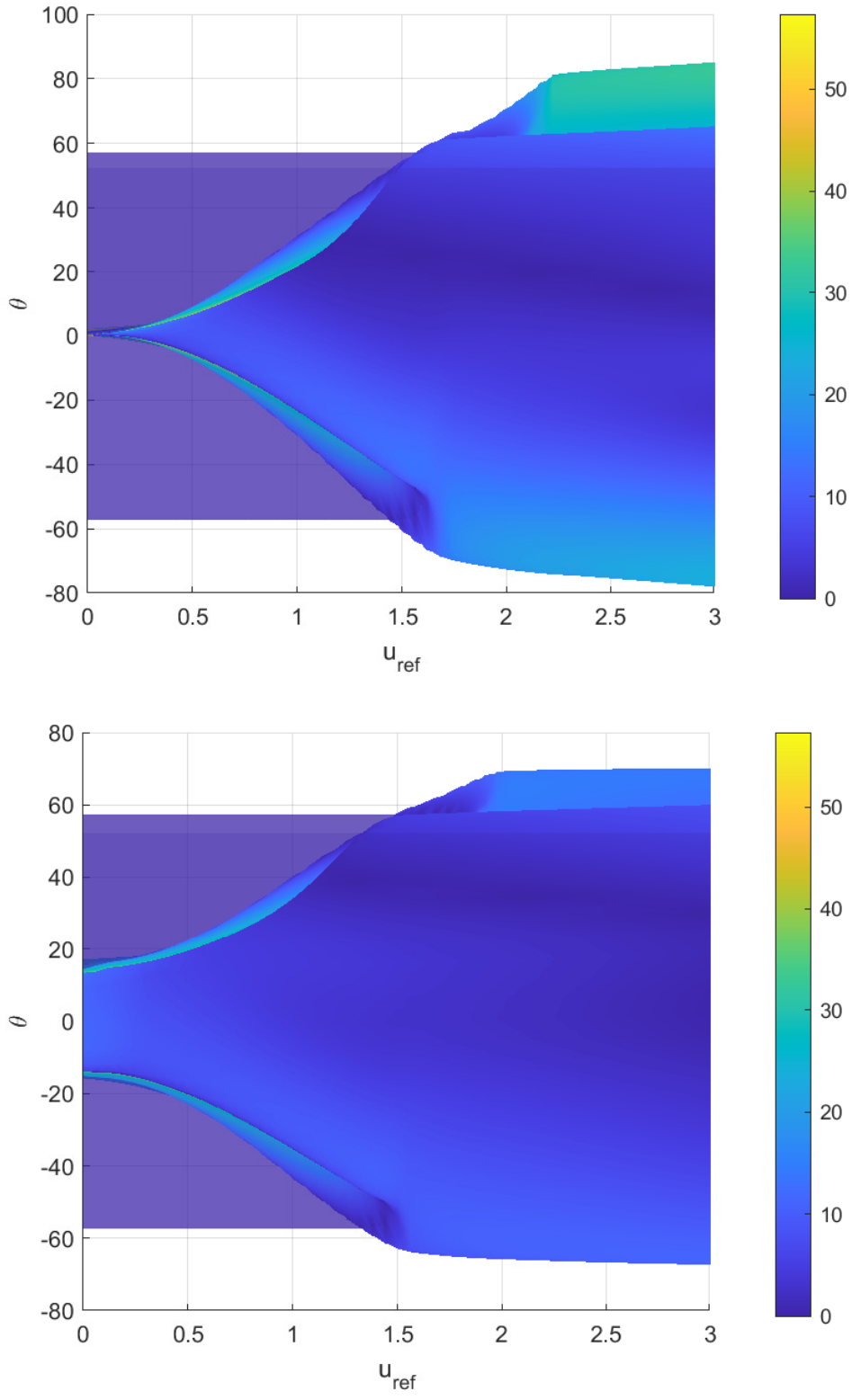

Figure 5.6: Simulated Pitch response following sine reference, colored by absolute pitch error $|e_\theta|$. Pitch reference (transparent) and response (solid, colored by error), using dive-plane actuation only (top) and combined actuation (bottom)

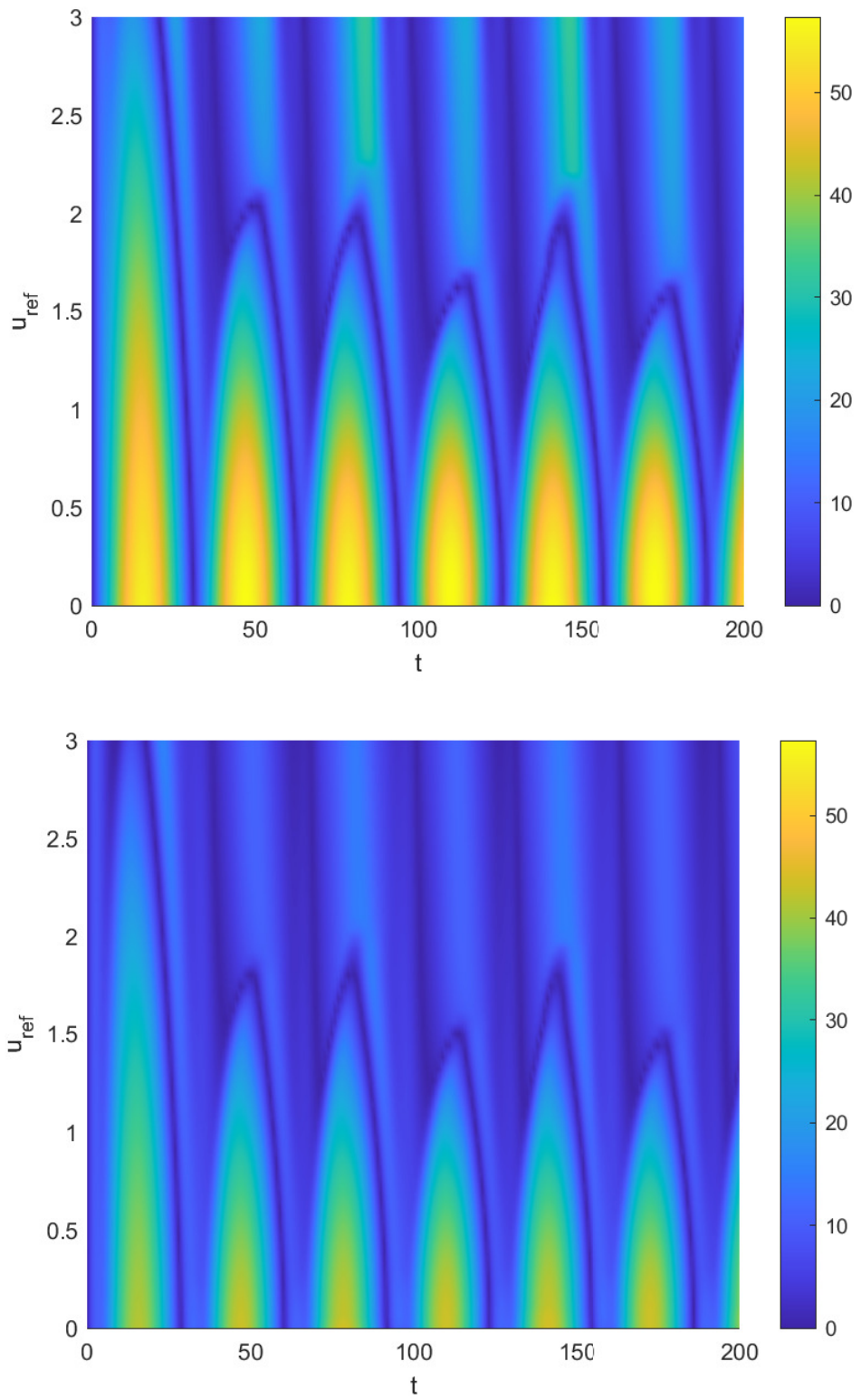

Figure 5.7: Simulated Pitch response following sine reference, colored by absolute pitch error $|e_\theta|$. Using dive-plane actuation only (top) and combined actuation (bottom)

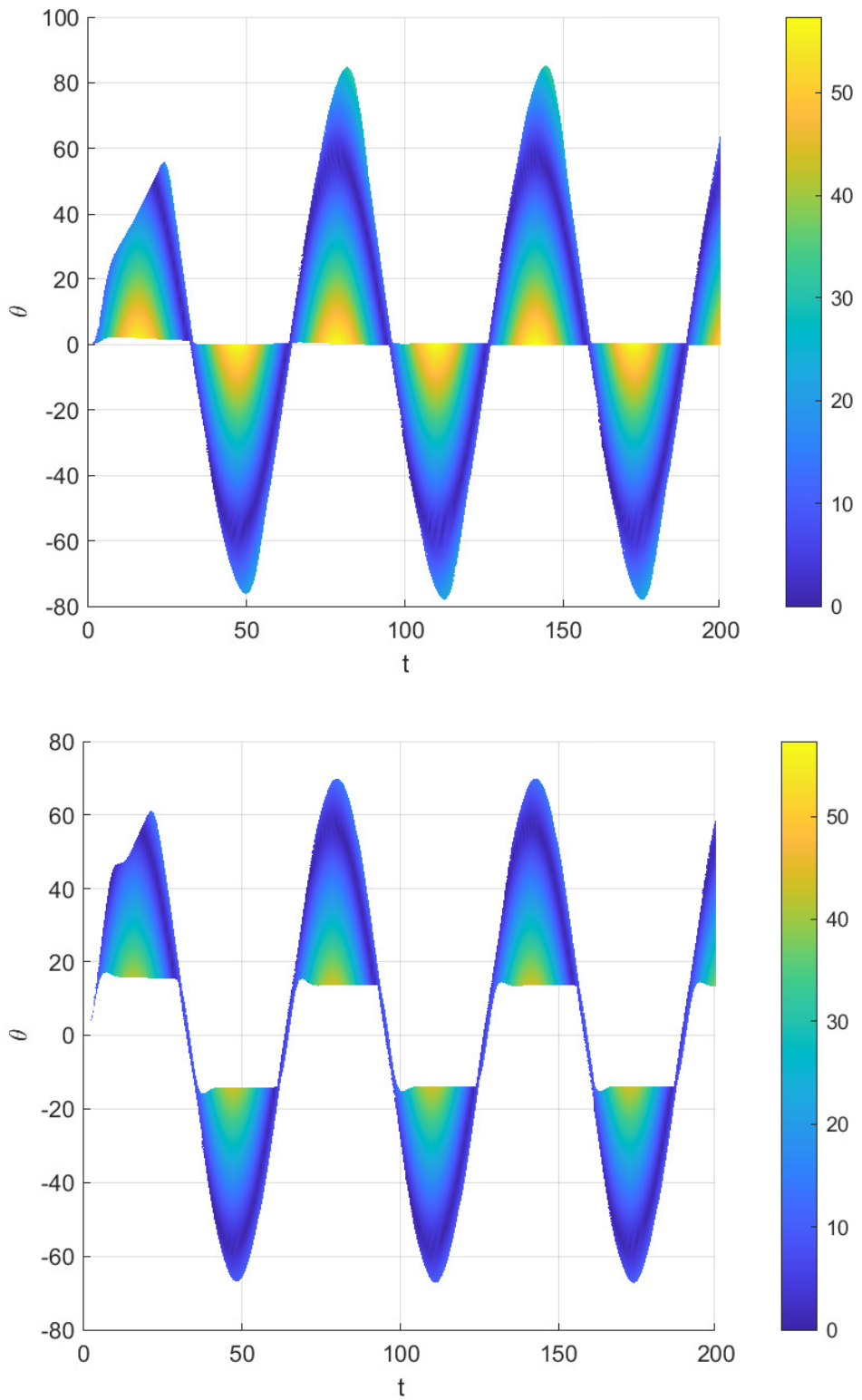

Figure 5.8: Simulated Pitch response following sine reference, colored by absolute pitch error $|e_\theta|$. Using dive-plane actuation only (top) and combined actuation (bottom)

5.3 Current

While the surge velocity mainly affects the performance of the system and mostly causes instabilities in simulation, adding an external disturbance in the form of current might affect the depth control system differently. Performing an initial simulation with constant current:

$$v_c^n = \begin{bmatrix} 0.05 \\ 0 \\ 0.05 \end{bmatrix} \frac{m}{s} \tag{5.2}$$

Adds significant stationary error in both pitch and depth, as shown in Figure 5.9. The integrator does not manage to remove this stationary error due to the integrator limiter, as shown in Figure 5.10 The limiter prevents the integrator from changing since the error e_z is too large.

If the integrator limiter is removed, the depth control system manages to follow the reference trajectory, as shown in Figure 5.11. However, the pitch error is still severe, with $e_\theta \approx 30[deg]$, prompting questions about the feasibility of the control laws in the pitch channel. This is especially apparent when considering that the dive-planes are mostly not active even though the pitch error is far from zero and that a current of $0.05\frac{m}{s}$ is not a significant current velocity. Increasing the current from $0.05\frac{m}{s}$ in x^n and z^n to $0.1\frac{m}{s}$ further amplifies this discrepancy to the point where the pitch is always positive, as shown in Figure 5.12, rendering the depth control system useless. However, if instead of using the explicit steady-state control law from section 3.3, implementing pitch feedback and a PD controller as the dive-plane control law results in stable motion, as shown in Figure 5.13. Examining the graph shows that the depth control system now manages to perform the depth maneuver changes as desired.

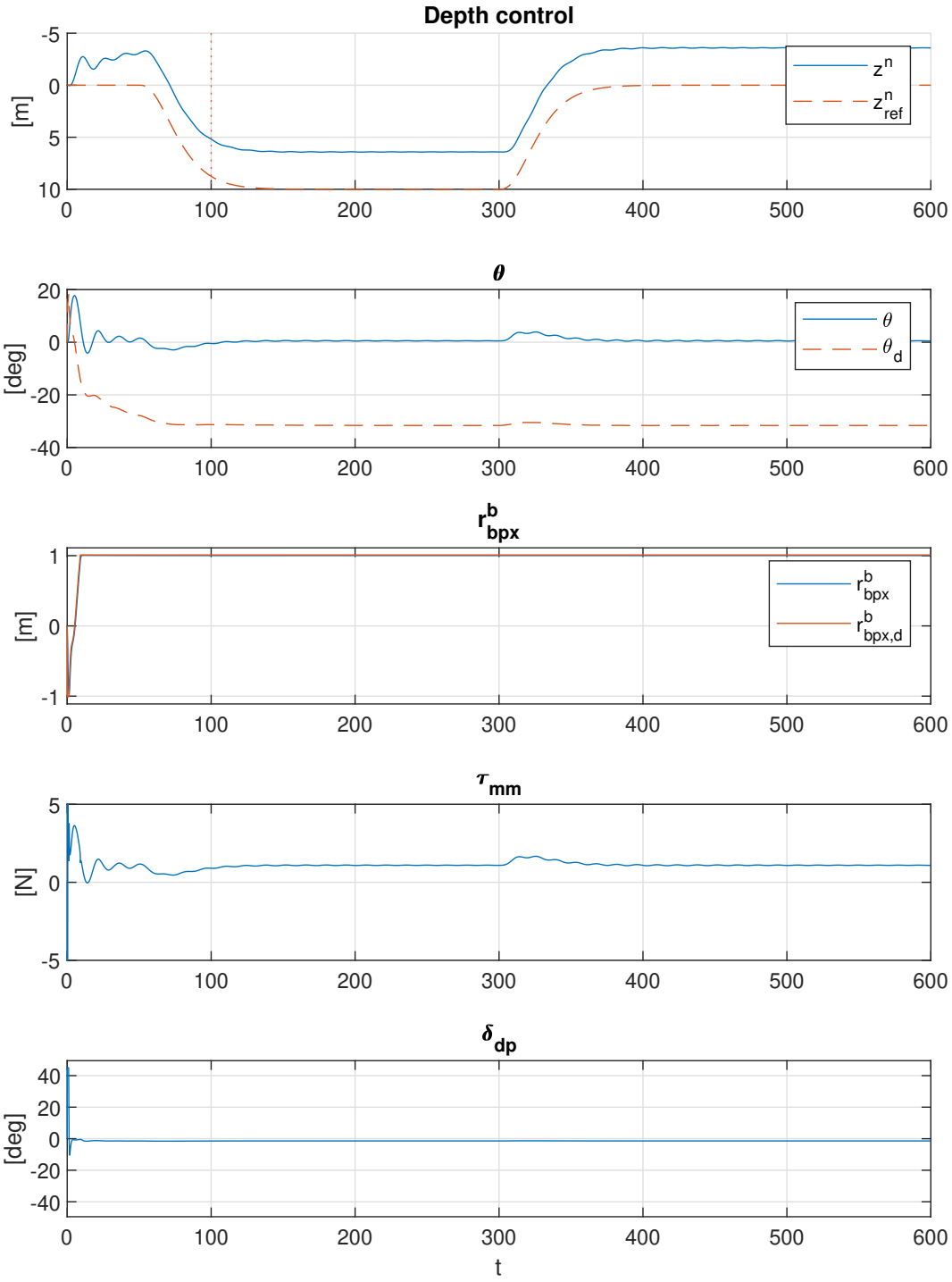

Figure 5.9: Result from initial simulation with added current, as described in section 5.3

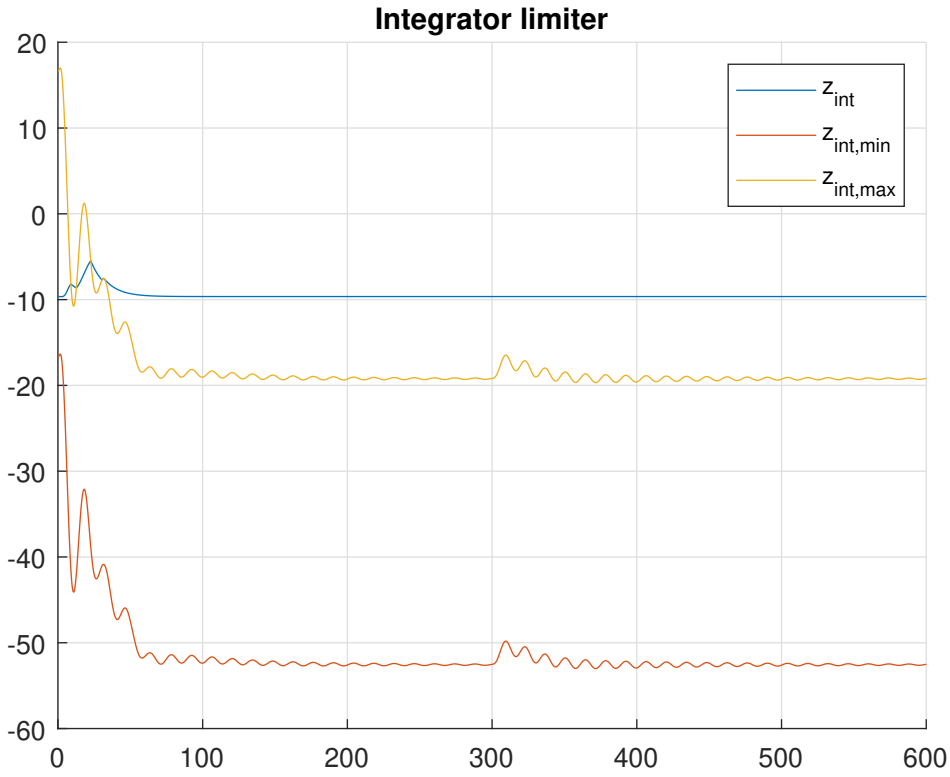

Figure 5.10: Integrator limiter behavior from initial simulation with added current, as described in section 5.3

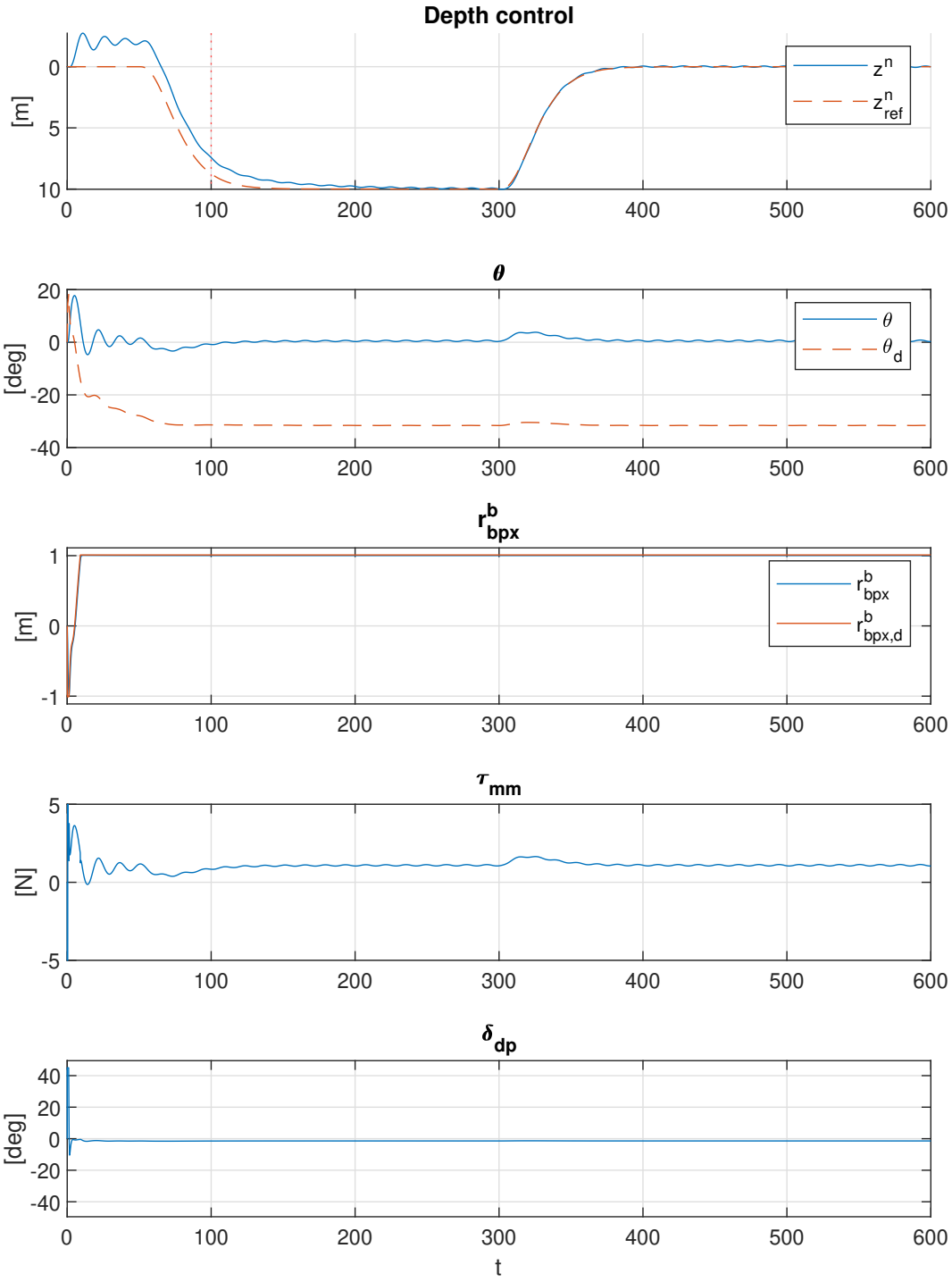

Figure 5.11: Result from simulation with added current when the integrator limiter is removed, as discussed in section 5.3

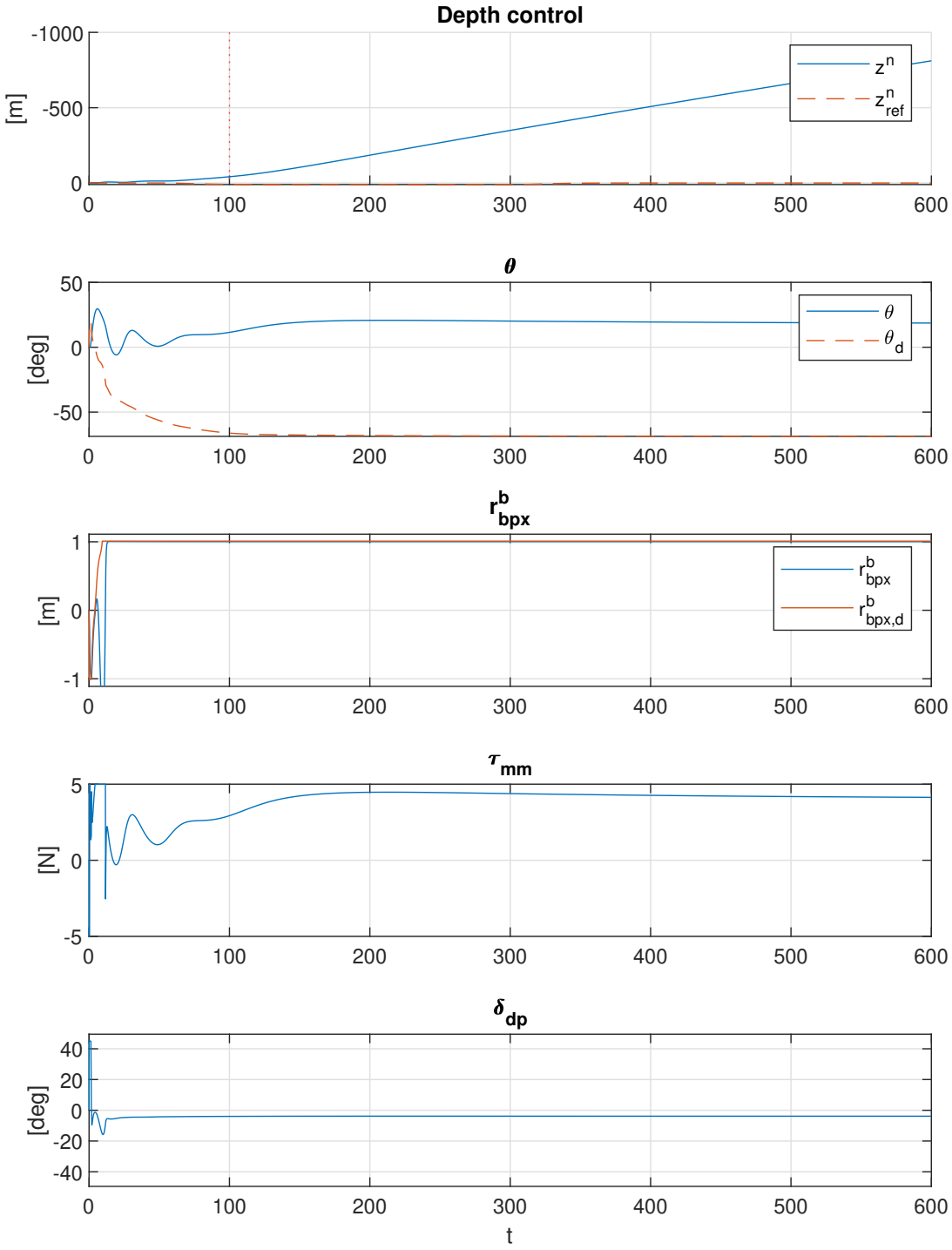

Figure 5.12: Result from increasing current velocity from $0.05\frac{m}{s}$ to $0.1\frac{m}{s}$, as discussed in section 5.3

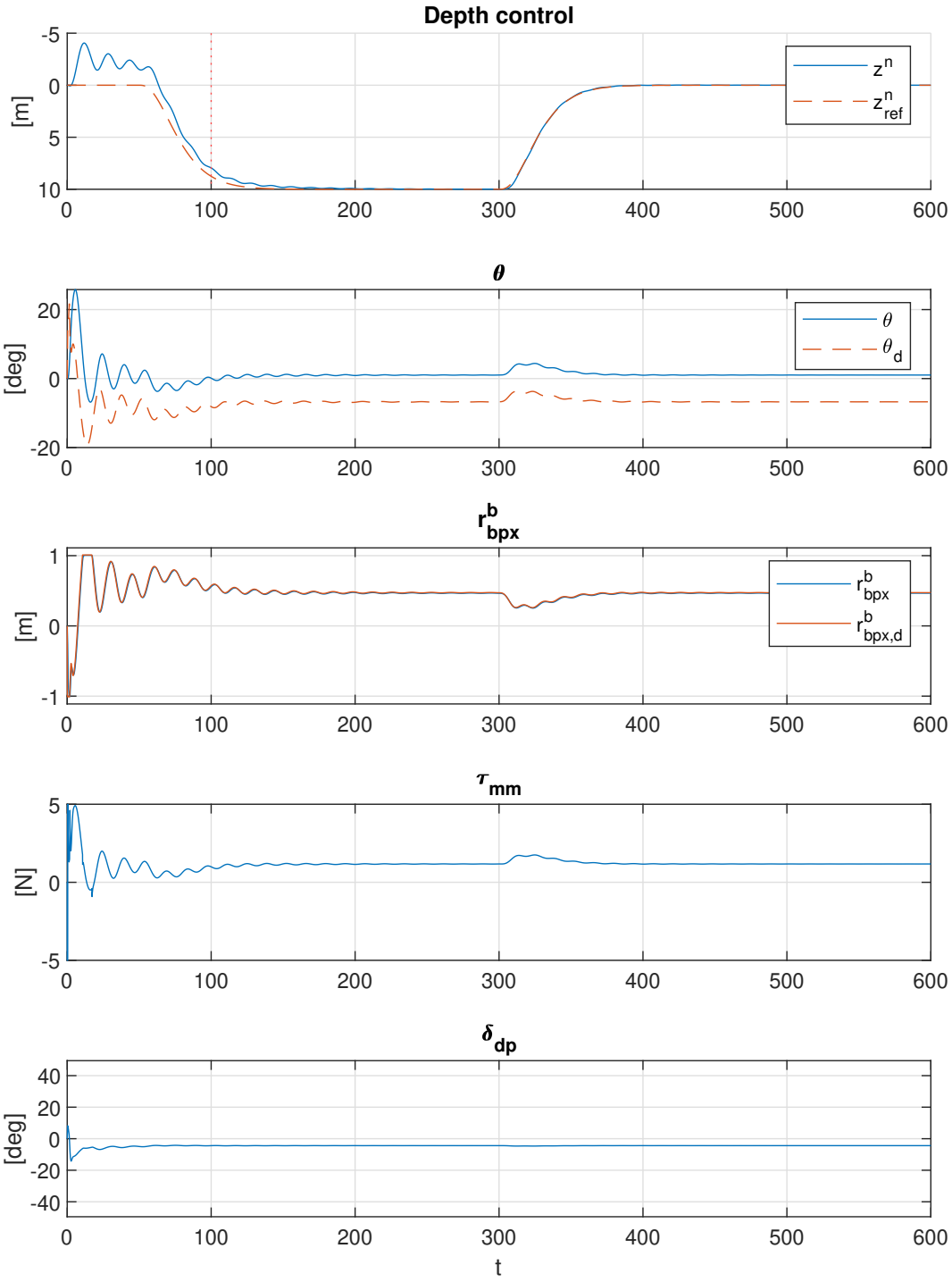

Figure 5.13: Result from changing dive-plane control law from explicit open-loop to PD feedback with current 0.1

5.4 Control Allocation in Pitch

Since the pitch channel has two actuators available, some form of control allocation must be implemented. The open-loop pitch control laws for MMA and dive-planes, as suggested in section 3.2 and 3.3 respectively, implement the actuations in parallel based on the steady-state pitch dynamics, with the MMA actuating over its calculated θ_{max} independent of the dive-planes. As such, the MMA does not provide any control torque for θ_d larger than this, and this is left over for the dive-planes to handle by itself. This configuration means the control authority of the combined pitch controller is limited once θ_d hits θ_{max}. Furthermore, while this configuration considers the actuator limits, the response is not tuneable and entirely dependent on the reference θ_d generated by the depth controller. As such, implementing weighted control allocation is not possible with this configuration.

5.5 MMA as Failsafe Function

Adding MMA to the vehicle adds some redundancy to the control system, considering that MMA and dive-planes act in different mediums and are separated by the vehicle hull. If the dive-planes fails to actuate, the MMA can in principle operate the vehicle without them. However, if the dive-planes hold some position $\delta_{dp,f}$ during actuation failure, they will act as a disturbance dependent on the relative velocity U_r:

$$\frac{1}{m_p g \cos(\theta_d)} \frac{1}{2} \rho_w U_r^2 A_{dp} C_{dp} \delta_{dp,fixed} r^b_{bdp,x} \tag{5.3}$$

As described in equation 3.29. This places a requirement on the point-mass:

$$r^b_{bp,x} > \frac{1}{m_p g \cos(\theta_d)} \frac{1}{2} \rho_w U_r^2 A_{dp} C_{dp} \delta_{dp,f} r^b_{bdp,x} \tag{5.4}$$

To overcome the disturbance provided by the dive-planes. To simplify, assuming small $v^b_{bz} \approx 0$ such that $U_r \approx v^b_{b,x}$ and thus $\alpha_r \approx 0$, the following limitation is examined:

$$r^b_{bp,x} > \frac{1}{m_p g \cos(\theta_d)} \frac{1}{2} \rho_w U_r^2 A_{dp} C_{dp} \delta_{dp,f} r^b_{bdp,x} > \frac{1}{m_p g \cos(\theta_d)} \frac{1}{2} \rho_w u_{ref}^2 A_{dp} C_{dp} \delta_{dp,f} r^b_{bdp,x} \tag{5.5}$$

$$r^b_{bp,x} > \frac{1}{m_p g \cos(\theta_d)} \frac{1}{2} \rho_w u_{ref}^2 A_{dp} C_{dp} \delta_{dp,f} r^b_{bdp,x} \tag{5.6}$$

Assuming the surge velocity subsystem ensures $v^b_{b,x} = u_{ref}$. However, using the values from the table 4, with $u_{ref} = 5$ and maximum dive-plane actuation $\delta_{dp,f} = -45[deg]$ provide the requirement:

$$r^b_{bp,x} > 39.91 \geq \frac{39.91}{\cos(\theta_d)} \tag{5.7}$$

Considering that the maximum actuation $r^b_{bp,x,max} = 1$, MMA is not feasible as a redundancy mechanism for this configuration. However, a more generalized requirement can be determined:

$$r^b_{bp,x} > \frac{39.91}{\cos(\theta_d)} = U_r^2 \delta_{dp,f} \frac{2.033}{\cos(\theta_d)} \tag{5.8}$$

Considering that the limit is quadratically dependent on U_r and linearly dependent on $\delta_{dp,f}$, that the relative velocity is controlled by the surge velocity subsystem, and that the dive-planes are significantly more limited ($\delta_{dp} \in \pm 0.7854[rad]$) than the surge velocity $u_{ref} \in [0, 8][\frac{m}{s}]$, MMA can be used as a redundancy option if the failure is detected such that the main thruster can be throttled to limit the surge velocity and thus ensure that the MMA is able to control the vehicle pitch.

5.5.1 Surge Velocity Limit

Again, considering $U_r \approx u_{ref}$ and $\delta_{dp,f} = -45[deg]$, the equation can be rewritten as a limit on the reference velocity:

$$|u_{ref}| < \sqrt{|r^b_{bp,lim,x}\delta_{dp}\frac{\cos(\theta_d)}{2.033}|} \tag{5.9}$$

$$|u_{ref}| < 0.6216\sqrt{|\cos(\theta_d)|} \tag{5.10}$$

Which suggests that to be able to hold a pitch of $\theta_d = 0$, the reference velocity u_{ref} must be smaller than $u_{ref} < 0.6216[\frac{m}{s}]$. [Example]

5.5.2 Performance Over Different Dive-plane Failures

The performance of the system using a slightly higher $u_{ref} = 1$ can be used to simulate the performance of the depth control system considering $\delta_{dp,f}$ over a range $\delta_{dp,f} \in [-45[deg], 45[deg]]$, considering the depth control systems ability to operate under failure of the dive-planes in every configuration within the dive-plane actuator limitations. Approximating the relative velocity as $U_r \approx u_{ref}$ as previously and examining the case of $\theta_d = 0$ provide an estimate of the dive-plane actuation failure limit:

$$\delta_{dp,f} < \frac{r^b_{bp,x,lim}}{2.033u^2_{ref}} \tag{5.11}$$

$$|\delta_{dp,f}| < \frac{1}{2.033 \cdot 1^2} \approx 0.49 \tag{5.12}$$

Suggesting that the depth control system may still be functional for an actuation failure with $|\delta_{dp,f}| < 0.49 \approx 28.2$[deg]. Or, considering that $U_r \geq u$, it may be more correct to state that a failure with $|\delta_{dp,f}| > 28.2$[deg] may leave the depth control system non-functional. Simulating the case over $\delta_{dp,f} \in [\delta_{dp,min}, \delta_{dp,max}]$ provide the result shown in Figure 5.14, with the graph color denoting the absolute depth error $|e_z|$. There, we can see that the MMA is sufficient to act as a redundancy for a significant region of $\delta_{dp,f}$, approximately ranging from $\delta_{dp,f} \in \pm 20[deg]$, however, failures in δ_{dp} larger than this can generally not be compensated for by the MMA without reducing the velocity reference u_{ref} further.

If a failure in the dive-planes is detectable and the failure actuation $\delta_{dp,f}$ is known through for example measurements or estimation, a potential optimization opportunity can be to derive and alter the control law used in the surge subsystem such that the surge velocity is lowered enough for the MMA to overtake the disturbance provided by $\delta_{dp,f}$, but not further, as to maintain the greatest surge velocity while maintaining depth control of the vehicle. Recalling the steady-state

pitch relation from section 3.3:

$$-m_v g \sin(\theta) r^b_{bg,z} - m_p g \cos(\theta) r^b_{bp,x} + \frac{1}{2}\rho_w U_r^2 A_{dp} C_{dp} \delta_{dp} r^b_{bdp,x} = 0 \tag{5.13}$$

$$m_v g \sin(\theta) r^b_{bg,z} + m_p g \cos(\theta) r^b_{bp,x} = \frac{1}{2}\rho_w U_r^2 A_{dp} C_{dp} \delta_{dp} r^b_{bdp,x} \tag{5.14}$$

Consider now the case where the dive-planes fail to actuate and is now stuck in some position $\delta_{dp,f}$. Assuming that the relative velocity can be described as $U_r \approx C_u u_{ref}$, with some constant $C_u \approx 1$, the point-mass m_p must be able to overcome the disturbance created by the dive-planes at $r^b_{bp,x,max}$, providing:

$$m_v g \sin(\theta_d) r^b_{bg,z} + m_p g \cos(\theta_d) r^b_{bp,x,max} > \frac{1}{2}\rho_w C_u^2 u_{ref}^2 A_{dp} C_{dp} \delta_{dp,f} r^b_{bdp,x} \tag{5.15}$$

$$u_{ref} < \sqrt{\frac{2}{\rho_w C_u^2 A_{dp} \delta_{dp,f} r^b_{bdp,x}} (m_v g \sin(\theta_d) r^b_{bg,z} + m_p g \cos(\theta_d) r^b_{bp,x,max})} \tag{5.16}$$

The constant C_u acts both as a tunable margin and as a ratio $C_u = \frac{U_r}{u_{ref}}$. As such, increasing the constant provides a stricter requirement, in return of greater margin of error. Considering the configuration (table 4) used in this thesis, $C_u = 1.1$, $\delta_{dp,f} = 10[deg]$ and $\theta_d = 0$ yields the requirement:

$$u_{ref} < 0.9554 \tag{5.17}$$

For this specific case.

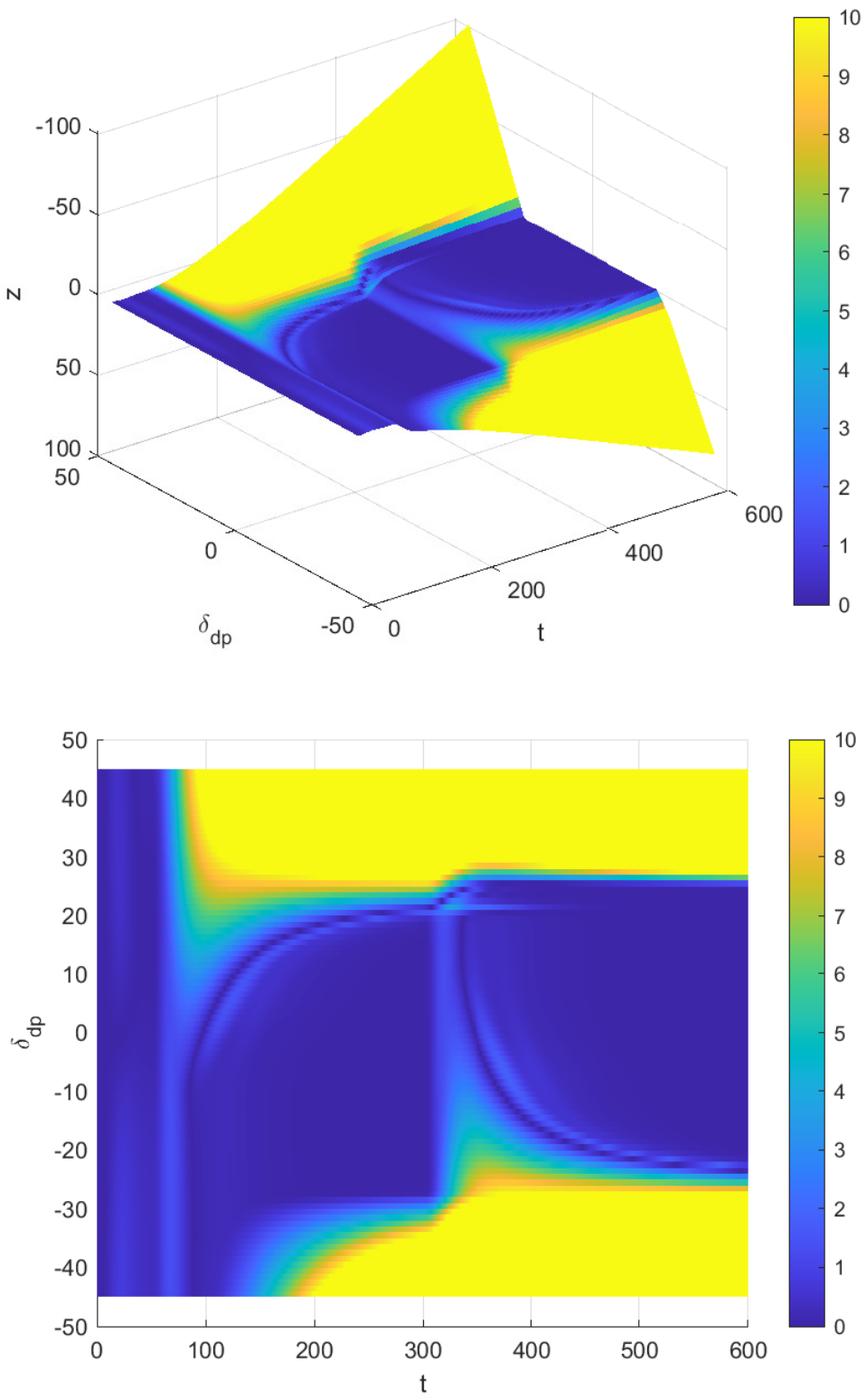

Figure 5.14: Simulated dive- and rise- maneuver at $u_{ref} = 1$ over fixed $\delta_{dp} = \delta_{dp,f}$, color by absolute depth error $|e_z|$. Error used in color is saturated to $|e_z| \in [0, 10]$

5.6 MMA for Drag Reduction

As discussed in section 1.5, MMA has the advantage of not inducing hydrodynamic drag, in contrast with dive-plane actuation. As such, implementing MMA to the depth control system can reduce drag induced by the depth control system, reducing the thrust requirement of the surge subsystem leading to increased mission endurance. Simulating the system using the surge velocity reference $u_{ref} = 1\frac{m}{s}$ and considering the cases of using only the dive-planes, only MMA and the combined actuation yields the result shown in Figure 5.15 and 5.16. While the resulting depth (z^n) and pitch motion is similar for all three cases, the drag induced by the dive-planes in the dive-plane only case affects the main thruster significantly compared to using just MMA or the combined control law, creating a motivating example for reducing the drag. However, some considerations should be made when discussing this approach.

5.6.1 Drag Reduction Considering Explicit Open-Loop Pitch Control

Firstly, the combined actuation with open-loop control effectively acts as the one of most conservative configurations considering drag and the use of the dive-planes, as the dive-planes effectively work mostly to correct small errors in θ when $\theta_d < \theta_{max,mm}$, then only providing significant actuation δ_{dp} once the MMA reaches its saturation limits. As such, using different control laws such as conventional PD control, may provide larger impact on drag than the open-loop explicit control law used in this example. This effect of conservative dive-plane usage can be traced back to the explicit control law for $\delta_{dp,d}$. Recalling it from Equation 3.27:

$$\delta_{dp,d} = -\frac{2}{\rho_w U_r^2 A_{dp} C_{dp} r^b_{bdp,x}} A_\theta \sin(\theta_d - \phi_\theta) \propto A_\theta \sin(\theta_d - \phi_\theta) \tag{5.18}$$

We note that the desired dive-plane actuation is dependent on the phase-corrected $(\theta_d - \phi_\theta)$. Plotting the simulated θ_d and ϕ_θ, shown in Figure 5.17, reveals that the phase ϕ_θ is similar to the angle θ_d until the MMA saturates. Thus, the dive-plane actuation is small until the MMA is saturated, as the phase saturates with the MMA and the corrected $(\theta_d - \phi_\theta)$ then grows to provide actuation in the dive-planes.

5.6.2 Increased Surge Velocity Decreases Dive-Plane Actuation

Secondly, increasing the surge velocity u, and in turn, the relative velocity U_r, affects the performance of the dive-planes. While increased relative velocity quadratically increases the drag for the same actuation δ_{dp}, it also quadratically increases the effectiveness of the dive-planes. And considering that the drag induced is modeled as the square of the actuation δ_{dp}, the drag is reduced when significantly increasing the surge velocity reference u_{ref}, as demonstrated by the simulated result based on $u_{ref} = 5$ provided in Figures 5.18 and 5.19

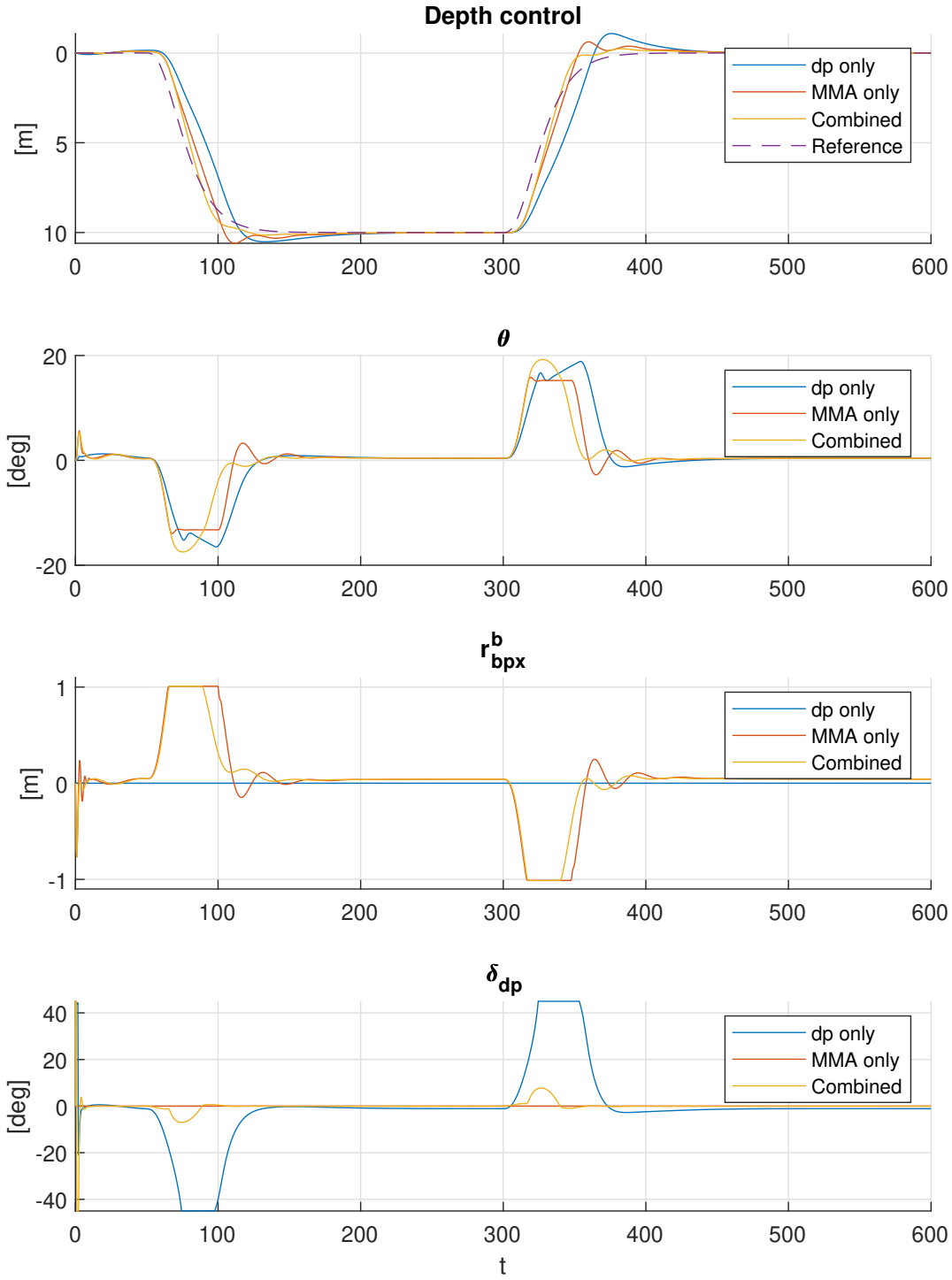

Figure 5.15: Simulated result from depth control system based on dive-planes only (blue), MMA only (red) and combined (yellow), with $u_{ref} = 1\frac{m}{s}$, as discussed in section 5.6

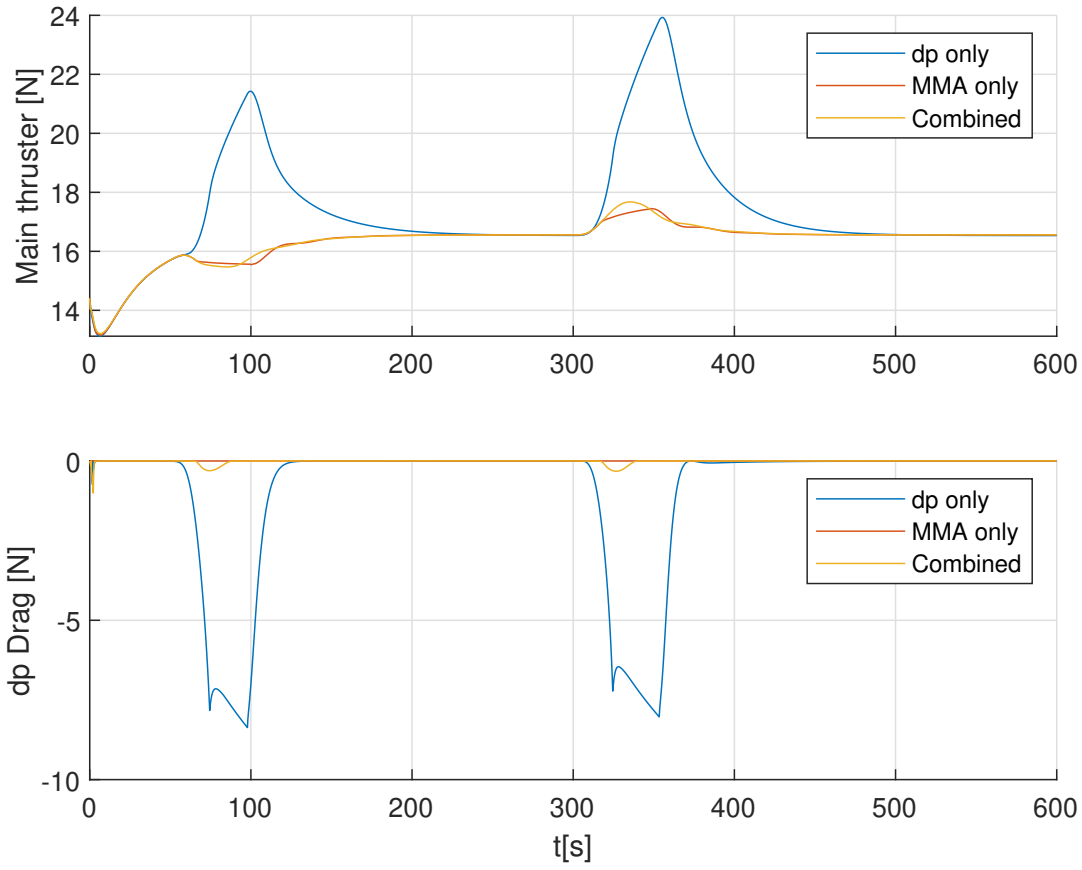

Figure 5.16: Commanded main thruster value from surge veloctiy subsystem and induced drag from dive-planes, considering using only dive-planes, only MMA and the combined control actuation with $u_{ref} = 1\frac{m}{s}$, as discussed in section 5.6. Note that the drag is 'negative' as it is applied in BODY-frame

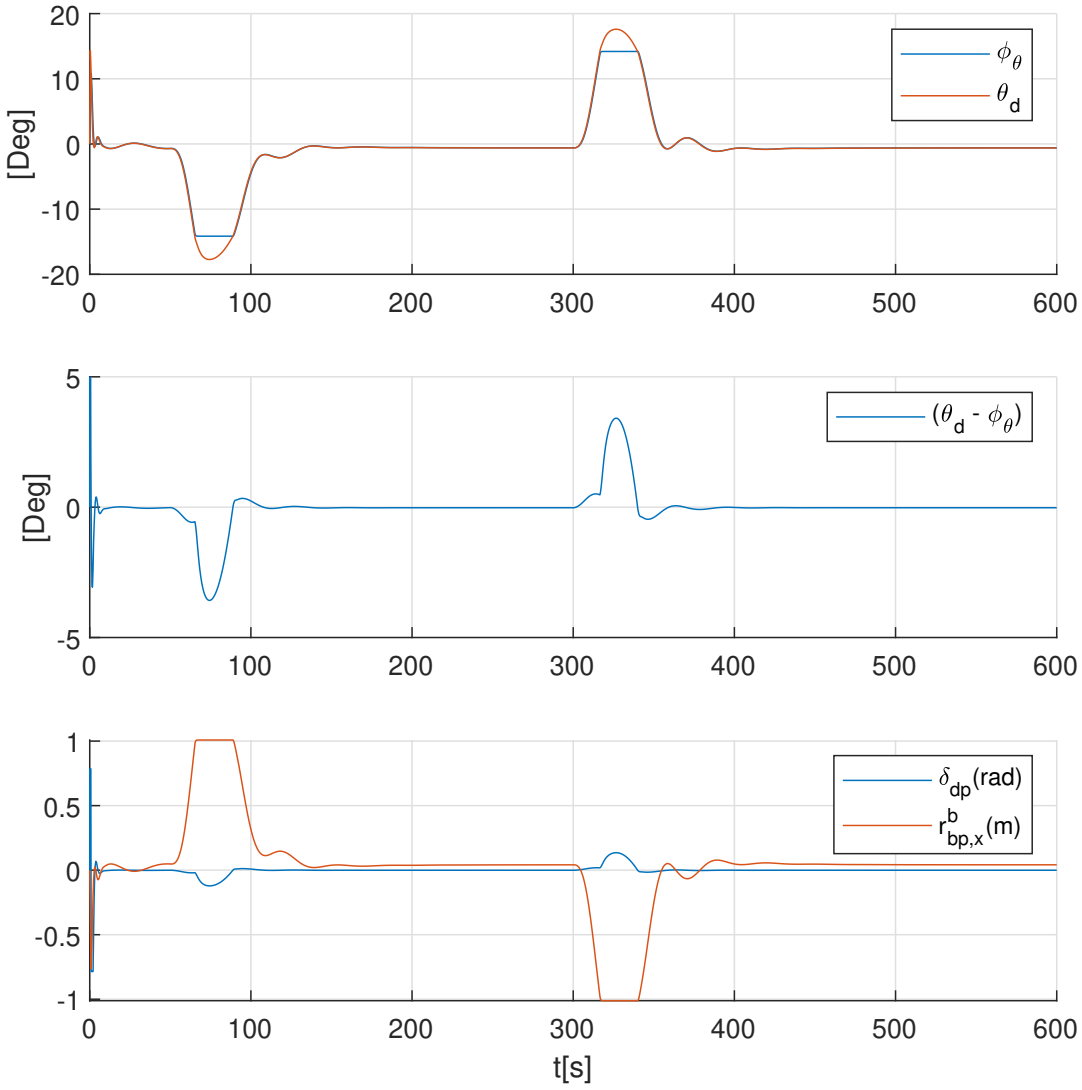

Figure 5.17: Comparing θ_d with ϕ_θ considering the open-loop explicit control law for dive-planes, as discussed in section 5.6

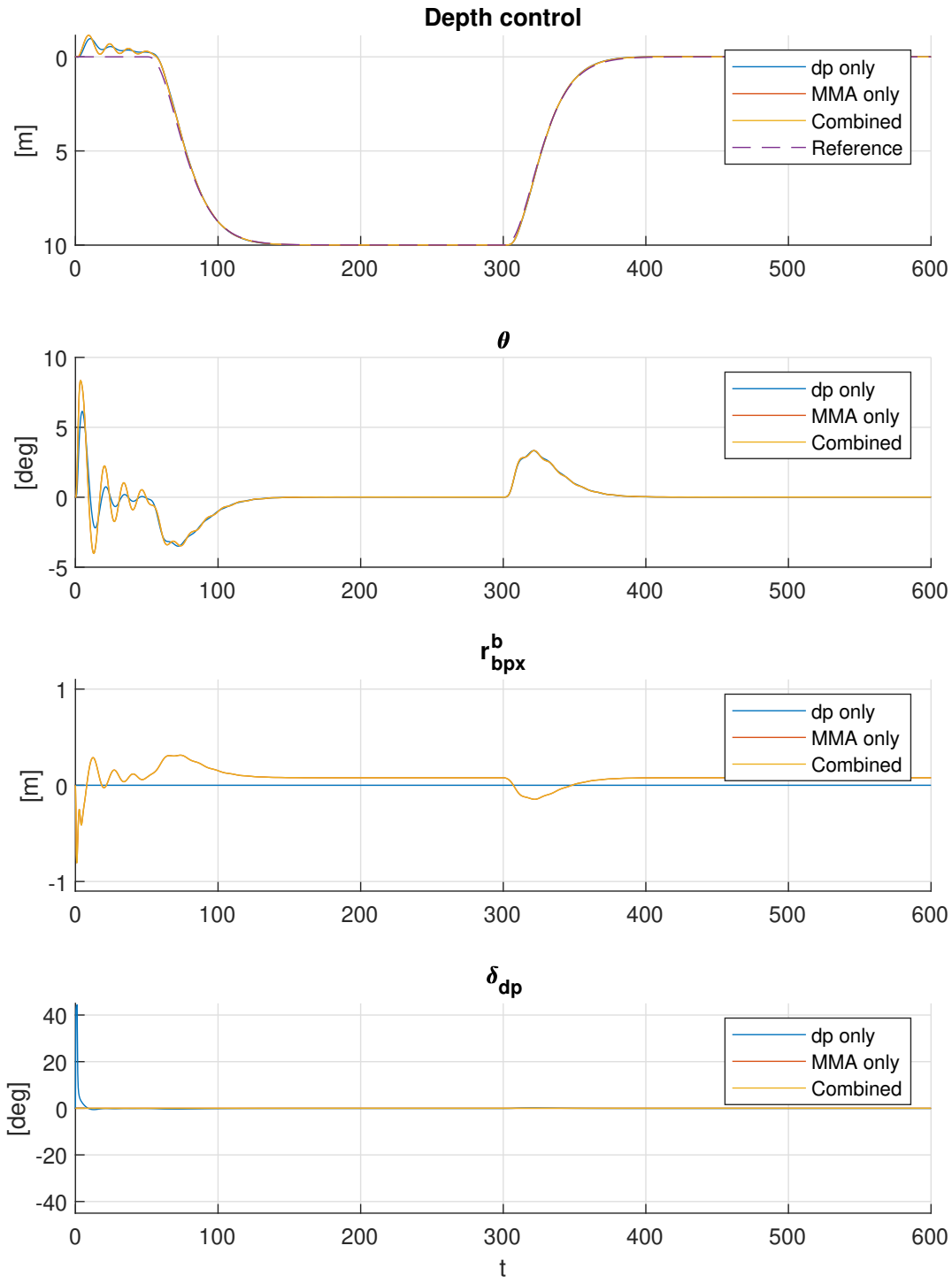

Figure 5.18: Simulated dynamics for increased $u_{ref} = 5\ ^{m}/s$

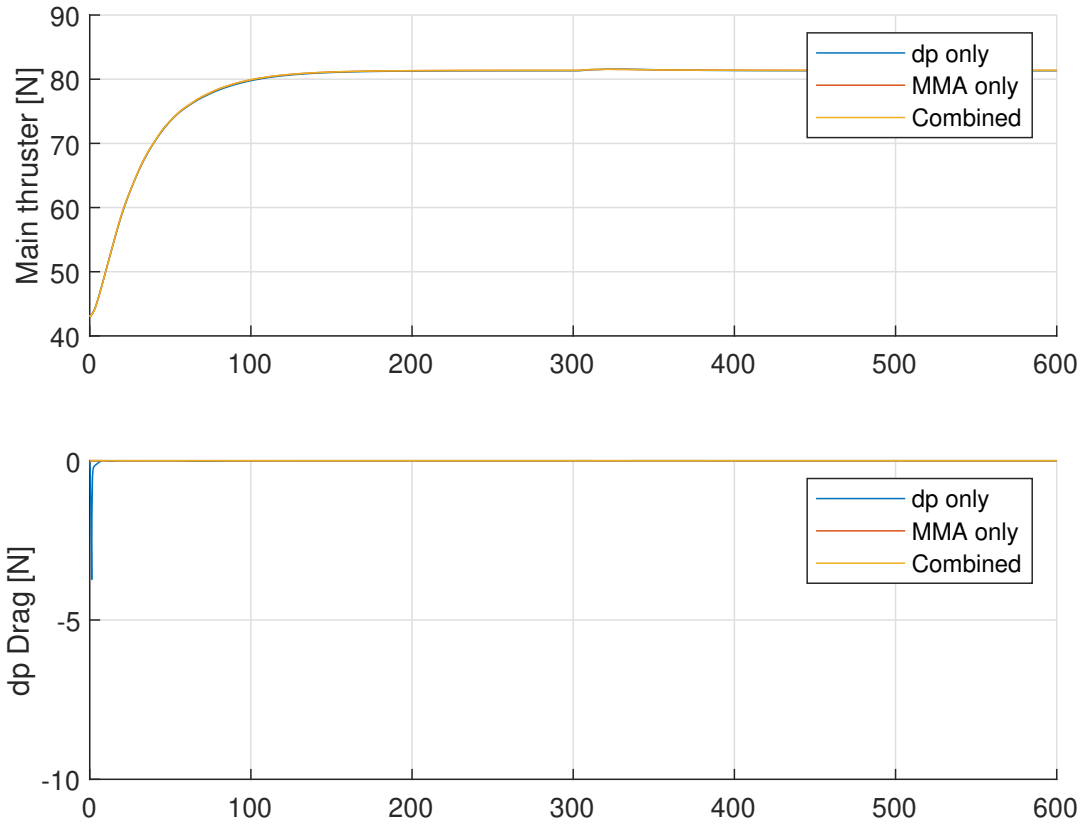

Figure 5.19: Simulated main thruster output (top) and induced dive-planes drag (bottom) for increased $u_{ref} = 5\ ^{m}/_{s}$

5.7 Improvement of using MMA as auxiliary actuatio

So far, the MMA has been assumed to be allowed to actuate across the entire length of the vehicle. However, this imposes strict volumetric constraints on the vehicle, and as such, the effect of using other limits on the MMA should be explored. As discussed in the literature review performed in this thesis, using the battery pack as the movable mass has already been discussed and implemented. As such, this case therefore considers a larger moved mass $m_p = 4[kg]$, and simulates the diving- and rising- maneuver over $r^b_{bp,x,max} \in [0, 1][m]$. Note that this limit is implemented in both directions of the vehicle, meaning that using, for example, $r^b_{bp,x,max} = 0.5[m]$, means the MMA has $0.5[m]$ of actuation in both positive and negative body axis. The result of this simulation is presented in Figures 5.20, 5.21 and 5.22.

Notably, implementing MMA gradually with a limit from $0[m]$ to around $0.2[m]$ gradually decreases the drag induced from the dive-planes, as seen in Figure 5.22, with limited effect on the main thruster force F_u. However, increasing the limit further sharply decreases the drag, before it the drag starts flattening out before becoming negligible. Interestingly, increasing the limit past $r^b_{bp,x,max} > 0.6$ results in an overshoot during the diving maneuver, sharply increasing the main thruster force. However, this might occur due to oscillations that have not settled before the maneuvers start, and the simulation should be repeated with a longer stabilizing time before the maneuvers start before making conclusions about how increasing the limit past 0.6 affect the response. However, considering that the goal of this case is to limit the MMA. As such, examining the figures, we can conclude that using a limit larger than 0.4 for this configuration is unnecessary, as it does not reduce drag or improve depth control any further.

Alternatively, a more conservative suggestion of $r^b_{bp,x,max} = 0.25$ can be used to get a significant portion of the drag reduction while being conservative with the space requirement of the MMA. Using this limit would, in this case, reduce the drag from the dive planes, and in turn, the main thruster force by approximately $5[N]$, or about $\frac{1}{7}$ of the non-MMA case (that is, the simulated result for $r^b_{bp,x,max} = 0$.

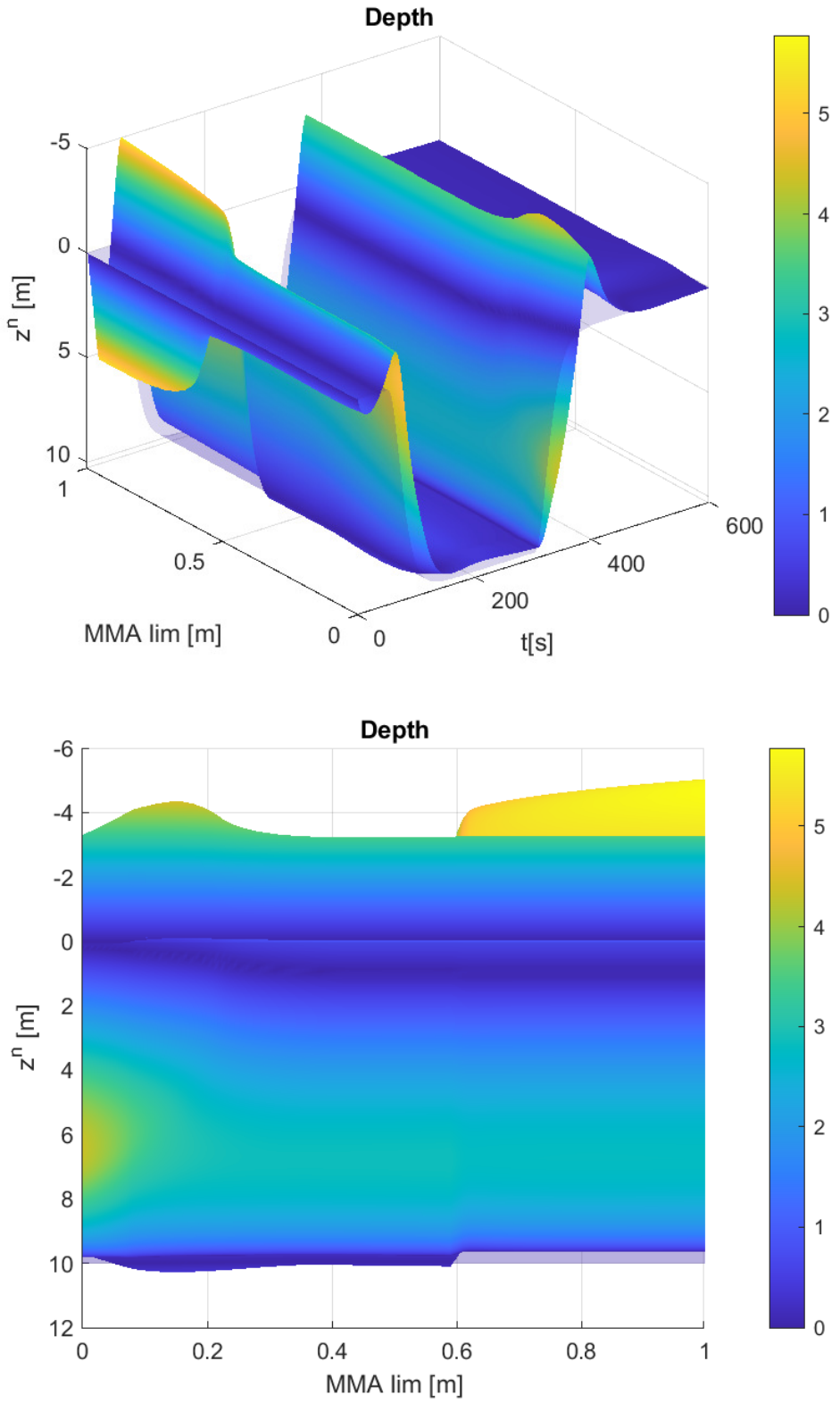

Figure 5.20: Depth control over MMA limit. Color by absolute depth error $|e_z|$

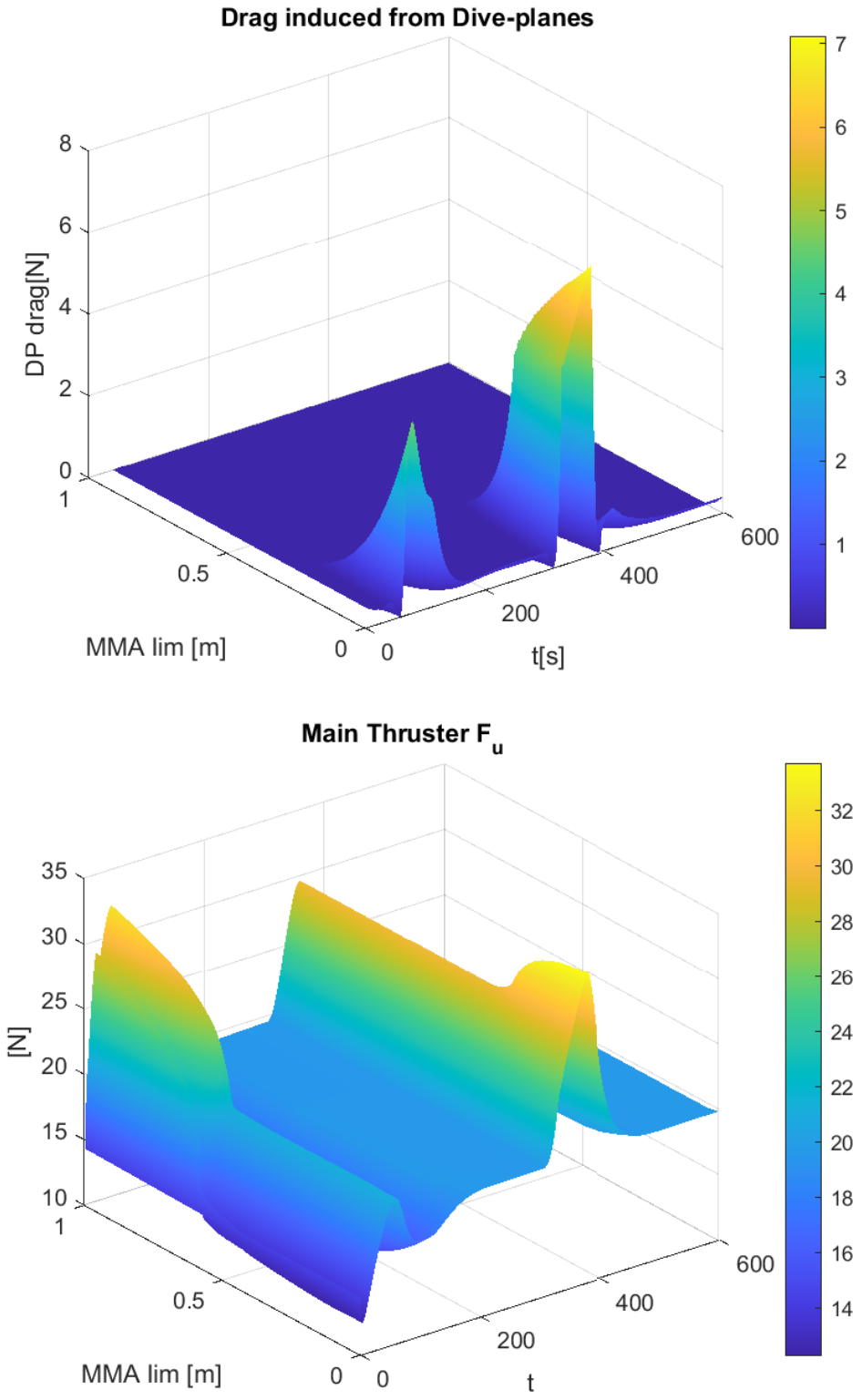

Figure 5.21: Main thruster F_u and drag induced by Dive-planes over MMA limit. Color by absolute plotting value. Values of drag before $t = 40[s]$ has been removed due to oscilations occuring before the vehicle stabilized properly before maneuvers

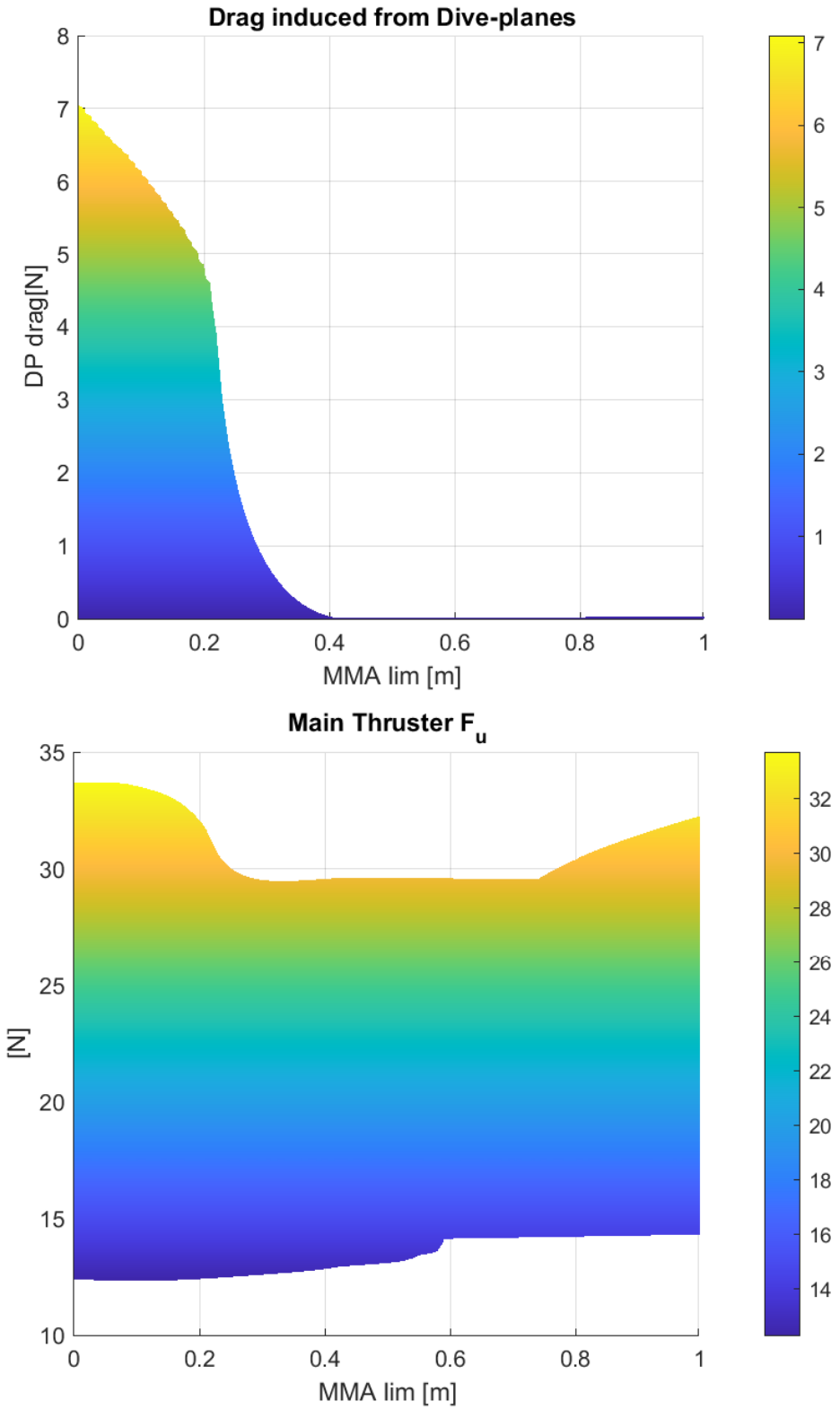

Figure 5.22: Main thruster F_u and drag induced by Dive-planes over MMA limit. Color by absolute plotting value

5.8 Discussion on General Results

As discussed, the mass ratio between the point-mass and the vehicle mass denoted σ_p. In this thesis, a configuration with a small mass ratio is been discussed, with a large actuation limit $r^b_{bp,x,max}$ to increase the available torque providable by the MMA. Whether it is more feasible to increase the mass size instead of the actuation length is left out of scope for this thesis to discuss. The maximum velocity of the moving-mass is directly tied to the bandwidth of reference $r^b_{bp,d}$, and since the control law for MMA proposed in this thesis is explicitly defined from the reference θ_d generated by the depth control system, the resulting actuator force and velocity requirements are directly dependent on the bandwidth of the depth controller. As such, the depth control system must be designed to not exceed the actuator limitations in bandwidth. This also means that decreasing the response from the depth control system will lead to lower power consumption, effectively relating the performance of the depth control to the MMA actuation limitations. The use of control allocation could also be used in the combined system to optimize actuation based on the surge velocity to limit the usage of dive-planes in low-speed conditions.

Overall, the explicit open-loop pitch control laws have shown reasonable performance for the depth control system. However, adding even a small ocean current of $0.05^m/s$ to the simulation created a significant stationary error in depth, and adding more destabilized the depth control system. As such, implementing this open-loop control law is not effective when currents are present. However, changing the dive-planes to use conventional PD control provided sufficient controllability. But, since the dive-plane control effectiveness is dependent on the relative velocity, this solution would not work for small U_r. As such, using open-loop control for MMA is not feasible for situations of low-speed relative velocity with currents present, and pitch feed-back should therefore be implemented to handle this disturbance.

Chapter 6

Conclusion

In this thesis, a literature study on moving-mass actuation and control considering various moving-mass configurations and applications has been performed. The implementation of an MMA control system has been modeled, discussed, and simulated in various cases considering comparisons with conventional dive-plane actuation, varying surge velocities, and in constant currents. Implementation of MMA has been simulated and discussed both as a control system for both attitude (pitch) and depth. Case studies examining the performance of MMA as a sole actuator, a failsafe function, a drag reduction method, and as an auxiliary actuator has been simulated and discussed. The usage of open-loop control laws for MMA and combined actuation has been discussed with considerations of its limits considering ocean current.

Finally, the research questions from the problem statement are answered:

- **Q1:** For the configuration proposed in this thesis, MMA can be used as the sole actuator in depth control, provided a non-zero vehicle velocity, as demonstrated in figure A.2
- **Q2:** The MMA configuration proposed in this thesis does not significantly alter the performance of the depth control system at a nominal surge velocity $u = 1\ ^m/s$, as shown in Figure 5.15, though it has the potential to reduce drag induced by dive-planes
- **Q3:** MMA is generally favorable in low-speed cases, allowing for attitude control at zero velocity. They can also be used to reduce the usage of dive-planes, reducing drag. Since MMA generally is shielded from the environment, it can act as a redundant actuator, even if the dive-planes are fixed in an undesirable position $\delta_{dp,f}$
- **Q4:** The saturation limits on the control system impose a maximum pitch, and thus, descent rate. This can cause integral windup, but can be removed by velocity saturation of depth reference model and/or limiting the integrator variable

Bibliography

[1] Xiaoming Wang, Wenya Zhou, Ruinan Mu, Zhigang Wu, A new deformation control approach for flexible wings using moving masses Aerospace Science and Technology, Volume 106, 2020, 106118, ISSN 1270-9638, https://doi.org/10.1016/j.ast.2020.106118

[2] Shahin Darvishpoor, Jafar Roshanian, Morteza Tayefi, A novel concept of VTOL bi-rotor UAV based on moving mass control, Aerospace Science and Technology, Volume 107, 2020, 106238, ISSN 1270-9638, https://doi.org/10.1016/j.ast.2020.106238

[3] Haus, T., Orsag, M. & Bogdan, S. Mathematical Modelling and Control of an Unmanned Aerial Vehicle with Moving Mass Control Concept. J Intell Robot Syst 88, 219-246 (2017). https://doi.org/10.1007/s10846-017-0545-2

[4] Jianqing Li, Changsheng Gao, Chaoyong Li, Wuxing Jing, A survey on moving mass control technology, Aerospace Science and Technology, Volumes 82-83, 2018, Pages 594-606, ISSN 1270-9638, https://doi.org/10.1016/j.ast.2018.09.033

[5] Zhengliang Lu, Yuandong Hu, Wenhe Liao, Xiang Zhang, Modeling and attitude control of CubeSat utilizing moving mass actuators, Advances in Space Research, Volume 67, Issue 1, 2021, Pages 521-530, ISSN 0273-1177, https://doi.org/10.1016/j.asr.2020.09.027

[6] He Huang, Jun Zhou, Solar sailing CubeSat attitude control method with satellite as moving mass, Acta Astronautica, Volume 159, 2019, Pages 331-341, ISSN 0094-5765, https://doi.org/10.1016/j.actaastro.2019.03.077

[7] Khalid Isa, M.R. Arshad, Syafizal Ishak, A hybrid-driven underwater glider model, hydrodynamics estimation, and an analysis of the motion control, Ocean Engineering, Volume 81, 2014, Pages 111-129, ISSN 0029-8018, https://doi.org/10.1016/j.oceaneng.2014.02.002

[8] Ziaeefard, S., Page, B.R., Pinar, A.J. et al. Effective Turning Motion Control of Internally Actuated Autonomous Underwater Vehicles. J Intell Robot Syst 89, 175-189 (2018). https://doi.org/10.1007/s10846-017-0544-3

[9] F. Wu and Z. Geng, Energy shaping for stably coordinating internally actuated underwater vehicles, Proceedings of the 30th Chinese Control Conference, 2011, pp. 347-353.

[10] Woolsey, Craig A. (2009). Internally Actuated Lateral-Directional Maneuvering for a Blended Wing-Body Underwater Glider.

[11] C. L. Nickell, C. A. Woolsey and D. J. Stilwell, A low-speed control module for a streamlined AUV, Proceedings of OCEANS 2005 MTS/IEEE, 2005, pp. 1680-1685 Vol. 2, doi: 10.1109/OCEANS.2005.1639997.

[12] Li, B., Wang, L., Wang, X. et al. Cross-coupling effect and motion control of an autonomous underwater vehicle with internal actuators. J Mar Sci Technol 24, 98-110 (2019). https://doi.org/10.1007/s00773-018-0534-6

[13] A Latifah et al 2019 J. Phys.: Conf. Ser. 1402 044018. Depth control design and simulation of hybrid underwater glider https://doi.org/10.1088/1742-6596/1402/4/044018

[14] Hans Cozijn, Haite van der Schaaf, Bas de Kruif, Egbert Ypma, Design of an Underwater Vehicle for use in Basin Experiments, Development of MARINâ€™s Modular AUV, IFAC-PapersOnLine, Volume 52, Issue 21, 2019, Pages 21-26, ISSN 2405-8963, https://doi.org/10.1016/j.ifacol.2019.12.277

[15] Li, B., and Su, T. (December 2, 2016). "Heading Autopilot of Autonomous Underwater Vehicles With Internal Moving Mass." ASME. J. Comput. Nonlinear Dynam. March 2017; 12(2): 021003. https://doi.org/10.1115/1.4034727

[16] N. E. Leonard and J. G. Graver, "Model-based feedback control of autonomous underwater gliders," in IEEE Journal of Oceanic Engineering, vol. 26, no. 4, pp. 633-645, Oct. 2001, doi: 10.1109/48.972106.

[17] Zhao, E., Song, B.W., 2011. Modeling and Variable Structure Control of Autonomous Underwater Vehicles with Moving Mass. AMM 130-134, 1963-1967. https://doi.org/10.4028/www.scientific.net/amm.130-134.1963

[18] Bo Li, Tsung-Chow Su, Nonlinear heading control of an autonomous underwater vehicle with internal actuators, Ocean Engineering, Volume 125, 2016, Pages 103-112, ISSN 0029-8018, https://doi.org/10.1016/j.oceaneng.2016.08.010

[19] Jianqing Li, Sai Chen, Chaoyong Li, Changsheng Gao, Wuxing Jing, Adaptive control of underactuated flight vehicles with moving mass, Aerospace Science and Technology, Volume 85, 2019, Pages 75-84, ISSN 1270-9638, https://doi.org/10.1016/j.ast.2018.12.003

[20] Pengxin Wei, Wei Wei, Changsheng Gao, Wuxing Jing, Dynamics and control authority of a flight vehicle equipped with a translating moving mass and rotating rail, Aerospace Science and Technology, Volume 108, 2021, 106396, ISSN 1270-9638, https://doi.org/10.1016/j.ast.2020.106396

[21] Changsheng Gao, Jianqing Li, Yidi Fan, Wuxing Jing, Immersion and invariance-based control of novel moving-mass flight vehicles, Aerospace Science and Technology, Volume 74, 2018, Pages 63-71, ISSN 1270-9638, https://doi.org/10.1016/j.ast.2017.12.017

[22] P. K. Menon, G. D. Sweriduk, E. J. Ohlmeyer, and D. S. Malyevac, Integrated Guidance and Control of Moving-Mass Actuated Kinetic Warheads, Journal of Guidance, Control, and Dynamics 2004 27:1, 118-126, https://doi.org/10.2514/1.9336

[23] Wei, P., Gao, C. & Jing, W. Longitudinal Aerodynamic Coefficients Estimation and Identifiability Analysis for Hypersonic Glider Controlled by Moving Mass. Int. J. Aeronaut. Space Sci. 20, 31-43 (2019). https://doi.org/10.1007/s42405-018-0123-2

[24] Li, J., Gao, C., Jing, W. et al. Nonlinear vibration analysis of a novel moving mass flight vehicle. Nonlinear Dyn 90, 733-748 (2017). https://doi.org/10.1007/s11071-017-3691-y

[25] Li, J., Gao, C., Feng, T., and Jing, W. (June 18, 2018). "Novel Moving Mass Flight Vehicle and Its Equivalent Experiment." ASME. J. Dyn. Sys., Meas., Control. November 2018; 140(11): 111010. https://doi.org/10.1115/1.4040326

[26] Haolan Chen, Jun Zhou, Min Zhou, Bin Zhao, Nussbaum gain adaptive control scheme for moving mass reentry hypersonic vehicle with actuator saturation, Aerospace Science and Technology, Volume 91, 2019, Pages 357-371, ISSN 1270-9638, https://doi.org/10.1016/j.ast.2019.05.041

[27] Kaixu Dong, Jun Zhou, Min Zhou, Bin Zhao, Roll control for single moving-mass actuated fixed-trim reentry vehicle considering full state constraints, Aerospace Science and Technology, Volume 94, 2019, 105365, ISSN 1270-9638, https://doi.org/10.1016/j.ast.2019.105365

[28] Wei, P.-x., Gao, C.-s. and Jing, W.-x. (2014), "Roll control problem for the long-range maneuverable warhead", Aircraft Engineering and Aerospace Technology, Vol. 86 No. 5, pp. 440-446. https://doi.org/10.1108/AEAT-10-2012-0170

[29] Wang, Y.K., Zhang, Z., Mao, J.Q., 2013. Sliding Variable Structure Control for Attitude of Moving-Mass Hypersonic Vehicles. AMM 325-326, 1225-1228. https://doi.org/10.4028/www.scientific.net/amm.325-326.1225

[30] Qiushi Zheng, Zhiming Zhou, "Stability of Moving Mass Control Spinning Missiles with Angular Rate Loops", Mathematical Problems in Engineering, vol. 2019, Article ID 7832602, 10 pages, 2019. https://doi.org/10.1155/2019/7832602

[31] Alexandra Techet. 2.016 Hydrodynamics (13.012). Fall 2005. Massachusetts Institute of Technology: MIT OpenCourseWare, https://ocw.mit.edu. License: Creative Commons BY-NC-SA.

[32] J. Tangler, J. David Kocurek, Preprint, To be presented at the 43rd AIAA Aerospace Sciences Meeting and Exhibit Reno, Nevada January 10-13, 2005, "Wind Turbine Post-Stall Airfoil Performance Characteristics Guidelines for Blade-Element Momentum Methods", accessed from https://www.nrel.gov/docs/fy05osti/36900.pdf

[33] Fossen, T. I (2021). Handbook of Marine Craft Hydrodynamics and Motion Control. 2nd edition, John Wiley & Sons Ltd

[34] SNAME (1950). The Society of Naval Architects and Marine Engineers. Nomenclature for Treating the Motion of a Submerged Body Through a Fluid. In: Technical and Research Bulletin No. 1â€“5.

Appendix A

Additional Figures

Additional figures from the thesis is placed here.

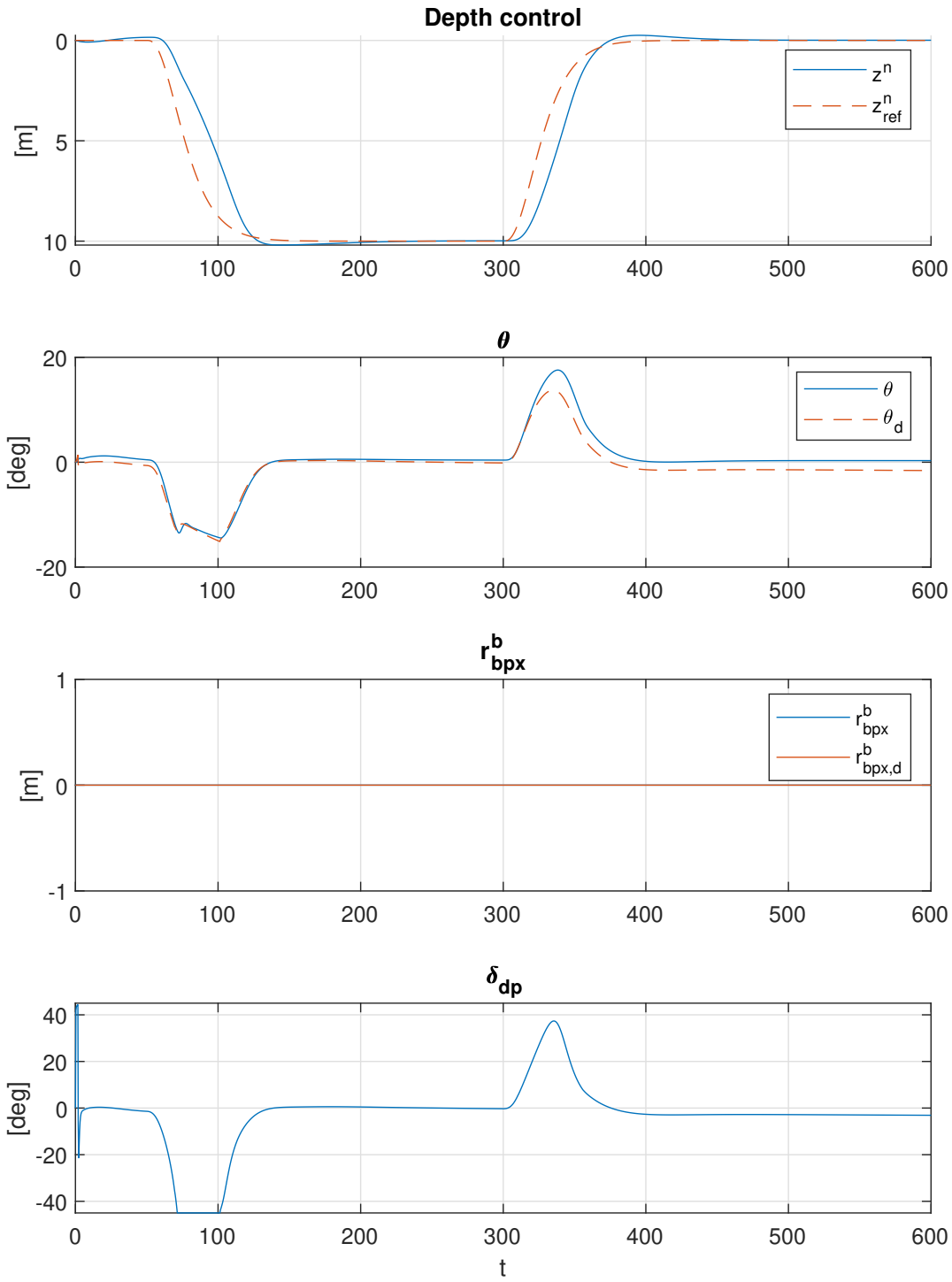

Figure A.1: Result of simulating the system with only Dive-planes, as discussed in section 5

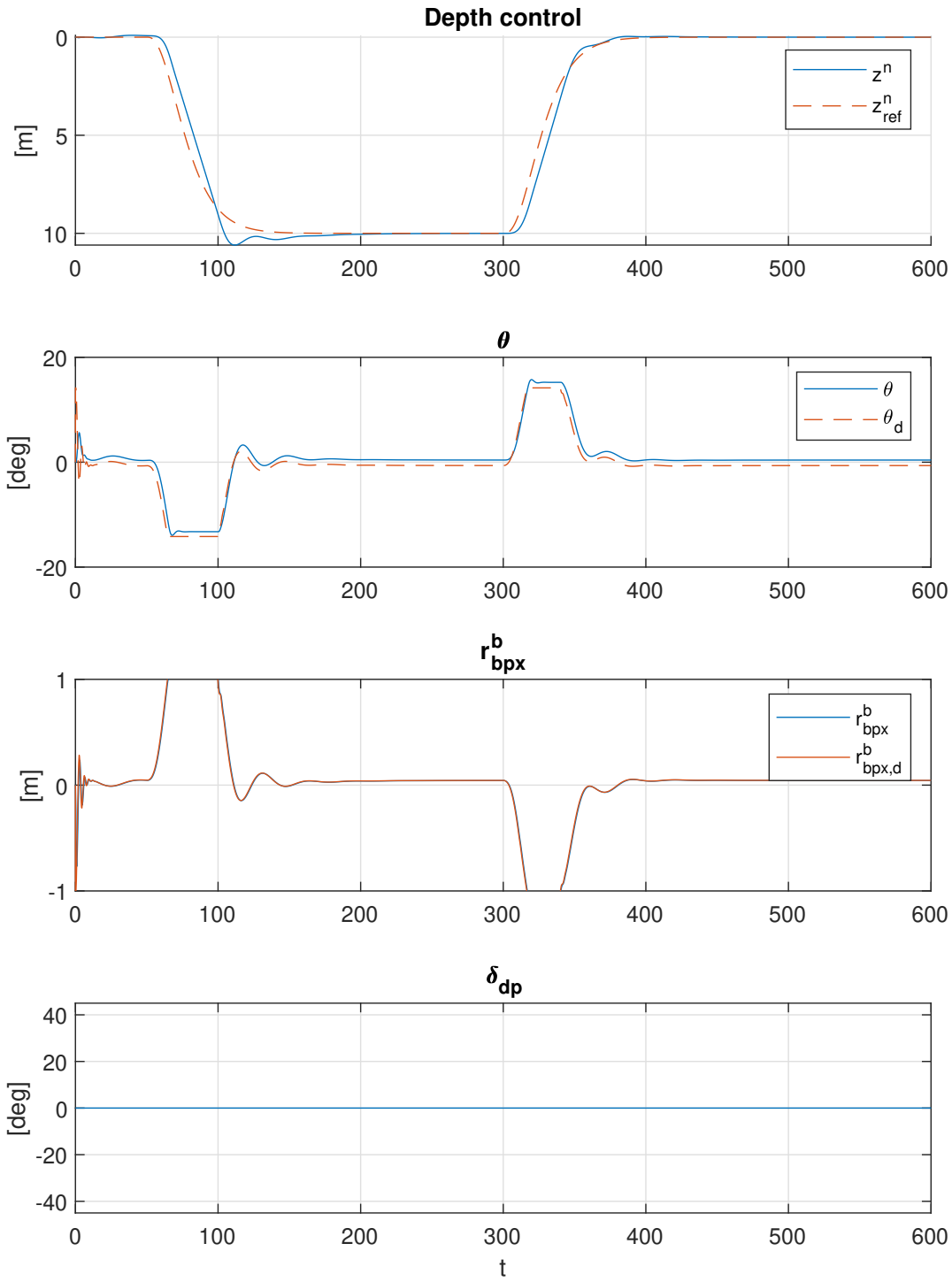

Figure A.2: Result of simulating the system with only MMA, as discussed in section 5

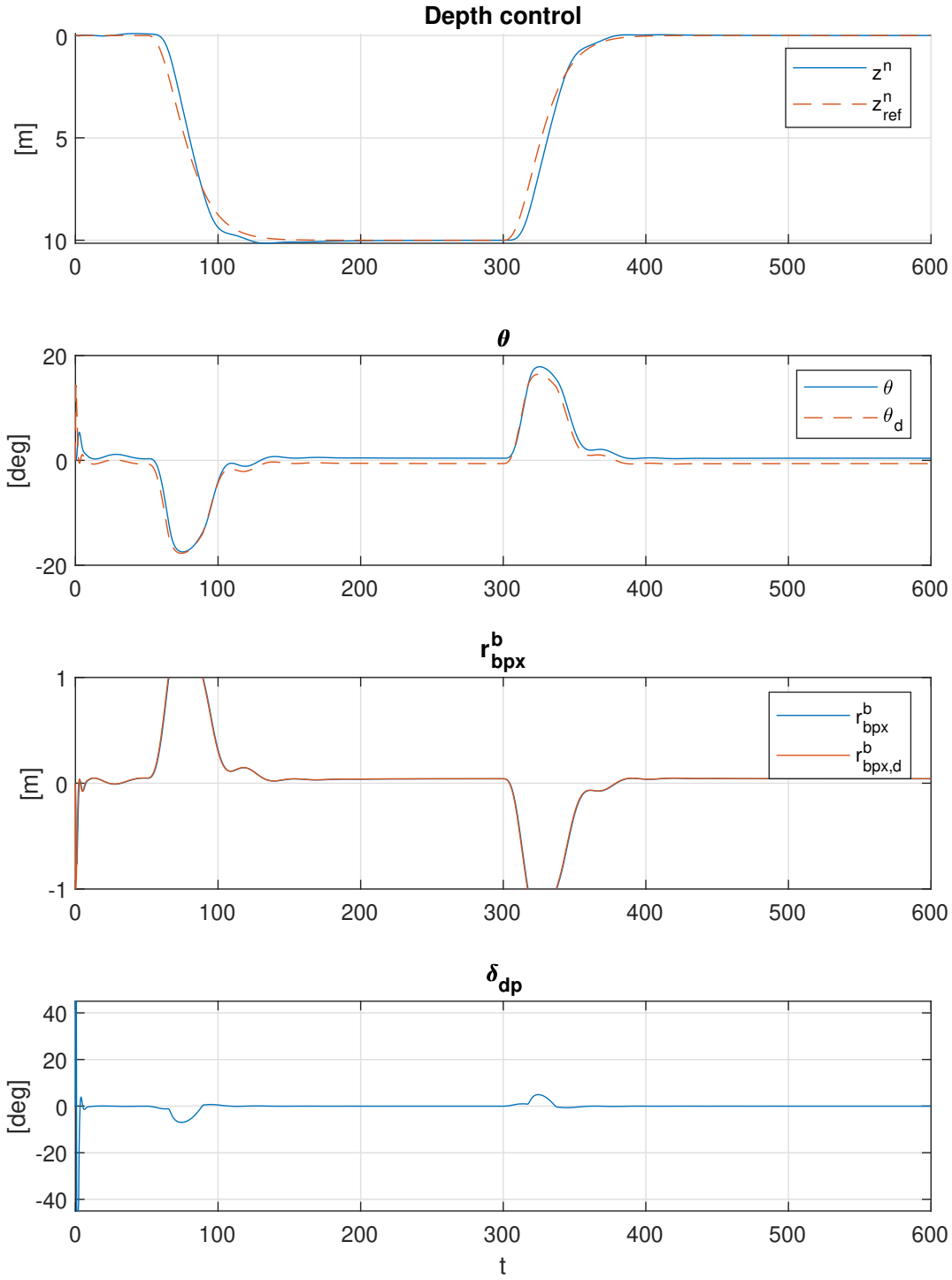

Figure A.3: Result of simulating the system with combined actuation, as discussed in section 5

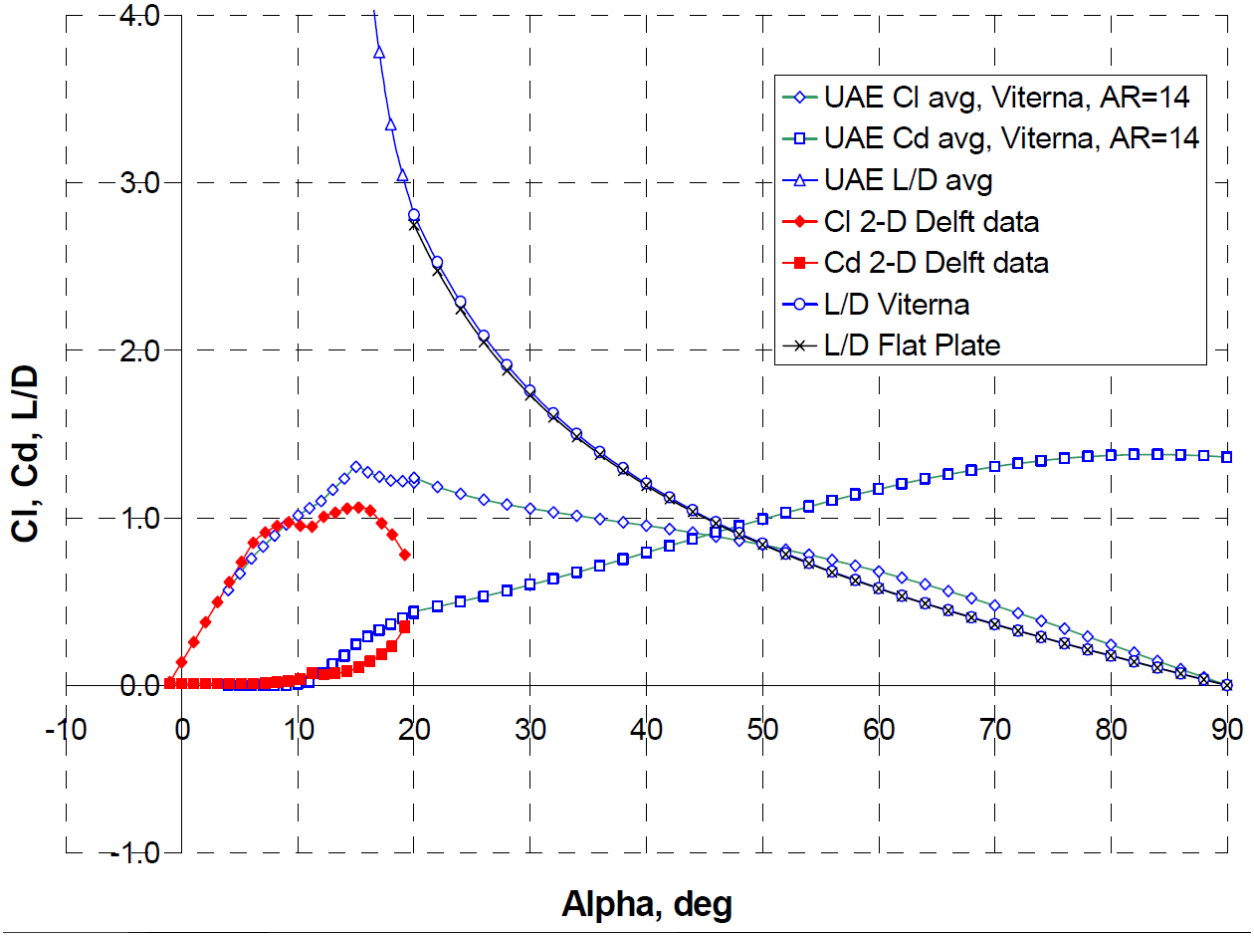

Figure A.4: Figure from [32] showing lift and drag coefficients: "Figure 10. S809 airfoil data input for WT_Perf"

Marcus Nicolai Løvdal

Design of Moving-mass and Dive-plane Control Systems for AUVs

NTNU
Norwegian University of
Science and Technology